1992

The surface characterization of a series of hydroxybenzenes on Ag(111): an EELS and TDS study

Barbara Scheetz Nielsen
Iowa State University

Recommended Citation

Nielsen, Barbara Scheetz, "The surface characterization of a series of hydroxybenzenes on Ag(111): an EELS and TDS study " (1992). *Retrospective Theses and Dissertations*. 10143.
https://lib.dr.iastate.edu/rtd/10143

INFORMATION TO USERS

This manuscript has been reproduced from the microfilm master. UMI films the text directly from the original or copy submitted. Thus, some thesis and dissertation copies are in typewriter face, while others may be from any type of computer printer.

The quality of this reproduction is dependent upon the quality of the copy submitted. Broken or indistinct print, colored or poor quality illustrations and photographs, print bleedthrough, substandard margins, and improper alignment can adversely affect reproduction.

In the unlikely event that the author did not send UMI a complete manuscript and there are missing pages, these will be noted. Also, if unauthorized copyright material had to be removed, a note will indicate the deletion.

Oversize materials (e.g., maps, drawings, charts) are reproduced by sectioning the original, beginning at the upper left-hand corner and continuing from left to right in equal sections with small overlaps. Each original is also photographed in one exposure and is included in reduced form at the back of the book.

Photographs included in the original manuscript have been reproduced xerographically in this copy. Higher quality 6" x 9" black and white photographic prints are available for any photographs or illustrations appearing in this copy for an additional charge. Contact UMI directly to order.

UMI

University Microfilms International
A Bell & Howell Information Company
300 North Zeeb Road, Ann Arbor, MI 48106-1346 USA
313/761-4700 800/521-0600

The surface characterization of a series of hydroxybenzenes on Ag(111): An EELS and TDS study

Nielsen, Barbara Scheetz, Ph.D.

Iowa State University, 1992

U·M·I
300 N. Zeeb Rd.
Ann Arbor, MI 48106

The surface characterization of a series of hydroxybenzenes on Ag(111): An EELS and TDS study

by

Barbara Scheetz Nielsen

A Dissertation Submitted to the
Graduate Faculty in Partial Fulfillment of the
Requirements for the Degree of
DOCTOR OF PHILOSOPHY

Department: Chemistry
Major: Analytical Chemistry

Approved:

Signature was redacted for privacy.

In Charge of Major Work

Signature was redacted for privacy.

For the Major Department

Signature was redacted for privacy.

For the Graduate College

Iowa State University
Ames, Iowa

1992

TABLE OF CONTENTS

GENERAL INTRODUCTION

Background

Phenolic resins and many related compounds have industrial applications as protective coatings, adhesives and integrated circuits [1]. In each case, the phenol-like molecule interacts with a substrate surface (typically metallic) in some way. This interaction may be a simple chemical bond between the molecule and the substrate, decomposition of the organic molecule, or a more complex interaction, possibly leading to surface-catalyzed polymerization. Since these interactions necessarily occur at the substrate surface, surface science techniques should be helpful in their characterization.

Surface science techniques are used to study metal-adsorbate interactions for many different applications. For our purposes, we wish to answer fundamental questions about the metal-adsorbate interaction: What is the nature of this interaction? Which orientation does the adsorbate molecule prefer? Does the organic molecule decompose? Which functional groups bond? Does the substrate catalyze polymerization? In order to answer these questions, we employ three different surface science techniques: high resolution electron energy loss spectroscopy (EELS), thermal desorption spectroscopy (TDS), and Auger electron spectroscopy (AES). Auger electron spectroscopy provides information about the cleanliness of the metal surface [2], TDS determines temperature and coverage conditions for any chemical reactions [3], and EELS provides vibrational information about the bonding geometry of the molecule to the surface [2].

The purpose of this dissertation is to examine the nature of the bonding between phenolic compounds with a metal surface. Our approach to this complex problem is simplification. First, we model the complex phenolic resins with smaller chemical analogs and second, we use a well characterized single crystal metal surface. The chemical analogs chosen to represent phenolic resins include phenol, catechol, resorcinol, hydroquinone, and pyrogallol. These molecules are all hydroxybenzene compounds, differing only in the number and positions of the pendant hydroxyl groups. The metal single crystal face chosen is Ag(111), the one most closely representing a polycrystalline Ag surface.

Literature Review

When considering possible surface catalyzed reactions or polymerization of hydroxybenzene compounds on silver, it is helpful to review the literature of simple chemical analogs to these more complex phenolic molecules. The simplest class of chemical analog consists of aliphatic alcohols or thiols, which model the O-H functionality of hydroxybenzene compounds. In all cases, these compounds readily undergo O-H or S-H bond cleavage to form the alkoxide or thiolate on surfaces of metals such as Al [4, 5], Cu(110) [6-9], Pd [10-12], Ru [13], and Ni [14-17]. In these cases, bonding occurs through the lone pair electrons of the sulfur or oxygen atom. Aliphatic alcohols decompose little (if at all) on clean Ag; the presence of coadsorbed oxygen is necessary to obtain appreciable yields of the alkoxide on these metals [18-20]. The C_1 - C_5 straight chain alkoxides formed on the pre-oxidized Ag surfaces are oriented with their alkyl chains parallel to the surface [20]. Alkoxides may form on clean Cu surfaces [8, 9]; however, again the presence of pre-adsorbed oxygen greatly increases the amount of alkoxy that forms [7-9, 19]. On the pre-oxidized Cu surfaces the chains appear oriented essentially normal to the surface [21, 22].

Unsaturation of the carbon chain can lead to bonding via a different mechanism, that of π bonds to the surface. Thus, unsaturated alcohols can bond to the surface via two different mechanisms: through the lone pair electrons of the oxygen atom or through the π electrons of the unsaturated backbone. Bonding solely through the π electron system would necessarily cause the molecule to lie parallel to the surface. However, if the molecule were already anchored to the surface through the lone pair electrons of the pendant atom, additional bonding via the π electrons could cause the molecule to tilt away from the surface normal. Studies of unsaturated aliphatic alcohols indicate that π-bonding does indeed contribute to the bond between the adsorbate and the metal surface. Unsaturated alcohols such as allyl alcohol and propargyl alcohol do not react with the clean Ag surface; however on the pre-oxidized Ag(110) surface these molecules form an alkoxide intermediate [23]. Further, the planes containing the π orbitals are tilted 25-35° from the surface normal, indicating an off normal adsorption due to the π-bonding of the double or triple bond with the metal surface [24].

Another class of chemical analogs consists of aromatic molecules. Studies of these molecules provide information about the contribution of aromaticity to the surface chemistry of the hydroxybenzenes. This class of compounds may be subdivided into the following three categories: aromatic hydrocarbons (specifically benzene), heteroatom aromatic molecules and aromatic hydrocarbons with side groups (i.e., substituted benzenes). The first category, aromatic hydrocarbons, includes benzene, naphthalene, anthracene, tetracene, perylene, and coronene. On Ag(111) all of these molecules orient with the molecular plane parallel to the surface [25]. On different surfaces, however, the bonding geometry of these molecules depends on the coverage [26]. For instance, at low coverage, the adsorbate-metal bond occurs through the π electrons and thus, the molecules are oriented parallel to the metal surface. Further, when the bonding is chiefly through the π electrons, it is referred to as π-bonding or, for a six-membered ring, η_6 bonding. However, at high coverage, bonding to the surface occurs only through cleavage of the C-H bonds. Thus, the molecules are oriented vertically on the surface, perhaps for steric reasons. In these cases, bonding is referred to as σ-bonded, or η_n, where n depends on the number of σ bonds formed with the surface [27].

Benzene has been studied extensively on a variety of metal surfaces. On most metals studied, and at most coverages, it is agreed that benzene assumes a parallel orientation on the surface and bonds primarily through the π electrons of the aromatic ring. For instance, a parallel orientation is observed for benzene on all surfaces of Ni studied: Ni(100) [28-30], Ni(110) [31], Ni(111) [28-30, 32-34], and Raney Ni [35]. Similarly, for all surfaces of

Pt studied, including Raney Pt, Pt(100), (110), (111), and Pt/Al_2O_3, benzene lies flat on the metal surface [32, 36-40]]. A parallel orientation is also observed on Pd(100) [41-43] and Pd(111) [44]; however, in some cases a slightly tilted orientation is observed on Pd(111) [42, 45-47] and Pd(110) [48]. Further, if coadsorbed with CO on the Pd(111) surface, benzene assumes a parallel orientation [49]. Other metal surfaces, including Ir(111) [50], Mo(110) [51], Rh(111) [52], Os(0001) [53], Ag(111) [54, 55], Ru(001) [56], and Au electrodes [57] all exhibit a parallel, or nearly parallel, orientation of the benzene molecule. Further, a parallel orientation is also observed on oxide surfaces such as Al_2O_3 [40]. Finally, the molecular orientation of benzene is found to be coverage dependent on graphite, i.e., a low coverage yields the parallel orientation and a high coverage yields a perpendicular orientation [26].

The second category of aromatic analogs to the hydroxybenzene molecules is that of heteroatom aromatic molecules. Data exist for both five- and six-member aromatic rings with one of the ring atoms not a carbon atom. Pyrrole (C_4H_4N), a five-member heteroatom aromatic molecule, orients perpendicular, or nearly so, on Rh(111) [58] and Ni(100) [59, 60], bonding via the nitrogen lone pair electrons and the π electron system. Studies of pyridine (C_5H_5N) on Cu(110) [61], Ni(111) [62], Ni(100) [62, 63], Ni(001) [64], Ag [65], Ag(111) [66, 67], silver adatoms on Rh(100) [68], Pd(110) [69], Pd(111) [46, 70], Pt(111) [71, 72], Pt(110) [39], Ir(111) [50, 73], and ZnO($1\underline{1}00$) [74] indicate that the nature of the adsorbate-metal bond is coverage dependent. For example, at low coverage, pyridine adopts the orientation of benzene, with its molecular plane parallel to the surface.

However, at high coverage, the molecule adopts an orientation more nearly perpendicular to the surface plane. In this slightly inclined orientation, the nitrogen atom of the ring forms the anchor point with the surface, with additional bonding contribution via the lone pair electrons of the nitrogen atom. Further, at least one study indicates that the orientation of the pyridyl species is temperature dependent i.e., at low temperatures, a parallel orientation is observed, whereas at high temperatures, an α-pyridyl (η_2) species is formed [60]. Pyrazine ($C_4H_4N_2$), another six-member heteroatom aromatic molecule, binds through the nitrogen lone pair electrons and is tilted from the surface normal, indicating some π electron contribution [54].

The third category of aromatic molecules most closely related to the hydroxybenzene molecules includes the substituted benzenes such as chlorobenzene and benzenethiol. Chlorobenzene on Ag(111) has been studied by UV photon-induced chemistry, and is observed to undergo dissociation via cleavage of the C-Cl bonds. Following C-Cl scission, the molecule dimerizes to form a chemisorbed biphenyl species oriented parallel to the surface, presumably bonded through the π electron system [75]. Benzenethiol (or thiophenol) undergoes S-H bond cleavage on Mo(110) to form phenyl thiolate [76]. Again, the aromatic ring is nearly parallel to the surface at low coverage, and makes an angle of about 20° with the surface normal at high phenylthiolate coverage [77]. Thiophenol adsorbed on Ni(100) exhibits an inclined orientation with the S-C bond axis nearly normal to the surface [78]. On Pt(111) and Ag(111) electrode surfaces, thiophenol bonds mainly through the sulfur atom [79, 80] and again, the molecule is oriented nearly perpendicular to the surface.

Finally, some data are also available concerning the molecules of interest, i.e., the molecules which are the subject of this dissertation. Phenol has been studied to some extent. When coadsorbed with oxygen, surface phenoxide is stabilized on Mo(110) [81, 82], and near-edge X-ray fine structure (NEXAFS) studies indicate the phenyl ring plane makes an angle of ~30° with respect to the surface normal [83]. When deposited from aqueous solutions on Pt(111) electrodes, EELS studies indicate that phenol adsorbs with the aromatic ring parallel to the surface [84-86]. A NEXAFS study of phenol on Ag(110) indicates that the aromatic ring tilts 40 ± 5° from the surface plane [87]. The interaction of phenol with Ni(111) has been studied by reflection-absorption infrared spectroscopy (RAIRS), and it is found to bond through the π electron ring, adopting a parallel orientation on the surface [88]. On Ni(110) phenol is observed with a ring orientation "in proximity to the metal surface, but not necessarily parallel" [89]. On Pd(110), phenol coordinates to the surface via the π electrons of the aromatic ring and via the heteroatom; thus, it adopts an adsorption geometry with the ring plane in "close proximity" to the metal surface [90], i.e., a parallel orientation. Finally, on Cu(110) phenol adopts a parallel geometry to the metal surface.

Catechol and hydroquinone have been studied previously using EELS. However, in the previous studies, the compounds are deposited from aqueous solutions, whereas in the present work, we employ gas phase adsorption. Catechol adsorbs parallel to the Pt(111) electrode surface as observed in EELS studies [85]. Packing densities, as determined by cyclic voltammetry (CV) studies, indicate that catechol orients parallel to the

Pt(111) and Pt(100) electrode surfaces [91]. Thin-layer electrochemical techniques such as linear potential scan voltammetry and potential-step chronocoulometry show hydroquinone to adsorb close-packed in a flat, or parallel, configuration to smooth Pt electrode surfaces [86]. Further, packing density studies, along with EELS studies, indicate a parallel configuration for hydroquinone on the well-defined Pt(111) surface [84]. However, on smooth, polycrystalline Pt surfaces, the orientation adopted by hydroquinone depends on the concentration of the aqueous solution from which it is deposited. One study indicates that the molecule is flat-oriented (i.e., η_6 or π-bonded) if deposited from a low concentration solution; whereas, when the adsorbate concentration is increased, the packing density on the surface increases abruptly and the molecule adopts an edgewise (i.e., η_2 or di-σ) orientation [92]. Further, the adsorption and orientation of hydroquinone on this surface is affected by temperature. For example, the packing density of low adsorbate concentrations increases as the temperature increases and the packing density of high adsorbate concentrations decreases as the temperature increases [86].

Very few studies exist for pyrogallol and essentially none exist for resorcinol. Pyrogallol has been studied by linear potential scan voltammetry and potential-step chronocoulometry using thin-layer electrodes, and is determined to lie flat on smooth Pt electrodes [86]. To the best of this author's knowledge, however, pyrogallol has not been studied using EELS or any other surface science technique. Finally, no literature is available, to date, on the surface characterization of resorcinol.

The study reported in this dissertation is unique in three respects. First, the vibrational studies are performed under UHV conditions, i.e., exposure of the metal to the compounds of interest is achieved *in situ* through exposure to vapors of the solid compounds. Second, to date, none of these molecules has been studied on the Ag(111) surface. Finally, this is the first comprehensive survey of the adsorption characteristics and vibrational properties of these molecules using TDS and EELS.

Normal Mode Analysis

Since the primary basis for this dissertation is vibrational spectroscopy, it is beneficial at this point to review some fundamentals of molecular vibrational spectroscopy as it applies to benzene, benzene derivatives, and high resolution electron energy loss spectroscopy. Each molecule has 3N degrees of freedom, where N is the number of atoms in the molecule. Three degrees of freedom are rotational, three are translational, and the remainder are vibrational. Thus, unless it is linear, each molecule will have 3N-6 normal vibrations. In theory, all atoms can participate in every normal vibration of the molecule, with amplitudes individual in magnitude and direction. The amplitudes are regulated by the symmetry relations of the molecule [93].

The benzene molecule consists of 12 atoms and thus, has thirty normal vibrational modes. Further, benzene is highly symmetric, belonging to the D_{6h} point group. Because of the high symmetry, vector diagrams corresponding to all thirty normal vibrations can be derived simply by symmetry considerations. The atomic displacements lie in three main directions: radial, tangential, and out-of-plane. Both the radial and tangential vibrations are in-plane, with atomic displacements pointing either normal to or along the tangent of the regular hexagon, respectively. An example of each of these three main types of vibrations is depicted in Figure 1. Vector diagrams for all thirty normal vibrations can be found elsewhere [93].

The thirty normal vibrations of benzene are listed in the first column of Table 1, according to the numbering system established by Wilson [94]. In the second column of Table 1, a description of the vibrational mode is given. Stretching vibrations are denoted by ν, bending modes in which the vibrating atoms preserve a well-defined plane are designated by β (i.e., in-plane, ip), and vibrations perpendicular to such a plane by γ (i.e., out-of-plane, op). Each normal vibration can be further characterized by the individual symmetry species of a particular point group. The symmetry species of the normal vibrations of the free benzene molecule, in point group D_{6h}, are listed in the third column of Table 1.

The introduction of substituents onto the benzene ring reduces the symmetry such that the normal vibrational modes can no longer be defined by the molecular symmetry. This is true since individual normal coordinates, depending on the substituents, will appear. However, the total number of vibrations of the substituted benzene is still 3N-6. Further, if only the six carbon atoms of the ring, the hydrogens of the benzene nucleus and the atoms of the substituent directly attached to the ring are considered, thirty normal vibrations may be separated from the rest. These thirty vibrations can be directly related to the thirty normal vibrations of

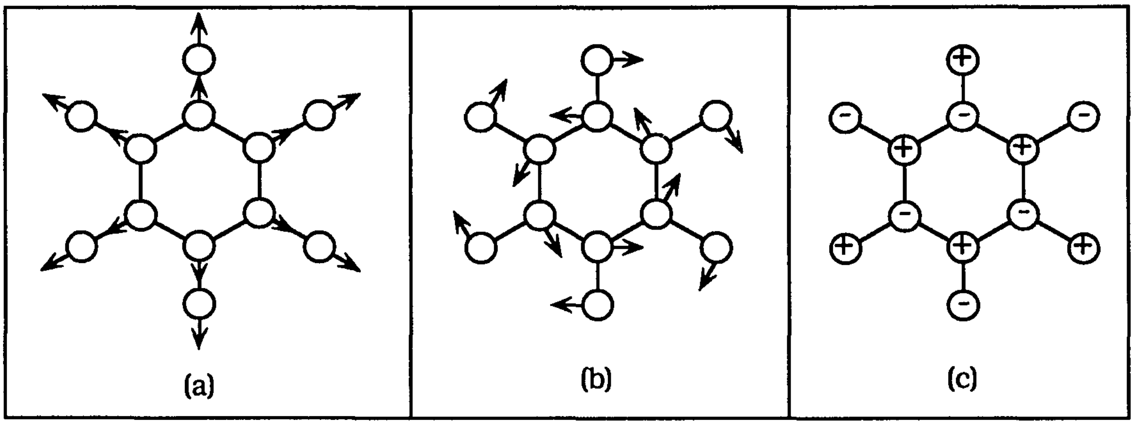

Figure 1. Vector diagrams of the three types of normal mode vibrations for benzene: (a) radial, (b) tangential and (c) out-of-plane.

Table 1. Vibrational mode assignments for benzene. Symmetry species for the D_{6h}, C_{2v}, C_{6v}, and C_{3v} point groups are presented. The shaded regions indicate symmetry species that represent totally symmetric representations of the respective point groups *and* obey the metal-surface selection rule.

[a]Reference [93].
[b]Reference [44].
[c]Reference [52].
[d]Reference [32].
[e]Reference [29].

* The D_{6h} point group represents the symmetry of the gas phase molecule.

Mode #	Vibrational Mode and Description	Symmetry Species				IR freq. (cm^{-1}) [a]	Intensity	Pd(111) [b]	Rh(111) [c]	Pt(111) / Ni(111) [d]	Ni(111) / Ni(100) [e]
		D_{6h} •	C_{2v} (⊥)	C_{6v} (//)	C_{3v} (//)						
1	Radial skel./breathing	a_{1g}	a_1	a_1	a_1	993			880		
2	ν_{CH}, in phase stretch	a_{1g}	a_1	a_1	a_1	3073			2970/3030	3000	
3	β_{CH}, in phase bend	a_{2g}	b_2	a_2	a_2	1350	vw				
4	o.p. skeletal, C_3 pucker	b_{2g}	b_1	b_1	a_1	707	vw				
5	γ_{CH}, o.p. trigonal bend	b_{2g}	b_1	b_1	a_1	990	vvw				
6a	Radial skel./ip C_3 bend	e_{2g}	a_1	e	e	606	vvw				
6b	Radial skel./ip C_3 bend	e_{2g}	b_2	e	e	606	vvw				
7a	ν_{CH} (ν_{CX}), stretch	e_{2g}	a_1	e	e	3056			2970/3030	3000	
7b	ν_{CH} (ν_{CX}), stretch	e_{2g}	b_2	e	e	3056					
8a	ν_{CC}, stretch	e_{2g}	a_1	e	e	1599	vvw				
8b	ν_{CC}, stretch	e_{2g}	b_2	e	e	1599	vvw				
9a	β_{CH}, ip bend	e_{2g}	a_1	e	e	1178	vw				
9b	β_{CH}, ip bend	e_{2g}	b_2	e	e	1178	vw		1130		1115
10a	γ_{CH}, op C_6 libration	e_{1g}	a_2	e	e	846	vw	825			
10b	γ_{CH}, op C_6 libration	e_{1g}	b_1	e	e	846	vw				
11	γ_{CH}, in phase, o.p.	a_{2u}	b_1	a_1	a_1	673	vvs	735	776/819	890/920	750
12	Rad. skel./C_3 trig. bend	b_{1u}	a_1	b_1	a_1	1010	vvw				845
13	ν_{CH} (ν_{CX}), trig. stretch	b_{1u}	a_1	b_1	a_1	3057					3025
14	ν_{CC}	b_{2u}	b_2	b_2	a_2	1309	vvw		1320		1325
15	β_{CH},ip trigonal bend	b_{2u}	b_2	b_2	a_2	1146	vvw				
16a	op skeletal, C_3 bend	e_{2u}	a_2	e	e	398					
16b	op skeletal, C_3 bend	e_{2u}	b_1	e	e	398					
17a	γ_{CH}, op	e_{2u}	a_2	e	e	967	vw				
17b	γ_{CH}, op	e_{2u}	b_1	e	e	967	vw				
18a	β_{CH}, ip bend	e_{1u}	a_1	e	e	1037	vs	1145		1150	845/1115
18b	β_{CH}, ip bend	e_{1u}	b_2	e	e	1037	vs				
19a	ν_{CC}, stretch	e_{1u}	a_1	e	e	1482	vs	1460	1420	1420	1425
19b	ν_{CC}, stretch	e_{1u}	b_2	e	e	1482	vs				
20a	ν_{CH} (ν_{CX}), stretch	e_{1u}	a_1	e	e	3064	vs	3025	2970/3030	3000	3025
20b	ν_{CH} (ν_{CX}), stretch	e_{1u}	b_2	e	e	3064	vs				

benzene. Therefore, as long as the benzene nucleus dominates the force field of the molecule, the normal modes of the substituted benzene may be compared to the normal vibrations of benzene [93]. Thus, the loss features in the EEL spectra which can be attributed to the vibrations of the six ring-carbons and the six other atoms directly bound to the ring, will be characterized by the numbers symbolizing the normal modes of the parent benzene molecule (i.e., those numbers listed in Table 1.)

Upon adsorption onto a surface, the symmetry of a molecule is also reduced, according to its orientation on the surface. Thus, if the benzene molecule assumes a perpendicular orientation on the surface, its symmetry is reduced to C_{2v}; however, if it adsorbs in a parallel configuration, its symmetry is reduced to C_{nv}, where n depends on the exact adsorption site. For comparison purposes, we will consider the adsorption of benzene on fcc(111) faces since Ag(111) falls into this category. With this restriction in mind, if benzene adsorbs in a parallel orientation, its symmetry is reduced to either C_{6v} or C_{3v}, assuming a high symmetry orientation. The symmetry species of benzene's normal vibrations under these various point groups are also given in Table 1. As noted earlier, benzene has been studied extensively on several different metal surfaces using vibrational spectroscopic techniques. The results of these earlier studies along with the mode assignments are also given in Table 1.

Further, when an N-atom species adsorbs on a surface, its 3 degrees of translational freedom can be considered as an extra 3 degrees of vibrational freedom. For instance, the entire molecule may vibrate perpendicular, or parallel, to the surface plane. Such vibrations are typically called frustrated translations, and occur at very low frequencies ($\leq$ 600 cm^{-1}) [95]. The classification of these extra degrees of freedom and their influence on the normal modes of the adsorbent depends primarily on the adsorption characteristics. For example, in all cases, the translational motion of the adsorbing species towards the surface must be converted to a vibration of the species against the surface (i.e., a stretching vibration perpendicular to the surface). However, classification of the translational motion parallel to the surface (two degrees of freedom) depends primarily on the strength of the adsorption [96]. If the molecule is physisorbed, or weakly bound, to the surface, then diffusion across the surface becomes possible and the parallel motion is characterized as a hindered translation. Conversely, if the molecule is chemisorbed, or strongly bound, to the surface, diffusion is inhibited and the translational motion parallel to the surface is described as a vibration parallel to the surface. Similar arguments apply to the rotations of the gas phase species which become hindered upon adsorption on the surface. For instance, if the adsorption is strong, a new vibrational mode (often called a libration) is observed; however, if the adsorption is weak, the motion may be referred to as a "psuedorotation" [96]. The latter scenario is most likely to apply to rotation around the surface normal and these vibrations are commonly referred to as wagging modes. Thus, vibrational modes different from those of the free molecule may be observed due to surface adsorption .

Because an N-atom molecule can possess up to 3N-6 vibrations, the vibrational spectra of complex molecules may become complicated. However, spectroscopic selection rules can be applied to simplify the interpretation of these spectra. These spectroscopic selection rules are based on whether transitions from one stationary state of a system to another, with the gain or loss of a quantum of energy, are allowed or forbidden. The type of transition observed in IR (and EELS) spectroscopy is the electric dipole-allowed transition. In the electric dipole transition, the charge distributions of the two different states differ in a way that corresponds to a change in the electric dipole. Thus, this transition can couple with electromagnetic radiation by interaction with the oscillating electric vector and then transfer energy to or from the electromagnetic field [97].

In general, the intensity, I, of a transition from a state described by ψ_i to another described by ψ_j is given by equation (1).

$$I \propto \int \psi_i \, \mu \, \psi_j \, d\tau \qquad (1)$$

The symbol μ is a transition moment operator, corresponding to a change in the electric dipole. The electric dipole operator may be written in the following form,

$$\mu = \Sigma e_i x_i + \Sigma e_i y_i + \Sigma e_i z_i \qquad (2)$$

where e_i represents the charge on the ith particle, and x_i, y_i and z_i refer to the orientation of the oscillating electric vector of the radiation relative to a Cartesian coordinate system fixed in the molecule. Substituting equation (2) into equation (1) gives the following expression which is expressed as three separate equations due to the orthogonality of the Cartesian coordinates [97].

$$I \propto \int \psi_i \, x \, \psi_j \, d\tau$$
$$I \propto \int \psi_i \, y \, \psi_j \, d\tau \qquad (3)$$
$$I \propto \int \psi_i \, z \, \psi_j \, d\tau$$

The above equations mean that the transition from the ith to the jth state (or the reverse) may acquire its intensity in any of three ways, specifically, by interaction with an electric vector oscillating in the x, y or z direction. The above integrals can be nonzero only if the direct products of the irreducible representations of the ith and jth states and the representations to which the Cartesian coordinates (x, y, and z) belong contains the totally symmetric representation. Further, the ψ_i state is always considered to belong to the totally symmetric representation of the point group (i.e., A_1 or a'.) Thus, in order to determine if a transition is electric dipole allowed, one only needs to determine if any of the three following direct products are nonzero.

$$\Gamma_i \otimes \Gamma_x \otimes \Gamma_j$$
$$\Gamma_i \otimes \Gamma_y \otimes \Gamma_j \qquad (4)$$
$$\Gamma_i \otimes \Gamma_z \otimes \Gamma_j$$

In equation (4), Γ is the irreducible representation of the ith or jth state, or that containing the Cartesian coordinates (x, y and z). If any of the above direct products contain the totally symmetric representation, the transition is allowed, and further, the transition is considered polarized in the direction of the corresponding Cartesian coordinate. For example, if the only allowed transition corresponds to $\Gamma_i \otimes \Gamma_x \otimes \Gamma_j$, the transition is polarized in the x direction or, it is x-polarized. Therefore, an electric dipole transition will be allowed with x, y, or z polarization if the direct product of the representations of the two states concerned is or contains the irreducible representations to which x, y, or z, belong, respectively.

Since ψ_i belongs to the totally symmetric representation of the point group, the coordinate x, y or z and ψ_j must belong to the same representation in order that their direct product contain the totally symmetric representation, whereby the representation of the entire integral contains the totally symmetric representation. Therefore, a fundamental transition will be infrared active (i.e., will give rise to an absorption band) if the normal mode which is excited belongs to the same representation as any one of the Cartesian coordinates x, y, or z [97].

In the EELS experiment, the incoming electrons lose some of their energy to the vibrational modes of the adsorbate through long-range interaction between the electric field of the incoming electron and the dynamic dipole of the adsorbate. This inelastic collision produces forward-scattered electrons that eventually appear in the specular direction. The dipole nature of this interaction imposes a "metal-surface" selection rule under which only those vibrational modes with a component of the dynamic dipole moment perpendicular to the surface can be observed [96]. In a very general sense, these vibrational modes belong to the totally symmetric representation of the relevant point group. The individual symmetry species belonging to the totally symmetric representations of the relevant point groups are shaded in Table 1.

If the direction perpendicular to the surface is chosen as the z-axis, this means that only the direct product

$$\Gamma_i \otimes \Gamma_z \otimes \Gamma_j$$

need be evaluated; that is, products involving Γ_x or Γ_y will not be dipole-allowed. Γ_z is the totally symmetric representation for all standard group tables used in this work with one exception, that is, Γ_z is totally symmetric for all C_{nv} point groups, but not C_s [97]. Effectively, this means that for the C_{nv} point groups, Γj must simply be the totally symmetric representation; for the C_s point group, there is an additional restriction arising from the definition of axes in C_s. According to Cotton [97], for the Cs point group, the z-axis lies in the surface plane, perpendicular to σ_h, and belonging to the a" irreducible representation. The a' representation contains both x *and* y axes, both lying parallel to σ_h, but only one of which can be perpendicular to the surface plane. Therefore, the dipole-allowed transitions for the C_s point group must belong to the totally symmetric representation, a', *and also* must contain a component of μ perpendicular to the surface. The easiest way to satisfy the latter requirement is simply by inspection.

Thus, once the symmetry of the adsorbate-metal complex is determined and the vibrations classified according to specific symmetry species, only those modes belonging to the totally symmetric representation *and* having a component of the dipole moment perpendicular to the surface will be observed in the EEL spectra. Application of the metal-surface selection rule to peaks observed in the EEL spectra assists in the assignment of those loss features. Furthermore, the presence, absence, and intensity of loss features can help to elucidate the molecular orientation of the adsorbate on the surface. These principles will be applied throughout this dissertation, and will form the foundation upon which interpretation of much of the experimental data will rest.

Explanation of Dissertation Format

This dissertation is arranged in three parts. The three parts include: "Part 1: The Surface Characterization of Phenol on Ag(111): An EELS and TDS Study"; "Part 2: A Comparative EELS and TDS Study of Catechol, Resorcinol and Hydroquinone on Ag(111)"; and "Part 3: The Surface Characterization of Pyrogallol on Ag-Coated Polyester and on Ag(111): An EELS Study." The parts will be combined and published as one manuscript. Following Part 3 are the General Conclusions for the entire dissertation. The references cited in the Bibliography are just those from the General Introduction, Experimental Procedures and General Conclusions sections. All references cited within each part are listed at the end of each part.

EXPERIMENTAL PROCEDURES

All experiments are performed in one standard stainless steel ultrahigh vacuum (UHV) chamber with a typical base pressure of 1-2x10^{-10} Torr. A schematic of this chamber is shown in Figure 1. Ultrahigh vacuum conditions are achieved using a 400 L/s ion getter pump, a 170 L/s turbomolecular pump and a titanium sublimator. The chamber is equipped with a mass spectrometer, a retarding field energy analyzer for Auger electron spectroscopy (AES), a high resolution electron energy loss spectrometer (EELS), a metal evaporator, and an ion sputter gun and gas inlet manifold for Ar^+ bombardment. Further, a dual needle gas doser assembly is used to introduce foreign gases into the chamber. The first dosing needle points at the crystal, allowing direct-line gas exposure of the crystal, while the second dosing needle is directed into the ionizing head of the mass spectrometer. This second needle allows for periodic purity checks of the dosing gas.

The hydroxybenzenes are introduced to the UHV chamber via a syringe needle doser, that is, an open tube with an inner diameter of 0.047 inch. The following dosing procedure is used: (a) establish a head space pressure of ~100 - 200 mTorr in the sample bulb, (b) pump out the bulb through the gas manifold to ≤0 mTorr and (c) open the doser to the chamber to expose the crystal. This procedure is used since mass spectral data indicate that volatile contaminants exist in the sample bulb at pressures greater than ~0 mTorr. The exposure units reported are Langmuir (L, 1 L = 10^{-6} Torr*s), calculated by multiplying the chamber

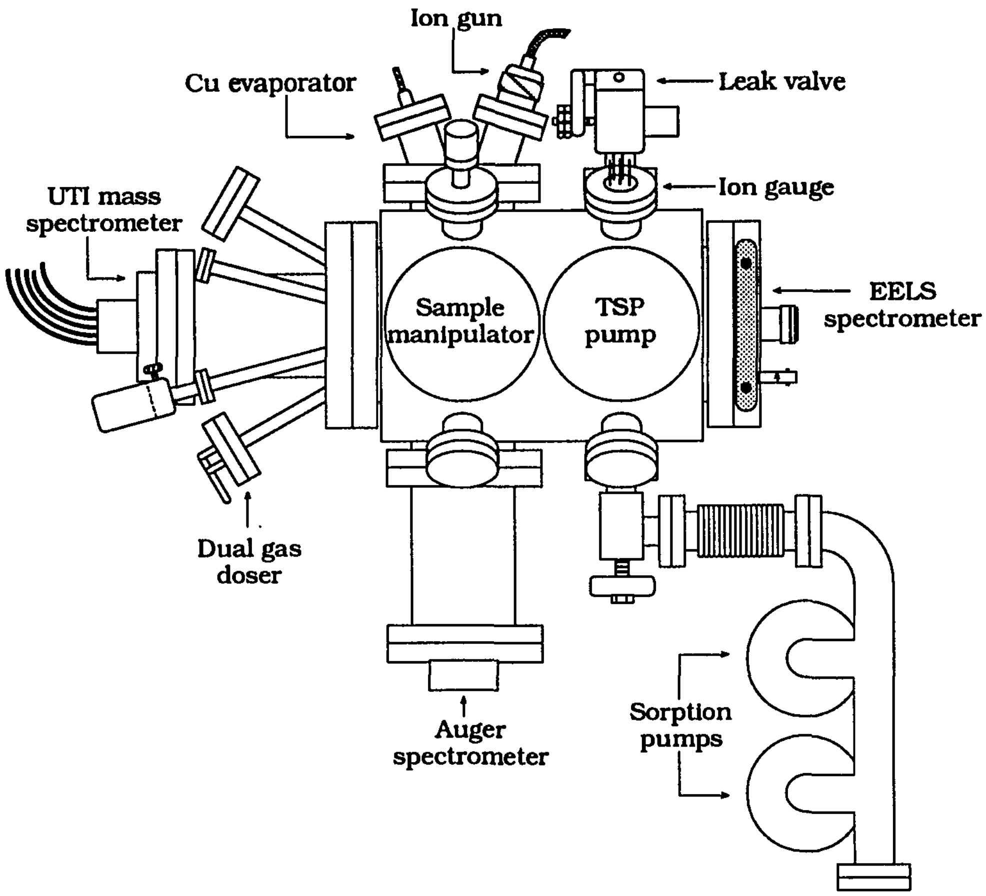

Figure 1. Schematic diagram of the ultrahigh vacuum (UHV) chamber.

background pressure during exposure by the exposure time. Thus, contrary to the normal usage, these exposure units do not reflect the integrated gas flux at the crystal directly. Instead, we assume that the units are proportional to the integrated flux, and thus, are still a useful, although qualitative, measure of the true exposure. Figure 1 depicts the location of the ion gauge relative to the doser, as this may have some effect on the ultimate background pressure measured.

The metal evaporator is included in the chamber to facilitate studies of the hydroxybenzenes on films of Cu on Ag. The evaporator consists of two high conductivity Cu feedthroughs, Cu barrel connectors, a tungsten wire evaporation basket and oxygen-free, high conductivity (OFHC) Cu wire. Holes are drilled in the barrel connectors and the ends of the tungsten basket are inserted through the holes. The basket is held is place simply by the "tightness" of this fit, which also provides electrical continuity. The barrel connectors are attached to the end of the Cu feedthroughs by set screws. A segment of OFHC Cu wire is woven around the W basket, which melts and evaporates as current passes through the W wire. An external power supply is used to pass current through the evaporator basket. A diagram of the evaporator arrangement is shown in Figure 2.

The chamber is periodically baked in an effort to reduce background contaminants and reach UHV conditions. Bakeout ovens have been designed and custom fit to the chamber such that, when assembled, the upper half of the chamber is enclosed. The lower portion of the chamber is wrapped with heating tapes and insulation for bakeout procedures. Typically, the chamber is baked at a temperature of 100 °C for a 24 hour

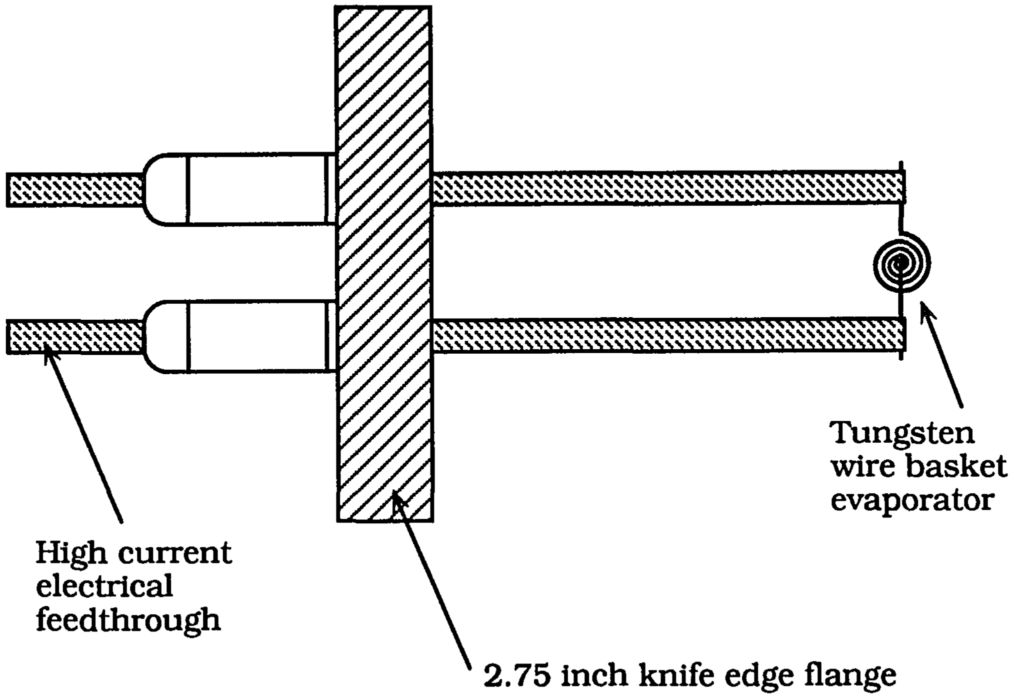

Figure 2. Schematic drawing of the Cu evaporator.

period or until the pressure begins to fall following an initial rise. The background pressure during a bakeout reaches ~$5x10^{-7}$ Torr after approximately 8 hours and then stabilizes at ~$5x10^{-8}$ Torr after approximately 20 hours. During bakeout, the gate valves between the pumps (i.e., turbomolecular and ion) and the chamber are open, and the pumps are pumping. Further, the turbo pump is baked using its own heating jacket, and the ion pump is baked using an internal heater. Periodically throughout the bakeout, the titanium sublimator pump (TSP) filaments are flashed. The three TSP filaments are flashed alternately with a current of ~45 A, while monitoring the chamber pressure. After shutting off the bakeout, all the filaments in the chamber (i.e., Auger, EELS, TSP, and ion gun filaments) are flashed for ~1 minute, allowing them to outgas. Also at this time, the crystal is flashed to ~900 K to desorb any adsorbed contaminants. Further, the TSP filaments are periodically flashed following a bakeout to help decrease the background pressure. Within 12 to 18 hours after a bakeout is turned off, the chamber base pressure is typically ~$1x10^{-10}$ Torr.

The Ag(111) crystal is approximately 1 cm^2 in area and approximately 4 mm thick, and it is oriented and polished to within 0.5° of the (111) face on both sides. The initial crystal cleaning procedure in vacuum is a repeated cycle of ion bombardment at 370 K, annealing to 570 K and oxidation to remove any bulk contaminants such as C, S, or O. Sample cleanliness is monitored by either EELS or AES. Between experiments the sample is cleaned by exposing the sample to 12 L O_2 followed by heating to 900 K to desorb any remaining contaminants. The characteristic Ag Auger transitions occur at ~266, 304 and a doublet at 351 and 356 eV [98]. Since the contaminant C Auger transition occurs at 272 eV and overlaps the 266 eV Ag transition, the cleanliness of the Ag surface is estimated when the C_{272}/Ag_{304} peak ratio, R, is within the range of 0.42 - 0.55 [99]. In the current experiments, the above cleaning procedure is repeated until the C/Ag Auger ratio falls within the range of 0.500 and 0.650. An AES spectrum of a clean Ag surface is shown in Figure 3. The cleanliness of the Ag crystal is also monitored by EELS and is assumed clean when the EEL spectrum is featureless. An EEL spectrum of the clean Ag surface is shown in Figure 4. A clean crystal is essential to assure reproducible experimental results.

Because Ag is not easily spot welded, a uniquely designed sample holder is used. A drawing of this sample holder is shown in Figure 5. The sample holder consists of three Cu blocks: one T-shaped backbone and two heater blocks. The Cu blocks are separated by two 0.020 inch sapphire sheetsand are aligned using a glass rod. The sapphire and glass provide electrical isolation, while allowing thermal conduction, across the blocks. Four Mo rods (0.063 inch diameter) extend in a square configuration out from the face of the sample holder, and two Ta wires (0.020 inch diameter) are spotwelded vertically across these Mo rods, connecting the top and bottom rods. Two Ta wires (0.015 inch diameter) are spotwelded to the thick Ta wires horizontally, to connect the left and right sides. Thus, the Ta wires form a square extended out from the sample block via the Mo rods. The Ag sample is supported in this Ta wire square by pressing the wires into grooves cut in the top and bottom edges of the crystal.

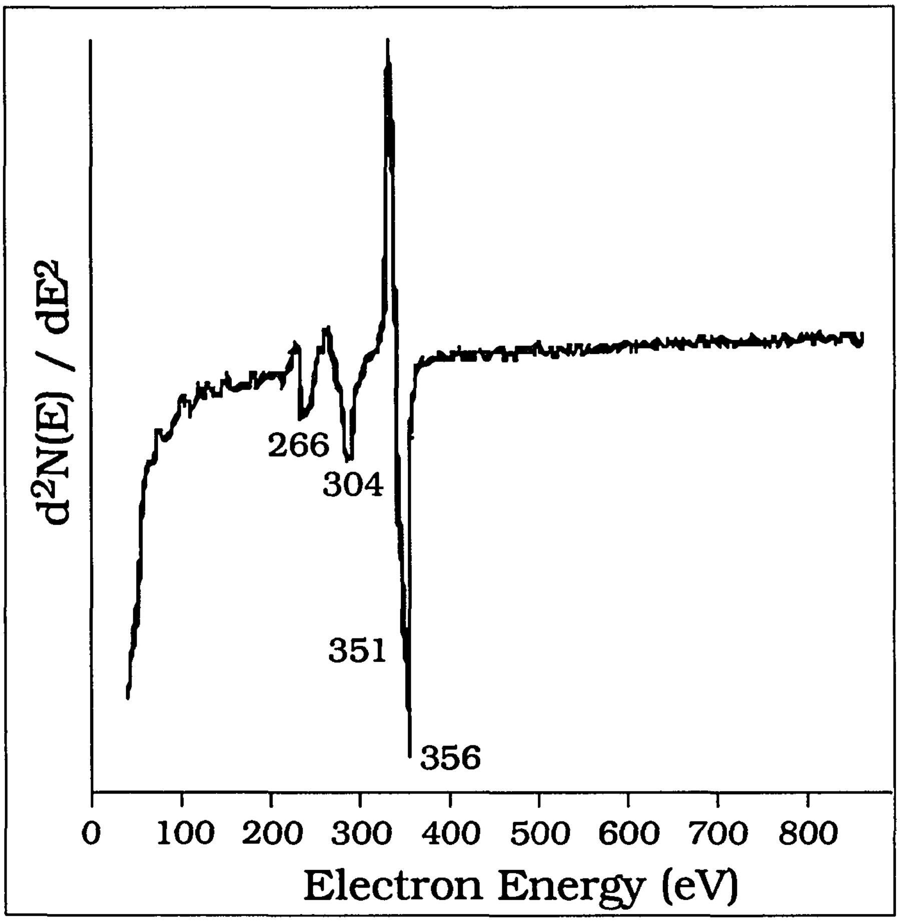

Figure 3. Auger electron spectrum of clean Ag.

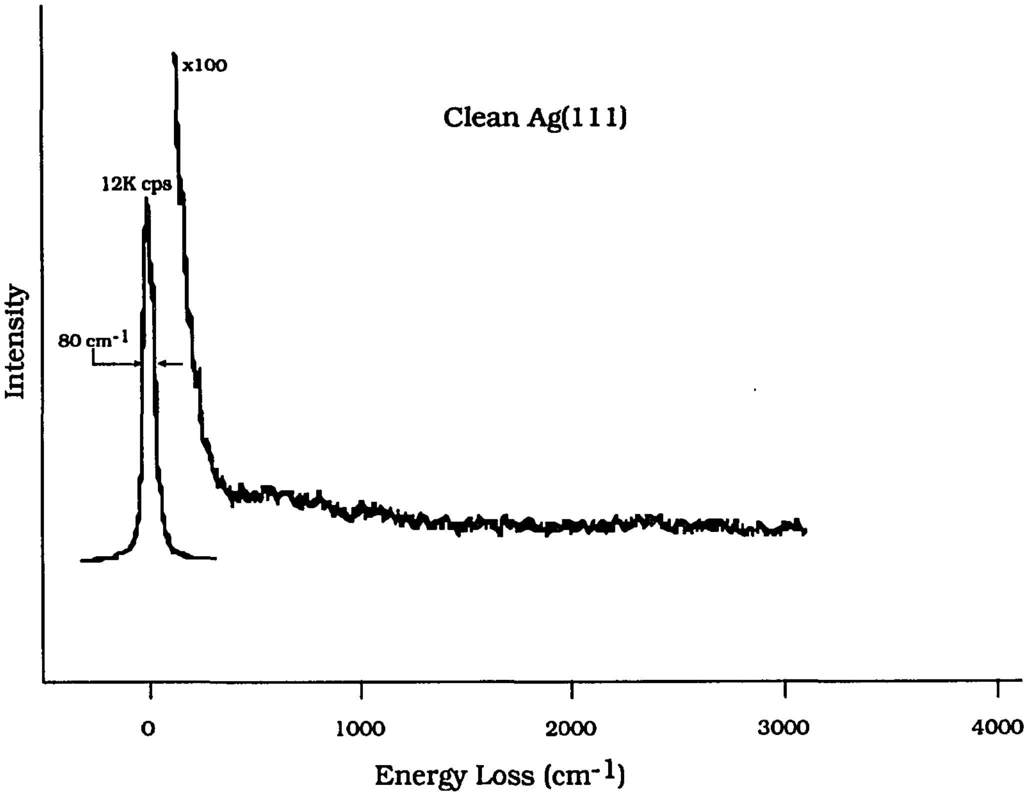

Figure 4. Electron energy loss spectrum of clean Ag.

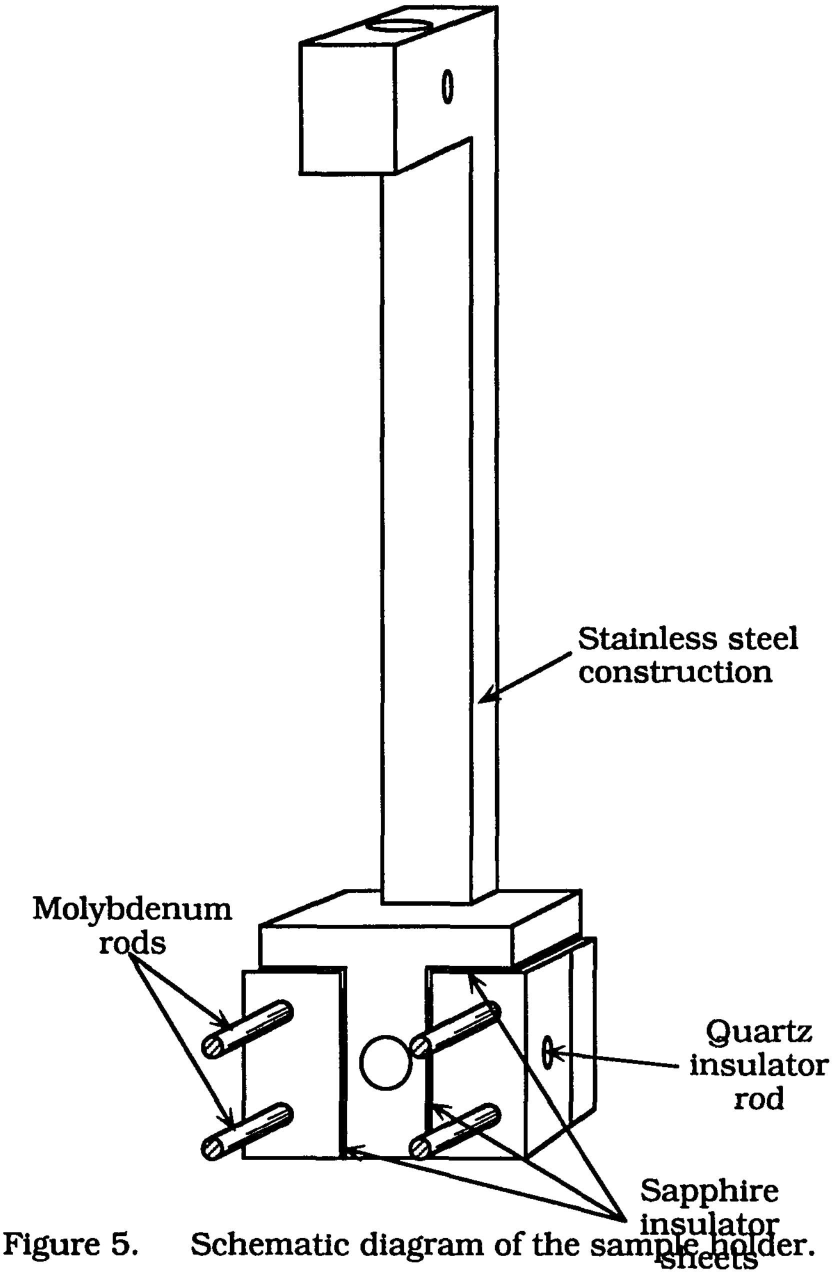

Figure 5. Schematic diagram of the sample holder.

Sample heating is achieved by passing current through the Ta wires using an external power supply. The crystal temperature is measured by 0.005 inch diameter Cr-Al thermocouple wires spotwelded together, with the resulting junction press-fit into a 0.018 inch diameter hole drilled in the center back of the crystal. Sample cooling is accomplished by means of a liquid nitrogen reservoir connected to the sample block via Cu braid. Liquid nitrogen is pumped into the reservoir using a recirculator designed and built elsewhere [100]. Sample temperatures of ~175 K can be attained using this cooling method. Initial sample cooling, from room temperature to ~200 K, takes between 2 and 3 hours; however, once cooled, the sample will cool from 900 to 200 K in about 5 minutes.

The hydroxybenzenes used in this study (phenol, catechol, resorcinol, hydroquinone, and pyrogallol) are reagent grade. All the chemicals are obtained from and specified as 99% pure. These compounds are used without further purification except to pump out the sample bulbs overnight on the gas manifold. The purity of each compound is confirmed in-house at the Chemistry Department Instrument Services Facility using a solid probe, Finnigan 4000 quadrupole mass spectrometer. The purity is also confirmed by gas phase mass spectrometry *in situ* using a UTI 100C quadrupole mass spectrometer and compared with reference spectra. The mass spectra of individual compounds are presented and discussed in subsequent chapters.

Between experiments the sample is cleaned as described previously, and prior to each exposure to a hydroxybenzene, is cooled to 200 K. Thermal desorption measurements are done using a UTI 100C quadrupole mass spectrometer interfaced to an Electra 286 personal computer and a commercial temperature controller [101]. The computer program used to acquire the thermal desorption data is described in Appendix A of this dissertation. The computer allows essentially simultaneous detection of up to eight masses as a function of time and temperature.

The mass spectrometer ionizer is in line of sight with the crystal and about 5 cm removed. The ionizer is partially enclosed by a concave stainless steel disk. A 1 cm diameter hole is cut in the center of the disk, and the crystal is aligned directly in front of this hole. This arrangement ensures that only molecules desorbing from the crystal surface reach the ionizer. A detailed schematic diagram of this arrangement is shown in Figure 6.

The sample temperature and the linear heating rate are controlled by a commercial temperature controller whose function is described elsewhere [101]. The feedback circuit, which controls the sample temperature, ramps linearly in millivolts [101]. Figure 7 shows the relationship between temperature and voltage over the temperature range of interest i.e., 200 to 900 K. The sample heating rate for all the compounds is 7 K/s. Since the conversion between millivolts and temperature is essentially linear for the Cr-Al thermocouple, the sample heating rate remains constant over the temperature range of interest.

The EELS experiments are performed using a commercial spectrometer [102]. Energy loss measurements are recorded in the specular direction with the crystal temperature at ~200 K after flashing to the pre-determined temperatures. The above procedure produces changes in the surface order and reflectivity of the crystal which are characterized by a

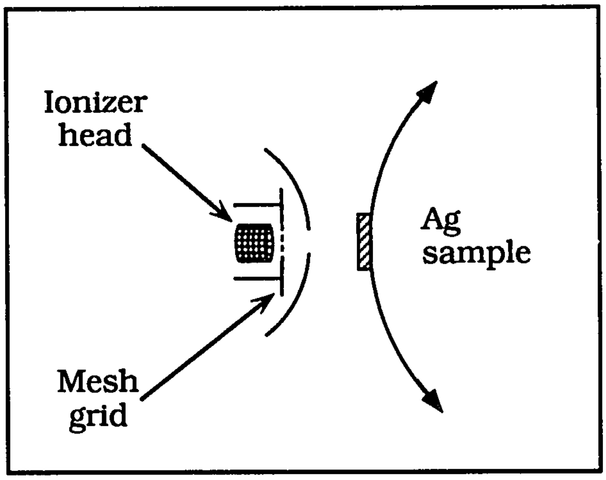

Figure 6. Schematic diagram of the crystal and mass spectrometer ionizer arrangement.

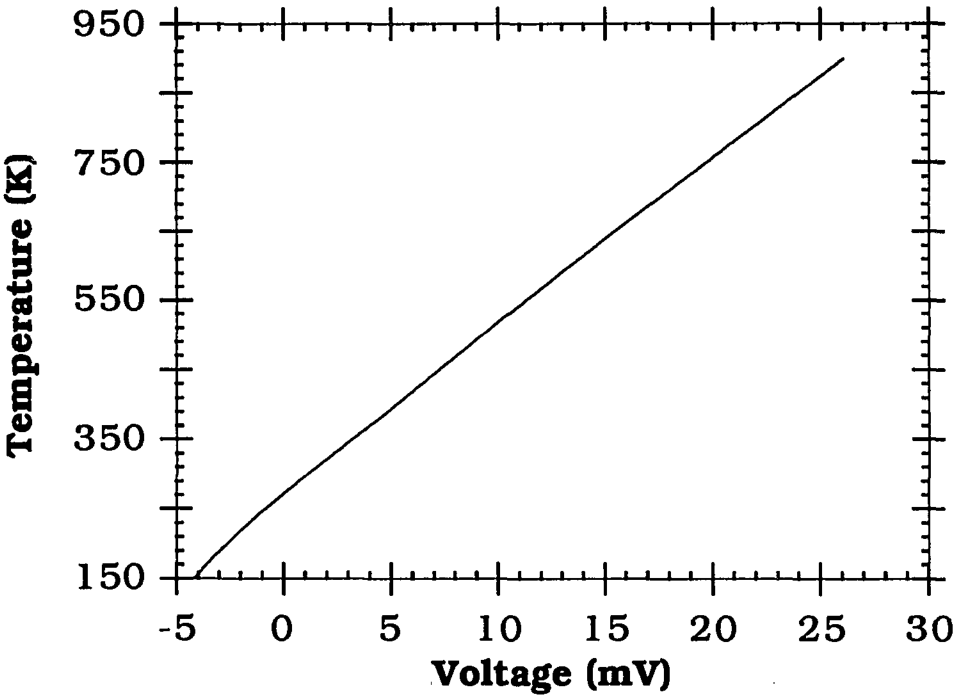

Figure 7. Temperature (K) vs. voltage (mV) curve for Cr-Al thermocouple wires.

change in the intensity of the elastic peak. No adjustments are made to the incident beam energy to lessen the effects due to these changes (i.e., the beam energy is kept constant at 5.0 eV throughout the experiments); however, minor focusing adjustments are made to maintain the resolution of the elastic peak. Typically, the elastic peaks have intensities between 1.5×10^4 and 9.0×10^4 counts/sec with resolutions of 81 cm^{-1} (10 meV).

The design, construction, assembly, and testing of the components of this system, including the computer software and hardware, constituted a major part of the Ph.D. effort of this author. This major task was accomplished primarily by the author, with assistance from several post-doctoral fellows, including Drs. J. L. Davis, J. Dyer and J. Burnett, and other graduate students in Dr. Thiel's research group. Although many components (including the UHV chamber, the EELS spectrometer, the retarding field analyzer, and the ion sputter gun) were purchased commercially or donated by industrial sources (i.e., Ford Motor Co. and the 3M Co.), considerable effort was still required to coordinate their successful incorporation into a single system and to bring them to an operational level. Other items, such as the gas handling system, gas doser, sample mount, and bakeout ovens, entailed even more effort since they were designed by the author and built under her supervision, in-house. The resultant system is a versatile and well-functioning apparatus which is very well suited for the study of hydroxybenzene surface chemistry.

PART 1:

THE SURFACE CHARACTERIZATION OF PHENOL ON Ag(111): AN EELS AND TDS STUDY

1. INTRODUCTION

Simple organic molecules can form ordered overlayers on Group VIII metal surfaces [1]. The formation of these overlayers is interesting since they serve as models or precursors to organic thin films or surface catalyzed reactions. The study of these simple systems is important to determine the nature of the more complex interaction between an organic thin film and a metal substrate. The chemical reaction and bond geometry between the analog molecules and the substrate model the interfacial chemistry between an organic thin film and a metal substrate. It is the interfacial chemistry that ultimately influences the macroscopic properties, such as adhesion, of the organic film and the metal substrate.

Phenolic functionalities are often added as adhesion promoters, that is, to enhance the adhesive bonding of a polymer to a substrate [1]. Rather than examine the surface characteristics of a complex phenolic resin, we have chosen to model such a system with the simple phenol molecule. Phenol may bond to the metal surface via two different mechanisms. One interaction involves bonding via the oxygen lone pair electrons and the second mechanism is the interaction of the π-ring system with the surface. Only a few studies of the surface characterization of phenol are reported in the literature. The adsorption and orientation of phenol has been studied previously on Cu(110) [2], Pt(111) [3], Mo(110) [4], Ni(110) [5], Ni(111) [6], and Pd(110) [1]. In all of these studies, the adsorption is characterized by a loss of the phenolic hydrogen to form a phenoxide species that is adsorbed with the ring plane nearly parallel to the surface for below saturation coverages. More recently, near-edge X-ray fine structure (NEXAFS) and X-ray photoelectron spectroscopy (XPS) studies indicate that below saturation coverages, the phenol aromatic ring tilts 50 ± 5° from the surface normal on Ag(110) [7]. However, on oxygen precovered Mo(110), evidence has been presented for a near perpendicular geometry, with bonding through the oxygen lone pair electrons [8].

This study examines the interaction of phenol on Ag(111), the closest-packed surface of silver, utilizing high resolution electron energy loss spectroscopy (EELS) and thermal desorption spectroscopy (TDS). Our objective is to characterize the reaction of phenol on Ag(111) to determine its bonding geometry, and to investigate any surface catalyzed reactions. The loss features observed in the EEL spectra are identified by comparison to vibrational mode assignments for phenol based on a normal mode analysis of benzene and by comparison to a previous surface vibrational study of phenol. The normal vibrational modes and frequencies of benzene are defined in the General Introduction of this dissertation (Table 1). The losses are further categorized into symmetry species of normal vibrations in different point groups. The two point groups chosen for comparison in this phenol study are C_{2v} and C_s, representing a perpendicular or parallel molecular orientation, respectively. Use of these point groups assumes that the surface imposes no specific site symmetry, yet does take into account the decrease in symmetry imposed by surface adsorption.

2. EXPERIMENTAL

The experiments are performed in a standard stainless steel ultrahigh vacuum (UHV) chamber with a typical base pressure of ~1 to 2×10^{-10} Torr. A schematic diagram of this chamber is shown in Figure 1. A complete description of this chamber is provided in the Experimental Procedures section of this text; however, details pertinent to the experiments with phenol will be included below.

The UHV chamber is equipped with a mass spectrometer, a retarding field energy analyzer for Auger electron spectroscopy (AES), a high resolution electron energy loss spectrometer (EELS), and an ion sputter gun and gas inlet manifold for Ar^+ bombardment. Further, a needle gas doser assembly is used to introduce the phenol into the chamber.

The phenol used in this study is reagent grade, purchased from Aldrich and specified as 99% pure. The phenol is used without further purification except to pump out the sample bulb through the gas manifold overnight. The purity of the phenol is confirmed in-house at the Chemistry Department Instrument Services Facility using a solid probe, Finnigan 4000 quadrupole mass spectrometer. The purity is also confirmed by gas phase mass spectrometry *in situ* using a UTI 100C quadrupole mass spectrometer. The mass spectra obtained are compared with reference spectra found in the literature. The phenol purity is confirmed both before and after experiments, *in situ*, to check for decomposition in the stainless steel gas handling lines. The gas phase mass spectrum obtained in this manner is shown in Figure 2, along with the corresponding reference cracking pattern.

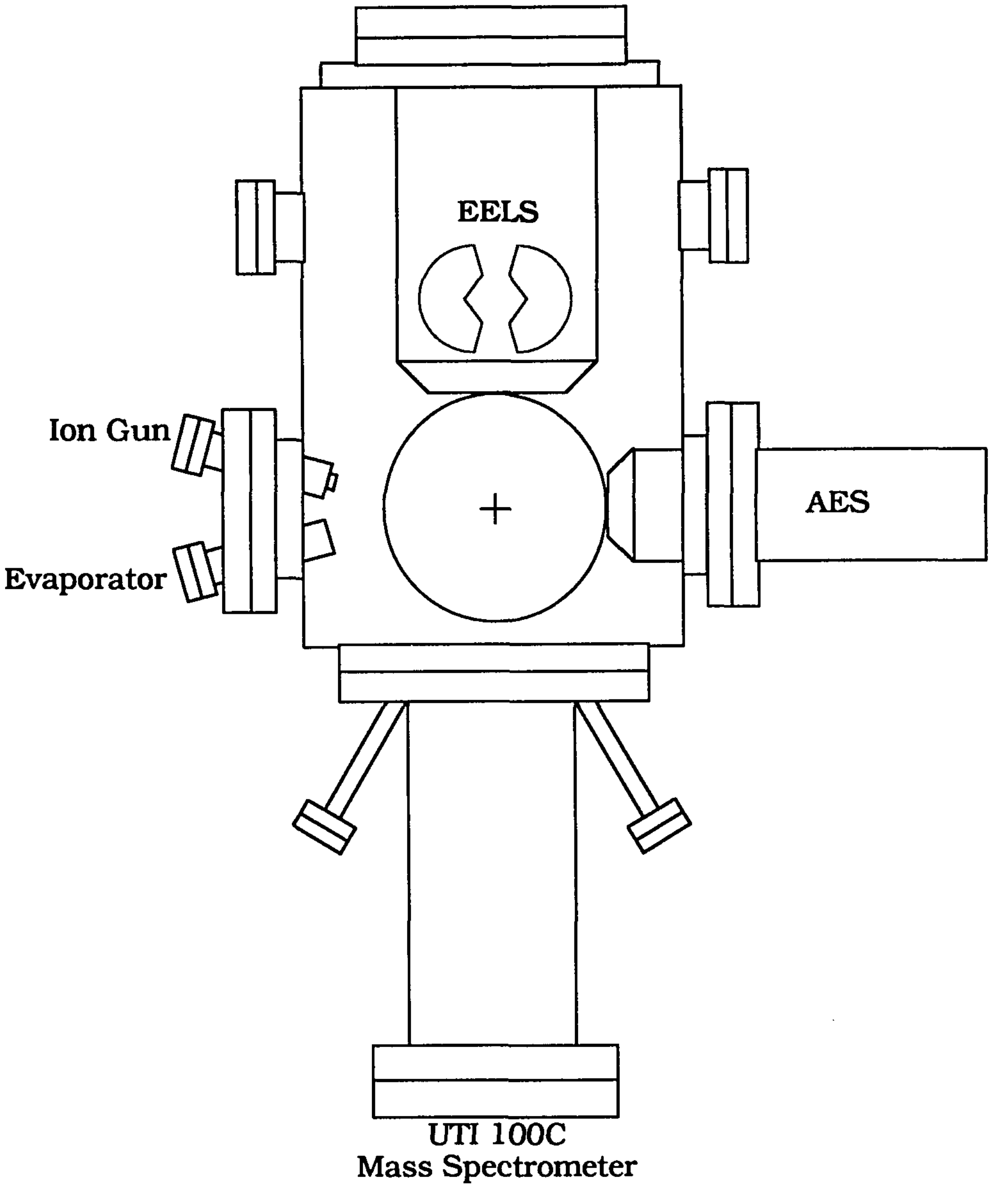

Figure 1. Schematic cross-section of the ultrahigh vacuum (UHV) chamber. The circle represents the focal circle, the circle around which the sample can rotate. The system is pumped by a 170 L/s turbomolecular pump (not shown) and a 400 L/s ion getter pump with a titanium sublimator.

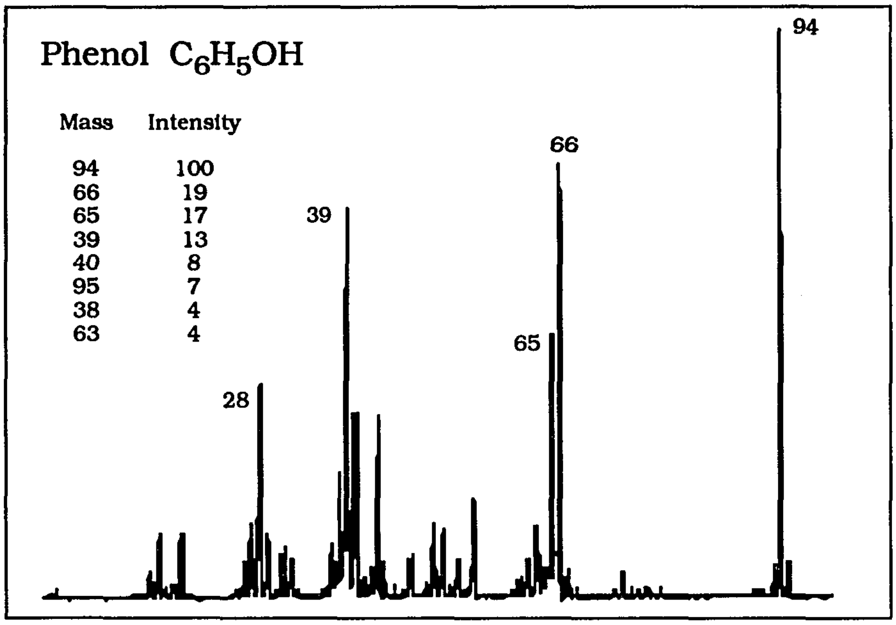

Mass	Intensity
94	100
66	19
65	17
39	13
40	8
95	7
38	4
63	4

Figure 2. Mass spectrum of phenol. Electron energy is 70 eV.

Although the relative intensities of fragments obtained *in situ* differ from those reported in the literature, all the prominent fragments are present.

Phenol is "highly toxic", a vesicant, and light sensitive [9]; thus, special precautions must be taken in its handling and storage. At room temperature, phenol is an amorphous solid. This solid can be warmed slightly in a warm water bath and transferred into the sample bulb using a pipette. The phenol is transferred into the sample bulb under a nitrogen atmosphere in a glove bag. The glass sample bulb is then wrapped with aluminum foil to keep out light. The unused phenol must be refrigerated.

The phenol is introduced into the UHV chamber via a syringe needle doser; that is, an open capillary tube with an inner diameter of 0.047 inch. The exposures are expressed in units of Langmuir (L, $1L = 10^{-6}$ Torr*s), calculated by multiplying the background pressure during exposure by the time of the exposure. We assume that the units are proportional to the integrated flux, and thus, are still a useful, although qualitative, measure of the true exposure. Phenol exposures are 20 s in duration, and typically, the chamber background pressure increases to $\sim 3 \times 10^{-8}$ Torr during exposure, thus, an exposure of 0.60 L.

3. RESULTS

3.1. Thermal Desorption Spectroscopy

The thermal desorption spectrum following phenol exposure at 200 K is shown in Figure 3. Only one exposure is shown since all other exposures produce the same spectrum. Two traces are shown in Figure 3, one for mass 94 and one for mass 2. Trace (a) represents mass 2, H_2^+, which is monitored to detect any hydrogen loss from the phenol. Trace (b) is for mass 94, representing the molecular fragment, $C_6H_6OH^+$, the most intense fragment in the phenol cracking pattern.

Only one feature is observed in the TDS spectra and it appears at 240 K. This peak represents a saturated state since increasing the exposure does not increase the area under the peak. Experiments monitoring other characteristic phenol fragments yield equivalent spectra to phenol (mass 94). That is, no different desorption features from masses 66, 65, 39, 40, 95, 38, and 63 are observed other than those due to cracking of phenol in the mass spectrometer ionizer. Thus, since all other fragments produce identical spectra, this 240 K peak suggests molecular desorption. The desorption energy is estimated to be 14.32 kcal/mole, assuming first order kinetics and using an approximate equation for desorption energy [10].

In adsorption experiments, mass fragments characteristic of phenol are monitored during a 20 s (~0.06 L) exposure to phenol. The results of the adsorption experiments indicate the steady evolution of dihydrogen (H_2^+, mass 2) from the onset of the dose. Second, we observe an initial onblast evolution of carbon monoxide (CO^+, mass 28) followed by the intensity

Figure 3. Thermal desorption spectra of (a) hydrogen and (b) hphenol from Ag(111). The spectra are obtained by monitoring mass 94 ($C_6H_5OH^+$) and mass 2 (H_2^+). Spectra equivalent to (b) are obtained if other, less-intense fragments are monitored. The sample heating rate is 7 K/s.

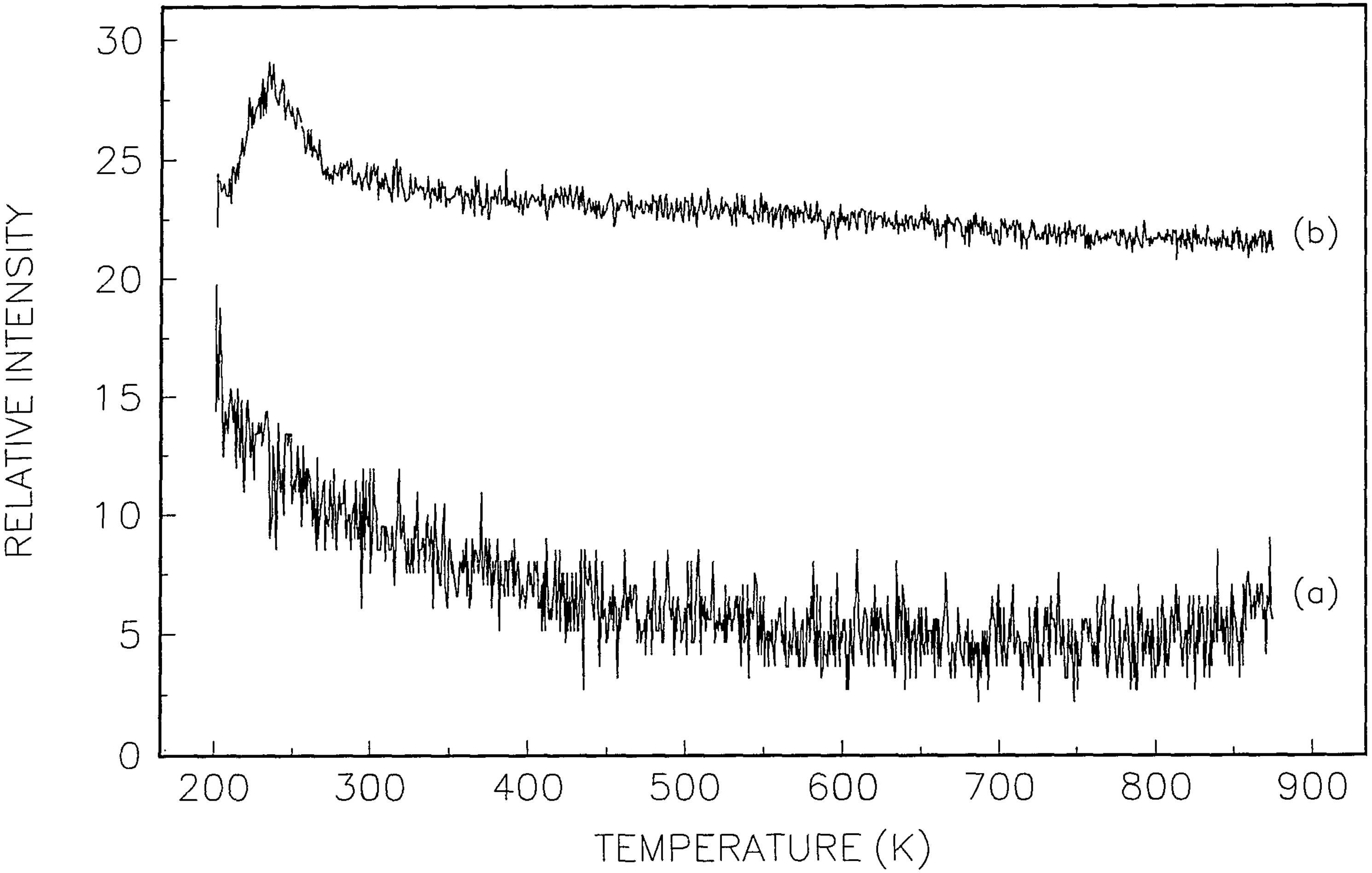
RELATIVE INTENSITY
0
5
10
15
20
25
30
200
300
400
500
600
700
800
900
TEMPERATURE (K)
(a)
(b)

becoming constant, and we observe a slow increase in water (H_2O^+, mass 18) intensity, followed by its leveling off. The signal intensities of water and carbon monoxide level off at the same time. We suspect that these fragments are due to displacement from the chamber walls, and do not originate from the phenol itself. Finally, we observe a steady increase in the signal intensities of phenol ($C_6H_6OH^+$, mass 94) and all other major fragments in the cracking pattern of phenol, i.e., 66, 65, 39, 95, 38, and 63. Because of the steady increase in signal intensities of these fragments, we conclude that phenol adsorbs molecularly on the Ag(111) surface.

3.2. Electron Energy Loss Spectroscopy

Figure 4 shows EEL spectra for the deposition of phenol on Ag(111). Curve (a) represents deposition of phenol at 200 K, curve (b) is the spectrum after heating the crystal to 300 K, and curve (c) depicts the spectrum following crystal heating to 600 K. The spectra shown are representative of several spectra taken at different times, and the loss frequencies reported in Table 1 are average values. Thus, the frequencies in Table 1 may not be an exact match to those of Figure 4.

The phenol EEL spectra are rich in that at least 6 loss features can be identified. However, at 200 K, only four of these features are prominent. The loss feature at 550 cm^{-1} is associated with the skeletal structure of the aromatic ring, and is assigned to a combination of out-of-plane skeletal vibrations and radial skeletal stretches. A very strong feature, observed at 750 cm^{-1}, is assigned to a combination of the δ(CH) deformation mode and radial skeletal stretches of the aromatic ring. This peak indicates

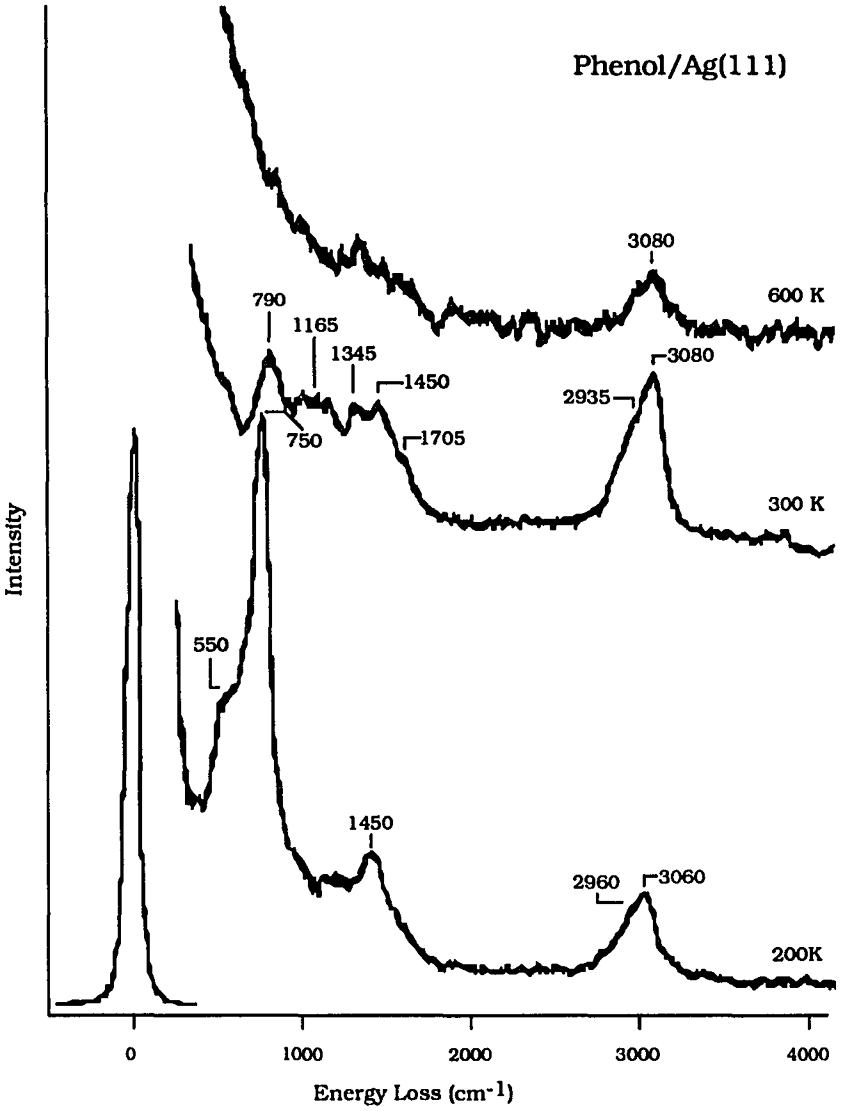

Figure 4. Electron energy loss spectra of phenol on Ag(111) at (a) 200 K, (b) 300 K and (c) 600 K. The vibrational mode assignments are summarized in Table 1.

Table 1. Vibrational mode assignments for phenol on Ag(111). Symmetry species for the C_{2v} and C_s point groups are presented. The shaded regions indicate symmetry species that represent totally symmetric representations of the respective point groups *and* obey the metal-surface selection rule.

[a] Reference [11].
[b] Reference [3].
[c] This work.
[d] Reference [13].
[e] Reference [14].
[f] Reference [12].

Mode #	Symmetry Species		Phenol IR freq. (cm^{-1})[a]	Intensity[a]	Phenol/ Pt(111) (electrode)[b]	Phenol/ Ag(111)[c]	Thiophenol IR freq. (cm^{-1})[a]	Thiophenol/ Pt(111) (electrode)[d,e]	Thiophenol/ Ag(111) (electrode)[e]	Thiophenol/ Mo(110)[f]
	C_{2v} (⊥)	C_s (//)								
1	a_1	a'	810	s		750/790	1093			
2	a_1	a'	3076		3020	2935-3060	3056	3057	3070	3105
3	b_2	a"	1313	w			1272			
4	b_1	a"	688	s	637		689	726	739	750
5	b_1	a"	978	vw			991	1000	1036	1035
6a	a_1	a'	526	m		550	698	726	739	750
6b	b_2	a"	617	w			617			
7a	a_1	a'	3030	sh	3020	2935-3060	412			
7b	b_2	a"	3044				3048	3057	3070	3105
8a	a_1	a'	1604	vs	1620	1705	1582	1516	1590	1510
8b	b_2	a"	1596	vw			---			
9a	a_1	a'	1167	m	1130	1165	1182	1145	1167	
9b	b_2	a"	1145	m			1159			
10a	a_2	a"	825	m			834			
10b	b_1	a"	241				185			
11	b_1	a"	749	vs	787	750/790	736			
12	a_1	a'	999	m			1002	1000	1036	1035
13	a_1	a'	1259	vs	1259	1345	3037	3057	3070	3105
14	b_2	a"	1333-1376	s	1370		1329			
15	b_2	a"	408				278			
16a	a_2	a"	410	w			---			
16b	b_1	a"	500	s	450	550	464	395	430	
17a	a_2	a"	958				960			
17b	b_1	a"	881	m	890		901			
18a	a_1	a'	1026	m	981		1026	1000	1036	1035
18b	b_2	a"	1071	s			1072			
19a	a_1	a'	1497	vs	1480	1450	1482	1428	1473	1510
19b	b_2	a"	1465	vs			1445			
20a	a_1	a'	3091	w	3020	2935-3060	3086	3057	3070	3105
20b	b_2	a"	3048	w			---			
ν_{OH}	a_1	a'	3623	vs			(ν_{SH}) 2575			
β_{OH}	b_2	a"	1180-1235	vs			(β_{SH}) 914			
γ_{OH}	b_1	a"	300				---			

aromaticity of the molecule on the surface. The third identifiable peak in curve (a) appears at 1450 cm^{-1}, and is assigned to the ν_{CC} stretching mode. Finally, the peak appearing in the range between 2960 and 3060 cm^{-1} can be assigned to the ν_{CH} stretching mode. The low frequency of this peak is indicative of aromatic C-H stretches.

The 300 K phenol EEL spectrum depicted in curve (b) is quite similar to that of the 200 K spectrum; however, some changes are apparent. For example, the loss feature at 550 cm^{-1} has all but disappeared. Second, the peak at 750 cm^{-1} is shifted to a higher frequency of 790 cm^{-1} and has decreased considerably in intensity. Further, at least two more features, appearing at 1165 and 1345 cm^{-1}, can be identified. The loss feature at 1165 cm^{-1} is assigned to β_{CH} bending vibrations, and that at 1345 cm^{-1} is tentatively assigned to the $\nu_{C\text{-}OH}$ stretching mode. Normally, this mode appears at ~1260 cm^{-1} as noted in the IR literature [11]. The ν_{CC} stretching mode appearing at 1450 cm^{-1} has not changed in frequency from the previous spectrum; however, it has decreased in intensity. Another new peak can be identified in the 300 K spectrum, appearing as a shoulder at ~1705 cm^{-1}. Like the preceding 1450 cm^{-1} feature, this peak is assigned to the ν_{CC} stretches of the carbon ring structure. Finally, the last feature in the 300 K spectrum occurs at 3080 cm^{-1} with a low frequency shoulder at ~2935 cm^{-1}, corresponding to the ν_{CH} stretching mode.

After heating the crystal to 600 K, the EEL spectrum is almost featureless as shown in curve (c). At this temperature, only one loss feature can be identified, the ν_{CH} stretch occurring at 3080 cm^{-1}. This peak is most likely due to hydrocarbon residue, presumably due to decomposition of phenol on the surface.

4. DISCUSSION

This study allows the identification and structural characterization of phenol on the Ag(111) surface. As is discussed in detail below, TDS results indicate molecular desorption (i.e., retention of aromaticity), as do features in the EEL spectra at temperatures below 600 K. Further, although the TDS and EELS results seem to indicate no dehydrogenation (i.e., O-H bond scission) upon phenol adsorption, the possibility is not ruled out completely. Finally, a temperature-dependent model of the preferred orientation is proposed.

4.1. Retention of Aromaticity

Phenol adsorbs associatively on the Ag(111) surface at 200 K. This associative adsorption is evidenced in adsorption experiments, as well as in the molecular desorption observed in the TDS experiments. Molecular desorption is inferred since mass 94 represents the molecular fragment ($C_6H_5OH^+$) and no different desorption features arising from other characteristic fragments are observed.

The product of this molecular adsorption is phenol, as shown by the EEL spectra. Table 1 summarizes the observed losses in the EEL spectra, as well as their assignments. All phenol vibrational mode assignments are made by comparison to the normal modes of the benzene molecule as described in the Introduction of this dissertation. Thus, the phenol assignments are numbered according to benzene vibrational mode convention. Further, vibrational assignments for phenol [3] and thiophenol

[12-14] determined in previous studies are included in Table 1 for comparison. The mere fact that all of the observed loss features correspond to normal modes of the benzene molecule is a strong indication of the aromatic nature of the adsorbed species.

At least two of the loss features observed in the EEL spectra, at both 200 and 300 K, indicate aromatic character in the adsorbed species. The very strong feature centered between 750 - 790 cm^{-1} is associated with the ν_1 and ν_{11} vibrations of the benzene ring. The ν_1 mode represents radial skeletal vibrations, or "ring breathing" modes, whereas, the ν_{11} mode originates from γ_{CH} out-of-plane bending vibrations. Further, losses in this frequency range can indicate the type of substitution in benzene derivatives, and in this instance, indicates a mono-substituted benzene [15]. Thus, the intensity and frequency of this loss is a strong indication of an aromatic species.

Further indication of the aromatic nature of the adsorbed molecule is evidenced in the ν_{CH} stretch centered between 2960 and 3060 cm^{-1} in both the 200 and 300 K spectra. This feature is assigned to the ν_2, ν_{7a}, and ν_{20a} vibrational modes corresponding to the benzene ring. Generally, ν_{CH} stretches for aromatic and ethylinic C-H bonds occur in the range between 3030 and 3080 cm^{-1}, whereas aliphatic and acetylinic C-H stretches occur at much lower or higher frequencies, i.e., 2840 to 3000 cm^{-1} for aliphatic ν_{CH} stretches and 3250 to 3340 cm^{-1} for acetylinic ν_{CH} stretches [15]. Also, it is common to observe multiple peaks in this region [15] as is present in these EEL spectra. Therefore, due to the frequency of the observed loss feature, the surface species is indeed aromatic at these temperatures.

After heating to 600 K, almost all the vibrational features disappear from the EEL spectrum. The only remaining peak at 3080 cm^{-1} is assigned to a ν_{CH} stretch. As described earlier, the frequency of this stretch indicates either ethylinic or aromatic ν_{CH} stretches [15]. Since there is no further evidence of any aromatic character to the surface species, due to the absence of the 750 cm^{-1} loss feature, we assume the high frequency stretch to be ethylinic in nature. This mode assignment agrees with other studies of adsorbed ethylene [16-18], propylene [19] and acetylene [20] di-σ-bonded to the surface. Thus, we conclude that the ν_{CH} loss originates from an ethylinic hydrocarbon residue on the surface.

4.2. Dehydrogenation

When considering the adsorption of phenol, there is a possibility of O-H bond scission, or dehydrogenation, even when the aromaticity of the ring is maintained. Is the O-H bond broken as the phenol adsorbs on the surface? If so, what is the fate of the hydrogen? Does it recombine with phenoxide, forming phenol? Does it form hydrogen gas and desorb? If no O-H bond scission occurs, how is the phenol bonded to the surface? Evidence in both the TDS and EELS results suggest no dehydrogenation of phenol upon adsorption at 200 K.

At first glance, the TDS results suggest no O-H bond scission. If dehydrogenation occurs, followed by desorption of H_2, we might expect the TDS trace of mass 2 to show at least one desorption feature. As shown in Figure 3, no H_2 evolution is apparent at temperatures up to 900 K. Previous studies of phenol and thiophenol on Mo(110) suggest O-H, (S-H) bond scission and the formation of surface phenoxide (phenyl thiolate), evidenced by the desorption of dihydrogen gas [12, 21]. The absence of a separate desorption feature for mass 2, however, does not unambiguously rule out dehydrogenation. It is possible that the O-H bond breaks upon adsorption, but the hydrogen remains coadsorbed on the surface and preferentially recombines with the phenoxide which then desorbs as phenol. This explanation is only postulated at this point, but could be examined more closely by isotopic exchange experiments.

All the EEL spectra evidence an absence of an ν_{OH} stretch. If present, this loss feature would appear at about 3623 cm^{-1} [11]. Three possible explanations exist for the absence of this feature: (a) O-H bond scission upon adsorption, (b) hydrogen bonding on the surface or (c) parallel orientation of the O-H bond in accordance with the metal-surface selection rule. Only one of these possibilities favors O-H bond scission. If O-H bond scission occurs, we would expect no ν_{OH} stretch to appear in the EEL spectra [3]. Figure 5 shows how the surface phenoxide species might appear on Ag(111). As noted in the TDS experiments, we observe no conclusive evidence for O-H bond scission; however, the absence of an ν_{OH} loss feature supports the idea of phenoxide-hydrogen recombination and desorption.

A second possibility, hydrogen bonding between phenol molecules, could also explain the absence of a ν_{OH} stretch. Since hydrogen bonded O-H bonds have small scattering cross sections in EELS and/or IR [22, 23], one might expect to observe only a very weak ν_{OH} stretch, or none at all. Evidence of hydrogen bonding between adsorbed phenol molecules has been

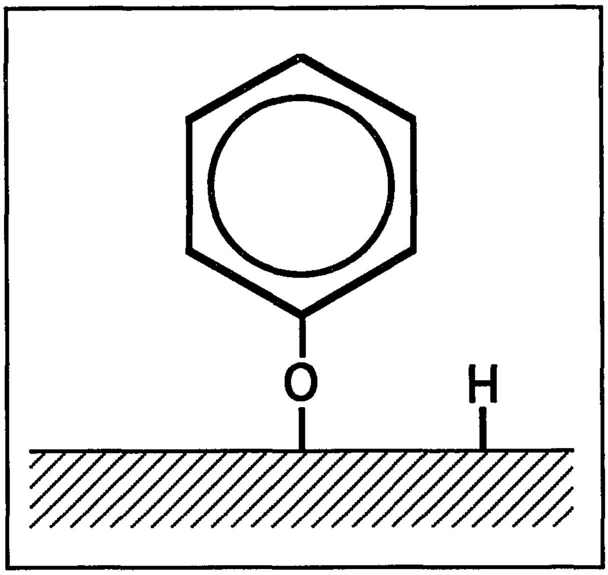

Figure 5. Diagram of the surface phenoxide species on Ag(111).

observed previously [6, 7]. Figure 6 shows what hydrogen bonded phenol species might look like on the surface. Thus, the absence of a ν_{OH} stretch does not conclusively indicate O-H bond scission.

Finally, in accordance with the metal-surface selection rule, the orientation of the O-H bond may make the ν_{OH} stretch essentially invisible in the EEL spectra. This possibility can be interpreted in two ways: either the entire phenol molecule is oriented parallel to the surface, or at least the O-H bond is parallel to the surface. Figure 7 shows these two possible orientations. Briefly, the metal-surface selection rule states that only vibrations with a component of the dipole moment change perpendicular to the surface are observed in EEL spectra. In either of the above cases, the O-H bond would be parallel to the surface, and the ν_{OH} stretch would not be observed in the EEL spectra. Therefore, again the absence of an ν_{OH} stretch in the EEL spectra does not conclusively indicate O-H bond scission.

The above arguments, based on TDS and EELS results, seem to favor the hypothesis that no dehydrogenation or O-H bond scission occurs. Instead, the phenol molecule remains intact upon adsorption. Further, either the orientation of the O-H bond to the surface or hydrogen bonding between phenol molecules cause the ν_{OH} stretch to be essentially absent from the EEL spectra. Dehydrogenation, however, cannot be completely discounted until isotopic exchange experiments are done on this system.

4.3. Ring Orientation and Normal Mode Assignment

When considering possible molecular orientations of phenol on the surface, we can envision two scenarios. In the first scenario, we assume

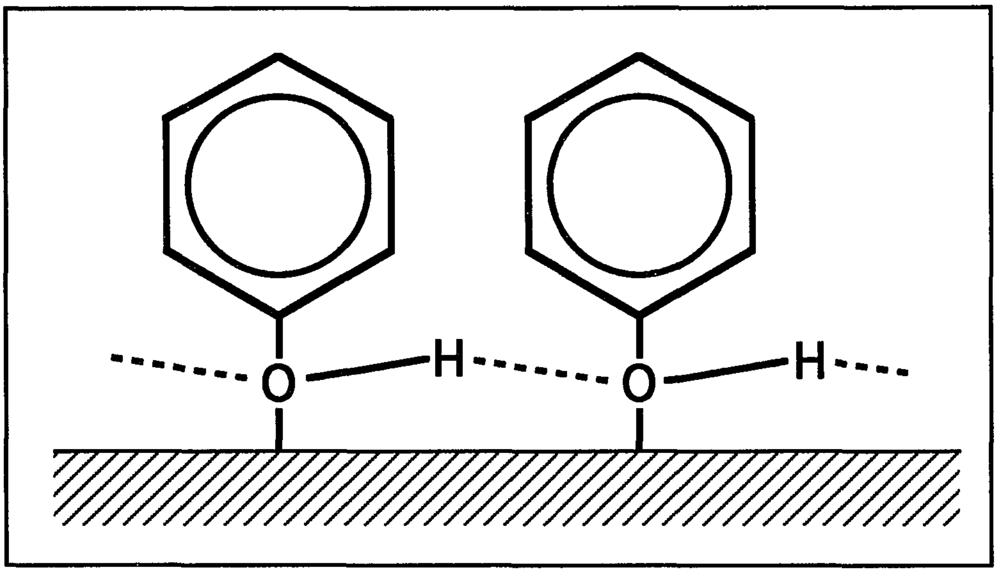

Figure 6. Diagram of hydrogen bonded phenol on Ag(111).

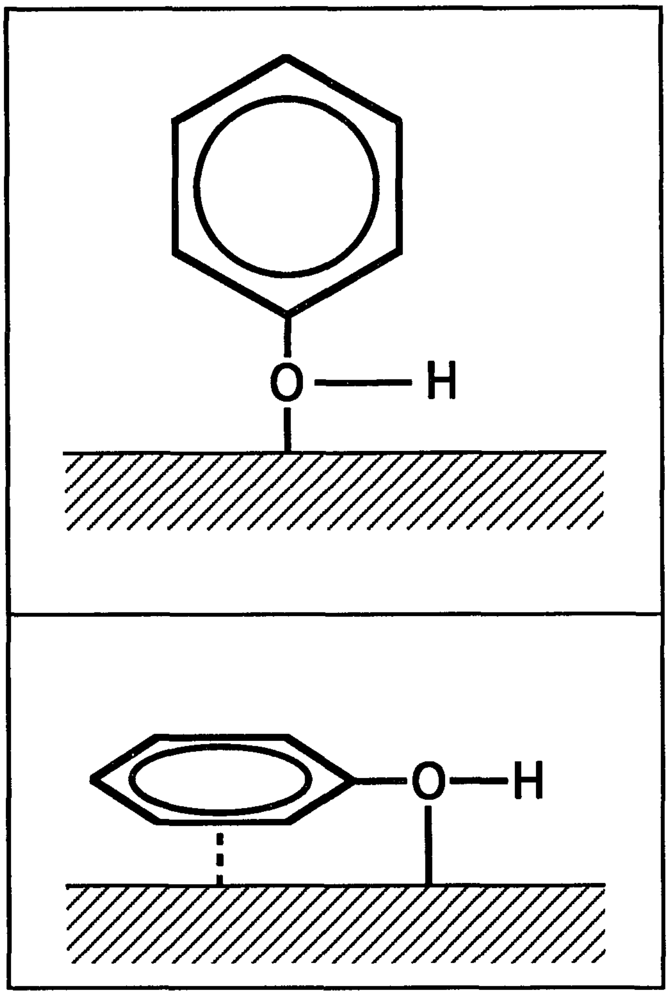

Figure 7. Two possible orientations in which the O-H bond axis lies parallel to the surface.

that only one chemical species is present on the surface at all times. Further, we assume that this species adopts a single, well-defined molecular orientation, i.e., either perpendicular, inclined or parallel. The second scenario would allow at least two different species to exist on the surface as a function of temperature. Table 1 shows the normal mode assignments for the EELS loss features.

Evidence for the "one species" scenario is found by categorizing the vibrational modes into specific point group symmetries and choosing the orientation that best agrees with that specific assignment. Table 1 shows the specific point groups to which the loss features in the EEL spectra can be assigned. Most of the loss features observed in the EEL spectra, both at 200 and 300 K, can be assigned to vibrational modes in accordance with the C_{2v} symmetry, i.e., the symmetry group representing a perpendicular orientation of the phenol molecule. The assignment of this symmetry point group assumes no perturbation from the adsorption site. The peak appearing at 550 cm^{-1} is assigned to the ν_{6a} vibrational mode of benzene. This mode is due to in-plane skeletal bends and belongs to the totally symmetric representation of the C_{2v} point group. The very strong feature centered between 750 - 790 cm^{-1} is associated with the ν_1 vibration of the benzene ring. The ν_1 mode represents radial skeletal vibrations, or "ring breathing" modes, and belongs to the totally symmetric representation of the C_{2v} point group. The feature at 1165 cm^{-1} appears only in the 300 K EEL spectrum, and is assigned to the ν_{9a} vibrational mode of the benzene ring which corresponds to β_{CH}, the out-of-plane bending mode. The peak at 1345 cm^{-1} can be assigned to ν_{13}, the $\nu_{C\text{-}OH}$ vibrational mode of a substituted benzene molecule. This feature appears at a higher frequency than the expected 1259 cm^{-1} in the infrared spectrum of the free molecule [11], which may be caused by a perturbation due to bonding to the surface [24]. Finally, the ν_{CC} stretch at 1450 cm^{-1} is assigned to the ν_{19a} vibrational mode of benzene. These assignments, ν_{9a}, ν_{13}, and ν_{19a}, all correspond to totally symmetric representations of *both* the C_{2v} and C_s point groups, but those C_s modes do not obey the surface selection rule, and therefore should not be visible in the EEL spectra. The ν_{CH} feature centered between 2960 and 3060 cm^{-1} is assigned to the ν_2, ν_{7a} and ν_{20a} vibrational modes. All three vibrational modes belong to the totally symmetric representations of *both* the C_{2v} and C_s point groups; however, again, those of C_s symmetry do not obey the surface selection rule. Thus, the point group assignments of these features indicate a perpendicular molecular orientation on the Ag surface. Figure 8a shows how a perpendicular orientation might appear on the surface.

At least two of the loss features, however, may be assigned to vibrational modes that belong *only* to totally symmetric representations of the C_s point group, i.e., the symmetry representing a parallel orientation on the surface. The peak centered at 750 - 790 cm^{-1} could also originate from ν_{11}, a γ_{CH} out-of-plane bend, and the peak appearing at 550 cm^{-1} from ν_{16b}, and out-of-plane skeletal bend. Further, as shown in Table 1, other loss features may be assigned to vibrational modes in the C_s point group; however, those modes do not obey the metal-surface selection rule, and would not be visible in the EEL spectra. A completely parallel orientation can be ruled out since only two of the six loss features belong to totally

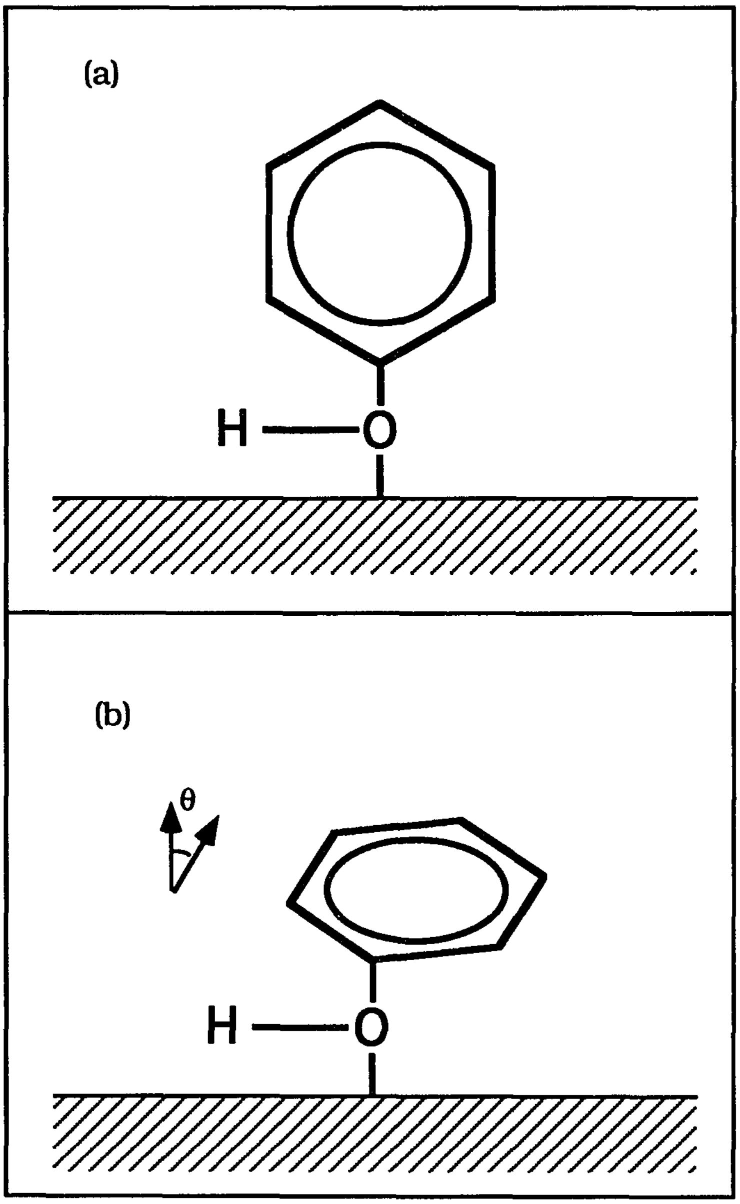

Figure 8. (a) Diagram of phenol in a perpendicular orientation, assuming no dehydrogenation.
(b) Diagram of phenol in an inclined orientation, at some angle, θ, from the surface normal.

symmetric representations of the C_s point group *and* obey the metal-surface selection rule. Thus, the presence and assignment of these two vibrational modes may only suggest some tilting of the phenol away from the surface normal. Figure 8b shows how a tilted orientation may appear on the surface.

In addition to this work on Ag(111), phenol adsorbed from an aqueous solution has been investigated [3]. The previous study suggests parallel adsorption on the surface based on EELS results and packing density calculations. Recall, a parallel orientation is synonymous with the C_s point group; however, all loss features in the previous study are assigned to vibrational modes in the C_{2v} point group, i.e., suggesting a perpendicular orientation. Confusion in the interpretation of EEL spectra arises from not carefully considering how surface adsorption reduces the symmetry of molecules. Therefore, all possible symmetries must be carefully considered and compared to determine the bonding geometry of the molecule on the surface.

The second scenario suggests that more than one species exists on the surface as a function of temperature. Figure 9 shows this temperature dependent model, assuming no O-H bond scission. In this model, phenol assumes a tilted orientation on the surface upon adsorption at 200 K. At this temperature, the most intense feature in the EEL spectrum appears at 750 cm^{-1}. As discussed earlier, this feature can be assigned to either ν_1 or ν_{11}, or it might possibly result from both of these vibrational modes. Because the frequency and intensity of this feature at 200 K most closely resembles that of ν_{11}, we shall assign it solely to the γ_{CH} out-of-plane bend.

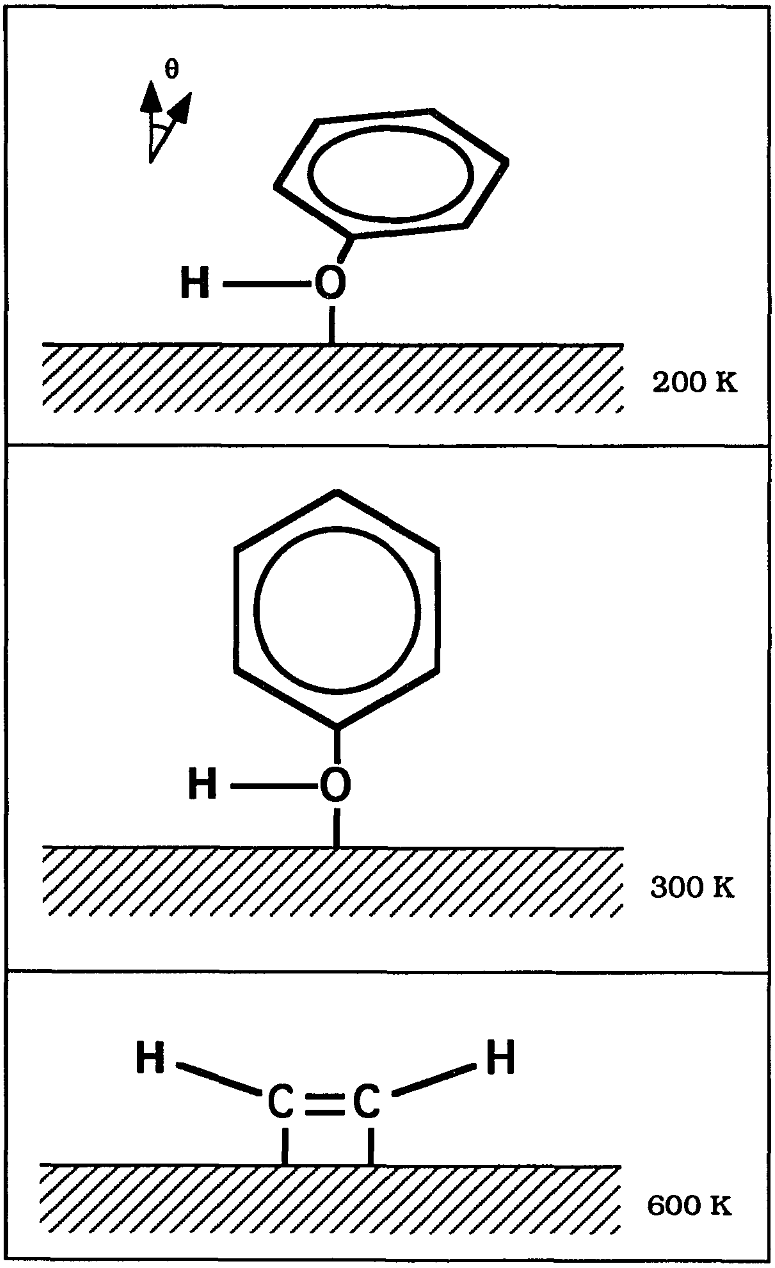

Figure 9. A proposed model for the temperature dependence of the orientation of phenol on Ag(111).

The symmetry species of ν_{11} belongs to a totally symmetric representation *only* of the point group C_s, thus suggesting a parallel orientation. However, since most of the features in the EEL spectrum at 200 K belong to totally symmetric representations of the point group C_{2v} (i.e., representing perpendicular orientation), we predict a tilted molecular orientation.

As the crystal temperature increases, changes in the vibrational spectra suggest a new molecular orientation. The TDS results indicate molecular desorption at 240 K; however, phenol is still present on the surface as evidenced in the EEL spectrum at 300 K. Also, by 300 K, the frequency of the 750 cm^{-1} shifts up to 790 cm^{-1}, and further, the intensity of this feature decreases significantly. This loss feature is now assigned solely to the ν_1 vibrational mode, the radial skeletal, or "ring breathing" mode. Again, this mode belongs to the totally symmetric representations of *both* the C_{2v} and C_s point groups; however, only the C_{2v} symmetry species obeys the surface selection rule. The C_{2v} point group represents a perpendicular orientation on the surface. Thus, by 300 K, the EEL spectrum suggests the phenol molecules assume a perpendicular orientation, as shown in Figure 9. This orientation change (i.e., from inclined to perpendicular) is similar to the parallel-to-edgewise (η_2) conversion observed for pyridine on Ni(100) [25].

By 600 K, only one feature remains in the EEL spectrum, appearing at 3080 cm^{-1}. As previously discussed, this peak is assigned to a ν_{CH} stretch, presumably due to a hydrocarbon residue remaining on the surface. Thus, by 600 K, either the phenol has molecularly desorbed or decomposed to only hydrocarbon fragments, as depicted in Figure 9.

The temperature dependent model just described suggests molecular desorption and irreversible decomposition of phenol on Ag(111). At 240 K, some phenol is molecularly desorbed and some phenolic species remains on the surface. By 600 K, only a hydrocarbon residue is evident on the surface. Phenol also undergoes molecular desorption and irreversible decomposition on Mo(110) [21]. On Mo(110), it is suggested that two species coexist on the surface, phenoxide and either phenoxide adsorbed at a different site or molecular phenol. Also, total decomposition to atomic constituents is observed on Mo(110), as indicated by XPS. We can only postulate what residue remains on Ag(111) at 600 K. Although our data do not unambiguously distinguish between a phenol or phenoxide species; however, it does suggest a change in orientation upon sample heating.

5. CONCLUSIONS

We identify and characterize phenol adsorbed on Ag(111) using thermal desorption and high resolution electron energy loss spectroscopies. Phenol is adsorbed associatively at 200 K and desorbs molecularly at 240 K. Neither the TDS or EELS data suggest dehydrogenation upon adsorption or molecular desorption at 240 K. The EEL spectra indicate that some phenol remains on the surface at 300 K, thus suggesting some irreversibly bound phenol. Decomposition to a hydrocarbon residue occurs by 600 K.

The vibrational losses observed in the EEL spectra can be assigned by comparison to normal vibrational modes of the benzene molecule and by comparison with assignments made by others of phenol or thiophenol. Upon adsorption at 200 K, the EELS loss features indicate an inclined orientation of phenol on the Ag surface. By 300 K, the orientation becomes perpendicular on the surface, and by 600 K, all evidence of phenol on the surface is gone.

REFERENCES CITED

1. M. G. Ramsey, G. Rosina, D. Steinmüller, H. H. Graen and F. P. Netzer, Surf. Sci. 232 (1990) 266.

2. N. V. Richardson and P. Hoffmann, Vacuum 33 (1983) 793.

3. F. Lu, G. N. Salaita, L. Laguren-Davidson, D. A.Stern, E. Wellner, D. G. Frank, N. Batina, D. C. Zapien, N. Walton and A. T. Hubbard, Langmuir 4 (1988) 637.

4. J. G. Serafin and C. M. Friend, Surf. Sci. 209 (1989) L163.

5. D. Steinmueller, M. G. Ramsey, F. P. Netzer and M. Neuber, Surf. Sci. 271 (1991) 567.

6. A. K. Myers and J. S. Benziger, Langmuir 5 (1989) 1270.

7. J. L. Solomon, R. J. Madix and J. Stöhr, Surf. Sci. 255 (1991) 12.

8. A. C. Liu, C. M. Friend and J. Stöhr, Surf. Sci. Lett. 236 (1990) L349.

9. Material Safety Data Sheet, Aldrich Chemical Co.

10. P. A. Redhead, Vacuum 12 (1962) 203.

11. G. Varsányi, Assignments For The Vibrational Spectra of Seven Hundred Benzene Derivatives, Volume 1, 1 (John Wiley & Sons, Inc., New York, 1974).

12. J. T. Roberts and C. M. Friend, J. Chem. Phys. 88 (1988) 7172.

13. D. A. Stern, E. Wellner, G. N. Saliata, L. Laguren-Davidson, F. Lu, N. Batina, D. G. Frank, D. C. Zapien, N. Walton and A. T. Hubbard, J. Am. Chem. Soc. 110 (1988) 4885.

14. J. Y. Gui, D. A. Stern, D. G. Frank, F. Lu, D. C. Zapien and A. T. Hubbard, Langmuir 7 (1991) 955.

15. E. Pretsch, T. Clerc, J. Seibl and W. Simon, Tables of Spectral Data for Structure Determination of Organic Compounds (Springer-Verlag, Berlin Heidlberg, 1983).

16. B. E. Bent, C. M. Mate, C.-T. Kao, A. J. Slavin and G. A. Somorjai, J. Phys. Chem. 92 (1988) 4720.

17. L. L. Kesmodel and J. A. Gates, Surf. Sci. 111 (1981) L747.

18. H. Ibach and S. Lehwald, J. Vac. Sci. Technol. 15 (1978) 407.

19. B. E. Bent, C. M. Mate, J. E. Crowell, B. E. Koel and G. A. Somorjai, J. Phys. Chem. 91 (1987) 1493.

20. L. L. Kesmodel, G. D. Waddill and J. A. Gates, Surf. Sci. 138 (1984) 464.

21. C. M. Friend in: Adsorption Structure of Organic Molecules on Mo(110), Vol. 17 (Springer-Verlag Berlin, Heidleberg, 1989) p. 67.

22. M. V. Thiel, E. D. Becker and G. C. Pimentel, J. Chem. Phys. 27 (1957) 486.

23. G. C. Pimentel and A. L. McClellan, The Hydrogen Bond (Reinhold, New York, 1960).

24. N. V. Richardson and N. Sheppard in: Normal Modes at Surfaces, Vol. 1 (Plenum Press, New York, 1987) p. 1.

25. G. R. Schoofs and J. B. Benziger, J. Phys. Chem. 92 (1988) 741.

PART 2:

A COMPARATIVE EELS AND TDS STUDY OF CATECHOL, RESORCINOL AND HYDROQUINONE ON Ag(111)

1. INTRODUCTION

Since phenolic functionalities are often added to monomeric molecules as adhesion promoters [1, 2], phenol-like molecules serve to model the metal-adhesive bonding interaction. A phenolic functionality is defined as a compound similar to phenol, i.e., hydroxyl groups attached to a benzene ring. The number and position of the hydroxyl substituents on the benzene ring may also affect the metal-adhesive bonding properties. To examine this phenomenon, we investigate three phenolic compounds, each with two pendant hydroxyl groups. The model compounds include catechol (*ortho*-di-hydroxybenzene), resorcinol (*meta*-di-hydroxybenzene) and hydroquinone (*para*-di-hydroxybenzene). The structures of these compounds are shown in Figure 1.

The surface reactions and bonding orientations of these model compounds are interesting to compare to those of phenol, the mono-hydroxybenzene. Like phenol, the di-hydroxybenzene molecules may bond to the metal surface via two different mechanisms. One mechanism involves the oxygen lone pair electrons and the second is the interaction of the π-ring system with the surface. Very few studies of the surface characterization of these compounds can be found in the literature. Catechol has been studied previously on Pt electrode surfaces using high resolution electron energy loss spectroscopy (EELS) and packing density calculations based on Auger electron spectroscopy (AES) and cyclic voltammetry (CV) measurements. In these studies. the catechol is deposited on the surface from aqueous solutions. Results of these studies indicate

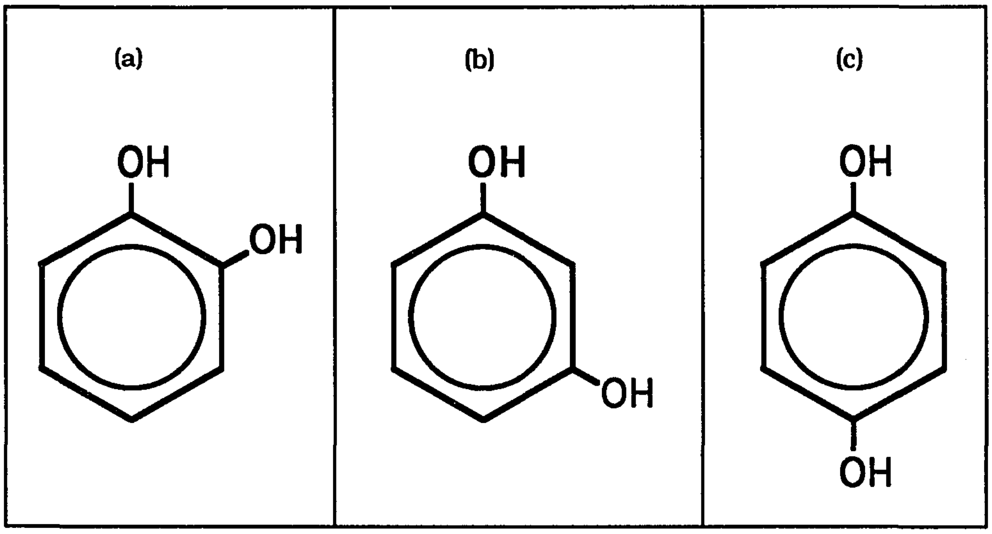

Figure 1. Diagram of the *o*-, *m*- and *p*-dihydroxybenzene molecules.
(a) *o*-dihydroxybenzene (catechol).
(b) *m*-dihydroxybenzene (resorcinol).
(c) *p*-dihydroxybenzene (hydroquinone).

that in adsorbed layers one molecule thick, the aromatic ring of catechol orients parallel to the Pt(111) and (100) electrode surfaces [3, 4].

Some studies of hydroquinone are found in the literature. Thin-layer electrochemical (TLE) studies of hydroquinone on Pt surfaces, deposited from aqueous solution, suggest that hydroquinone's orientation depends on several different factors, including solution concentration [5], surface roughness [6] and temperature [7]. Hydroquinone adopts a vertical, or "edgewise", orientation on smooth Pt surfaces and if deposited from solutions of concentrations greater than 1 mM, whereas on roughened surfaces or if deposited from solutions of concentrations less than 1 mM, a flat orientation is observed [5, 6]. Vibrational spectroscopic studies of hydroquinone on Pt(111) using EELS, in conjunction with packing density calculations by quantitative AES, indicate a loss of the phenolic hydrogens upon adsorption in a parallel orientation on the Pt surface [8]. No surface studies of resorcinol can be found in the literature at this time.

In this study, we investigate the interactions between catechol, resorcinol and hydroquinone with the Ag(111) surface using high resolution electron energy loss spectroscopy (EELS) and thermal desorption spectroscopy (TDS). Our objective is to characterize these interactions and to determine similarities and differences in their bonding geometry or reactivity. Our approach will be to compare the EEL spectra of these compounds to infrared data for benzene in order to identify and assign the observed vibrational modes. The normal vibrational modes of benzene, along with their frequencies, are defined in the General Introduction of this dissertation (Table 1). The EELS loss features observed for the di-hydroxybenzene molecules are further categorized into symmetry species of normal vibrational modes in different point groups. For these compounds, the point groups chosen for comparison include C_{2v}, C_{2v}^* and C_s, depending on the possible molecular orientations of the molecules on the surface. The difference between the C_{2v} and C_{2v}^* point groups is the different orientation of the twofold axis. These point groups are chosen with the assumption that the surface has no specific site symmetry.

2. EXPERIMENTAL

The experiments are performed in one standard stainless steel ultrahigh vacuum (UHV) chamber with a typical base pressure of ~1 to 2×10^{-10} Torr. A schematic diagram of this chamber is shown in Part I of this dissertation (Figure 1). A complete description of this chamber is provided elsewhere as well; however, details pertinent to the experiments with the di-hydroxybenzene compounds will be included below.

The compounds used in this study are reagent grade, purchased from Aldrich and specified as 99% pure. All compounds are used without any further purification except to pump out the sample bulb through the gas manifold overnight. The purity of each is confirmed in-house at the Chemistry Department Instrument Services Facility using a solid probe, Finnigan 4000 quadrupole mass spectrometer. The purity is also confirmed by gas phase mass spectrometry *in situ* using a UTI 100C quadrupole mass spectrometer. In the latter purity checks, a small stainless steel dosing needle directs the gas directly into the mass spectrometer ionizer. The mass spectra obtained are compared with reference spectra found in the literature. The compound's purity is confirmed both prior to and following experiments, *in situ*, to check for decomposition in the stainless steel gas handling lines.

The gas phase mass spectrum obtained for catechol is shown in Figure 2, with the corresponding reference fragmentation pattern. A mass spectrum of catechol is not available in the literature, therefore the solid probe mass spectrum is used for comparison purposes. Although the

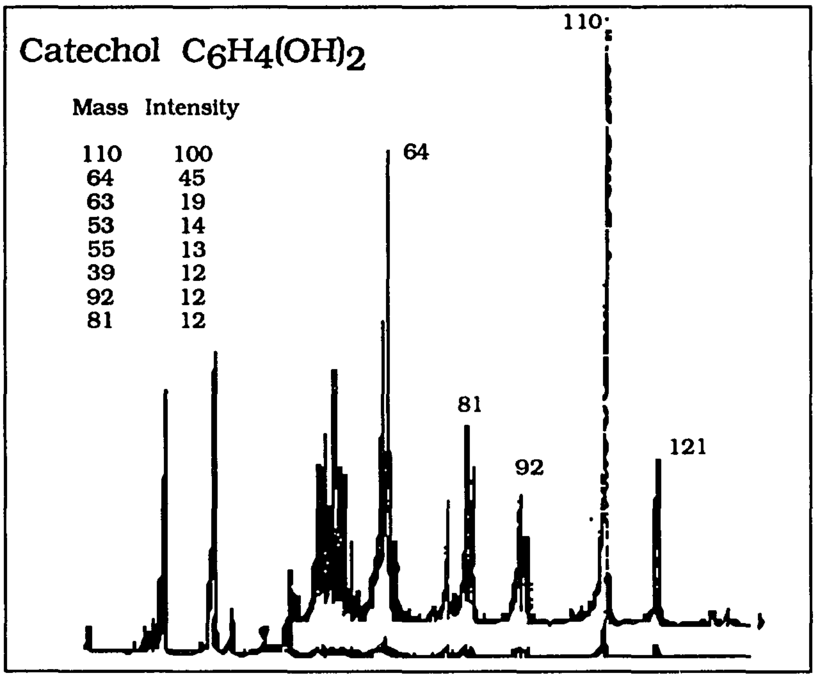

Mass	Intensity
110	100
64	45
63	19
53	14
55	13
39	12
92	12
81	12

Figure 2. Mass spectrum of catechol. Electron energy is 70 eV.

relative intensities of fragments obtained *in situ* differ from those observed in the solid probe spectrum, all the prominent fragments are present. Some extraneous peaks are visible in the gas phase mass spectrum (i.e., masses 121 and 82), however, these fragments decrease in intensity as the sample bulb is pumped out. Thus, the sample bulb is always pumped out to a pressure ≤0 mTorr before dosing the crystal.

Figures 3 and 4 show the gas phase mass spectra of resorcinol and hydroquinone with their reference fragmentation patterns, respectively. In both the resorcinol and hydroquinone mass spectra, we observe two extraneous peaks, masses 94 and 66, which are prominent fragments in the phenol cracking pattern. It is possible that some of the resorcinol and hydroquinone converts to phenol in the stainless steel gas line.

Special precautions must be taken when handling these di-hydroxybenzene compounds. All three compounds are light sensitive, and hydroquinone is also air sensitive [9]. Thus, the compounds are transferred into the sample bulbs under a nitrogen atmosphere, in a glove bag. The glass sample bulbs are wrapped with aluminum foil to avoid exposure to light.

The compounds are introduced into the UHV chamber via a syringe needle doser. The exposures are expressed in units of Langmuir (L, $1 \text{ L} = 10^{-6}$ Torr*s), calculated by multiplying the background pressure during exposure by the time of the exposure. We assume that the units are proportional to the integrated flux, and thus, are still a useful, although qualitative, measure of the true exposure. While a variety of exposures are probed in the TDS experiments, only a single exposure is used in the EELS

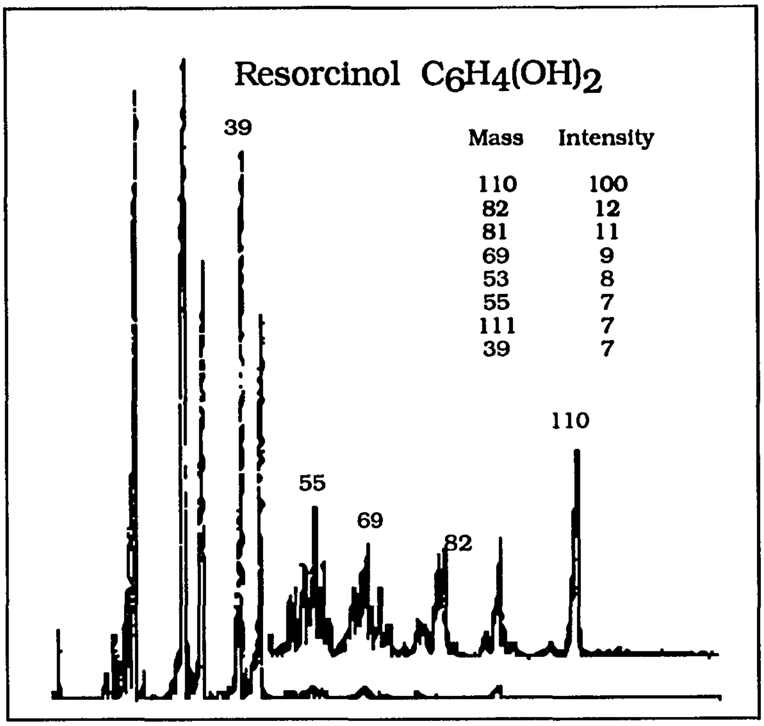

Resorcinol $C_6H_4(OH)_2$

Mass	Intensity
110	100
82	12
81	11
69	9
53	8
55	7
111	7
39	7

Figure 3. Mass spectrum of resorcinol. Electron energy is 70 eV.

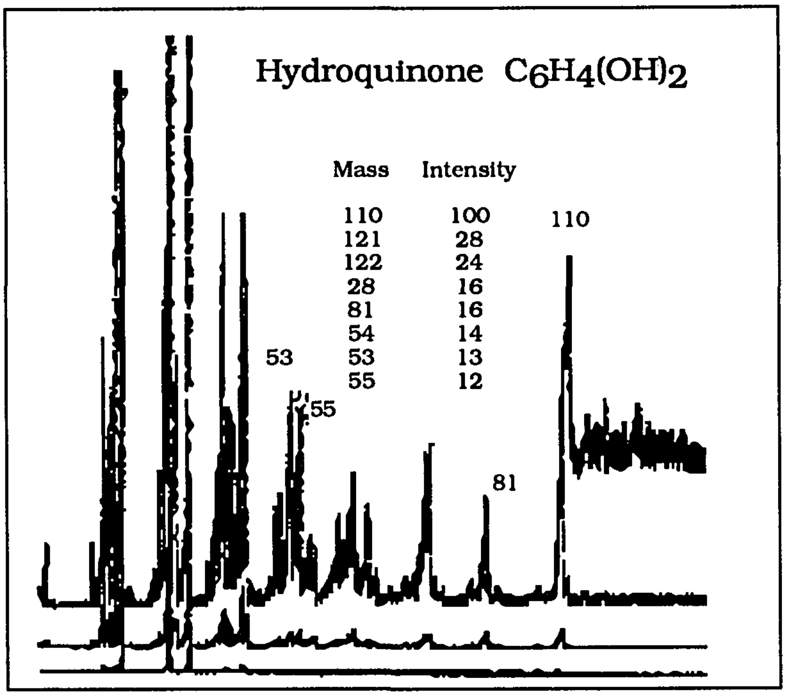

Hydroquinone $C_6H_4(OH)_2$

Mass	Intensity
110	100
121	28
122	24
28	16
81	16
54	14
53	13
55	12

Figure 4. Mass spectrum of hydroquinone. Electron energy is 70 eV.

experiments of the three compounds. For example, a 20 s (0.06 L) exposure is used for the catechol EELS experiments, whereas, 30 s (0.11 L) and 60 s (0.17 L) exposures are used for resorcinol and hydroquinone, respectively. These exposures provide a relatively high coverage in each case.

3. RESULTS

3.1. Catechol

3.1.1. Thermal desorption of catechol The thermal desorption spectra following increasing catechol exposures at 200 K are shown in Figure 5. Trace (a) in Figure 5 represents mass 2, H_2^+, and is monitored to detect hydrogen loss from the catechol. Only one trace is shown since the mass 2 traces are equivalent at all exposures, that is, no H_2 is detectable at any exposure. Traces (b)-(g) are for mass 110, representing the molecular fragment, $C_6H_4(OH)_2^+$, the most intense fragment in the catechol cracking pattern (cf. Figure 2).

Only two desorption features are observed in the mass 110 spectra. At low exposure, one desorption feature at ~220 K is observed. With increasing exposure, two desorption features are observed. The first desorption feature appears at ~220 K, with a second appearing at ~240 K. The intensity of the first feature remains essentially constant, whereas the intensity of the 240 K feature increases with increasing exposure. We attribute the low temperature feature to desorption off the heating wires, and the higher temperature feature is due to the catechol multilayer. Experiments monitoring other characteristic catechol features yield equivalent spectra to catechol (mass 110). That is, no desorption features are observed for masses 53, 55, 63, 81, 92, or 121 other than those due to cracking of the catechol in the mass spectrometer ionizer. Thus, since all other fragments produce identical spectra, these peaks suggest molecular desorption. The desorption energy of the 240 K peak is estimated to be

Figure 5. Thermal desorption spectra of (a) hydrogen and (b) - (g) catechol from Ag(111). The spectra are obtained by monitoring mass 110 ($C_6H_4(OH)_2^+$) following exposure to (b) 0.004, (c) 0.009, (d) 0.013 (e) 0.020, (f) 0.036, and (g) 0.059 L catechol.and by monitoring mass 2 (H_2^+). Spectra equivalent to that of mass 110 are obtained if other, less-intense fragments are monitored. The sample heating rate is 7 K/s.

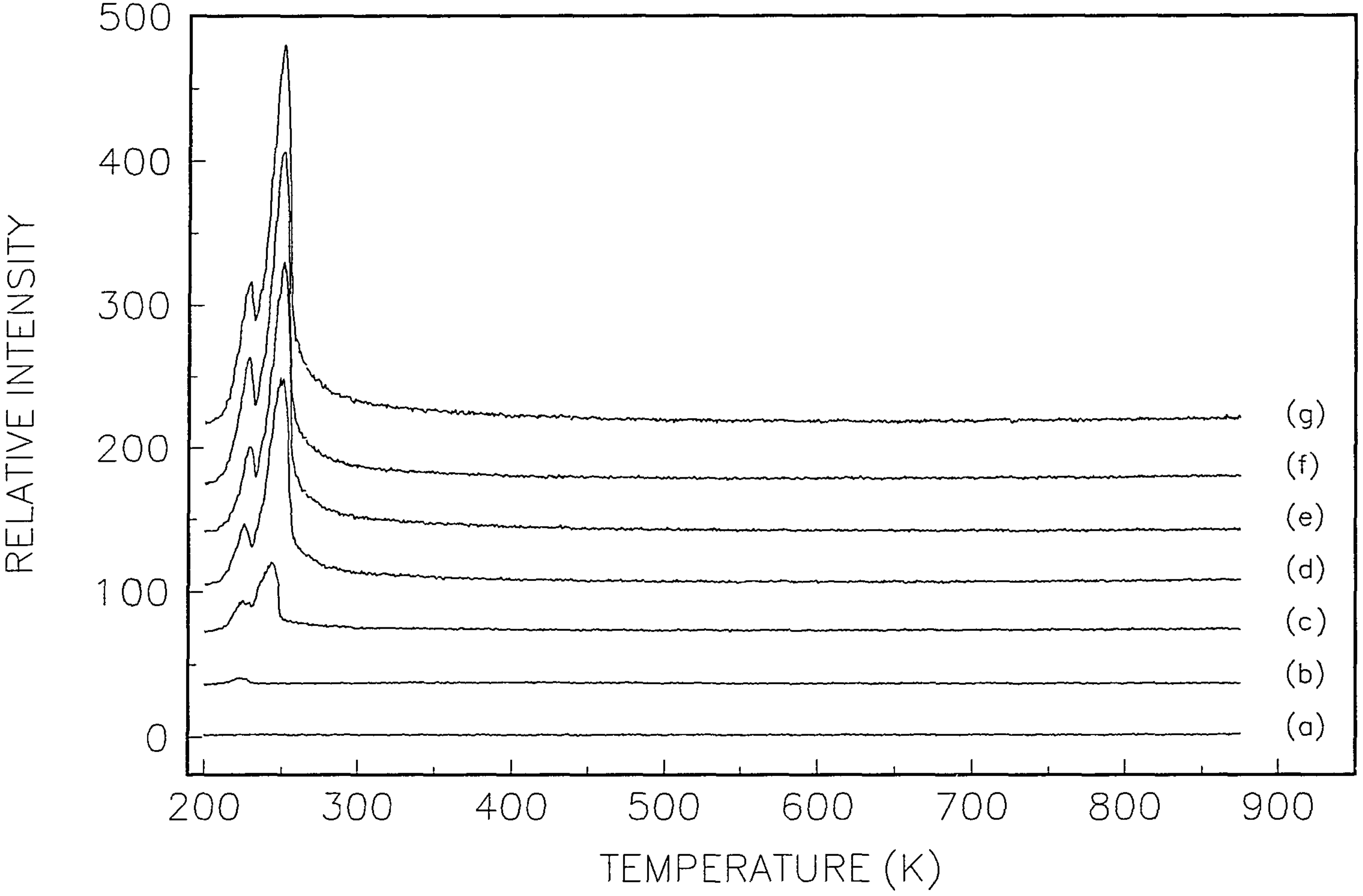
500
400
300
200
100
0
RELATIVE INTENSITY
200
300
400
500
600
700
800
900
TEMPERATURE (K)
(g)
(f)
(e)
(d)
(c)
(b)
(a)

14.32 kcal/mole, assuming first order kinetics and using an approximate equation for desorption energy [10].

3.1.2. Electron energy loss spectroscopy of catechol Figure 6 shows EEL spectra for the deposition of catechol on Ag(111). Curve (a) represents deposition of catechol at 200 K, curve (b) is the spectrum after heating the crystal to 300 K, and curve (c) depicts the spectrum following crystal heating to 700 K. The spectra shown in Figure 6 are representative of several spectra taken in different experiments, and the loss frequencies reported in Table 1 are average values. Thus, the frequencies in Table 1 may not be an exact match to those in Figure 6.

At 200 K, at least six loss features can be identified in the catechol EEL spectra. The loss at 560 cm^{-1} is associated with the skeletal structure of the aromatic ring, and is assigned to a combination of in-plane and out-of-plane skeletal vibrations and radial skeletal stretches. The very strong feature, observed at 755 cm^{-1}, is assigned to a combination of the γ_{CH} deformation mode and radial skeletal stretches of the aromatic ring. This peak indicates aromaticity of the molecule on the surface. The third identifiable peak in curve (a) appears at 1090 cm^{-1}, and is assigned to a combination of the β_{CH} in-plane bending mode and the β_{OH} in-plane bending mode. The peak at 1270 cm^{-1} is assigned to the $\nu_{C\text{-}OH}$ stretch associated with the aromatic ring. The fifth loss feature appears at 1450 cm^{-1}, and is assigned to the ν_{CC} stretching mode. Finally, the peak appearing in the range between 2960 and 3060 cm^{-1} can be assigned to the

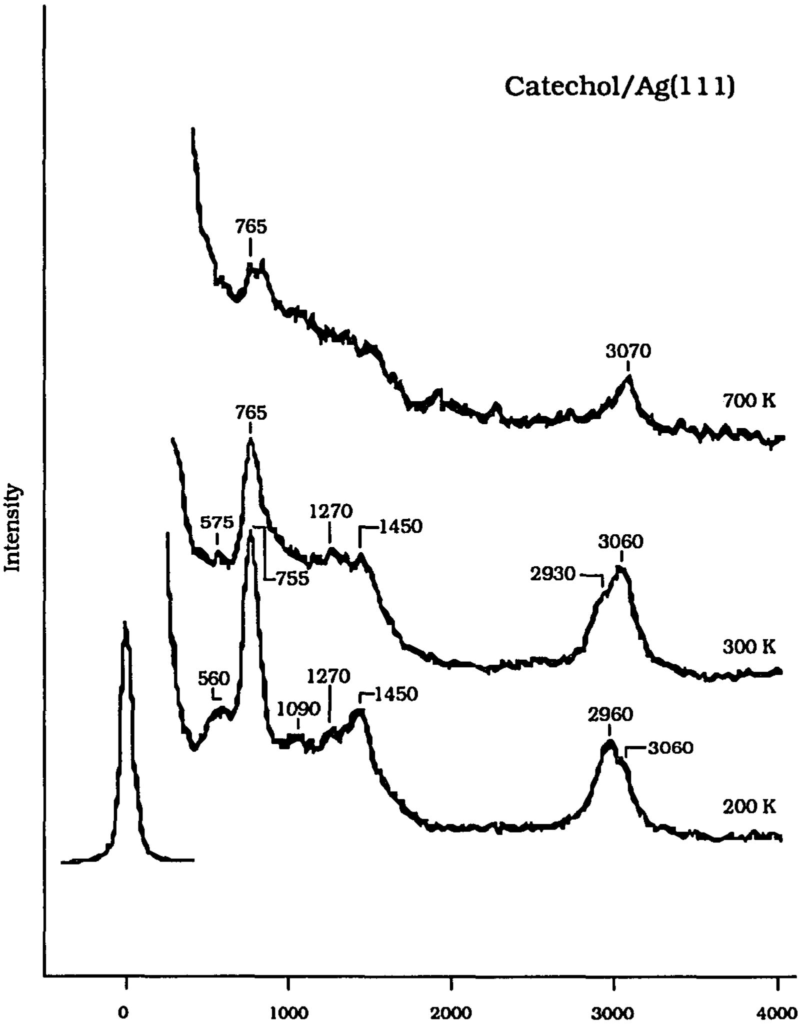

Figure 6. Electron energy-loss spectra of catechol on Ag(1 1 1) at (a) 200 K, (b) 300 K and (c) 700 K. The vibrational mode assignments are summarized in Table 1.

Table 1. Vibrational mode assignments for catechol and "O-H" catechol on Ag(111). Symmetry species for the C_{2v}^* and C_s point groups are presented. The shaded regions indicate symmetry species that represent totally symmetric representations of the respective point groups and obey the metal-surface selection rule.

[a] Reference [19].
[b] Reference [3].
[c] This work.

Mode #	Symmetry Species		IR freq. (cm^{-1})^a	Intensity^a	Catechol/ Pt(111) (electrode)^b	Catechol/ Ag(111)^c	"O-H" Catechol/ Ag(111)^c
	C_{2v}* (⊥)	C_s (//)					
1	a_1	a'	774	m		755 -765	760
2	a_1	a'	---	---			
3	b_2	a"	1284	m			
4	a_2	a"	722	vw			
5	a_2	a"	968	vw			
6a	a_1	a'	548	w		560 - 575	560
6b	b_2	a"	502	s b			
7a	a_1	a'	1275	s	1254	1270	1270
7b	b_2	a"	---	---			
8a	a_1	a'	1608	m	1618		
8b	b_2	a"	1625	s			
9a	a_1	a'	1150	w		1090	1180
9b	b_2	a"	375	m			
10a	b_1	a'	---	---			
10b	a_2	a"	204	m			
11	b_1	a'	745	s		755 - 765	760
12	b_2	a"	847	s			
13	b_2	a"	1243	m			
14	a_1	a'	1355	vs		1450	1470
15	a_1	a'	277	w			
16a	a_2	a"	566	w			
16b	b_1	a'	448	m	508	560 - 575	560
17a	a_2	a"	857	sh			
17b	b_1	a'	938	m	857		
18a	b_2	a"	1090	s			
18b	a_1	a'	1042	s	961	1090	
19a	b_2	a"	1469	s			
19b	a_1	a'	1515	vs	1378	1450	1470
20a	b_2	a"	---	---			
20b	a_1	a'	3045	w	2981	2930/3060	2920/3055
ν_{OH}	a_1	a'	3342	vs b			3435
ν_{OH}	b_2	a"	3460	vs			
β_{OH}	a_1	a'	1162	w			1180
β_{OH}	b_2	a'	1190	s			
γ_{OH}	b_1	a'	630	s			
γ_{OH}	a_2	a"	---	---			

ν_{CH} stretching mode. The low frequency of this peak is indicative of aromatic C-H stretches.

The 300 K catechol EEL spectrum depicted in curve (b) is very similar to that of the 200 K spectrum; however, some changes are apparent. For example, the 560 cm^{-1} loss feature is shifted up to 575 cm^{-1}. Second, the peak at 755 cm^{-1} is shifted up to 765 cm^{-1} and is decreased considerably in intensity. The loss feature at 1090 cm^{-1} is indistinguishable from the background, and the peaks at 1270 and 1450 cm^{-1} are both decreased in intensity. Finally, the last feature in the 300 K spectrum occurs at 3045 cm^{-1} with a low frequency shoulder at 2930 cm^{-1}, corresponding to the ν_{CH} stretching mode.

After heating the crystal to 700 K, the EEL spectrum exhibits only broad features as shown in curve (c). At this temperature, two weak features are identified, one appears at about 760 cm^{-1} and the second at ~3070 cm^{-1}. The 760 cm^{-1} loss feature indicates some aromatic nature of the surface species, as does the low frequency of the second loss feature. Further, the latter loss feature is the ν_{CH} stretch, and most likely represents a hydrocarbon residue, presumably due to decomposition of catechol on the surface.

The author would like to note that in some instances, different catechol EEL spectra are observed and will be referred to as "OH" catechol spectra. In both instances, the deposition conditions are the same. Figure 7 shows "OH" EEL spectra for the deposition of catechol on Ag(111). Curve (a) represents deposition of catechol at 200 K, curve (b) is the spectrum after heating the crystal to 300 K, and curve (c) depicts the

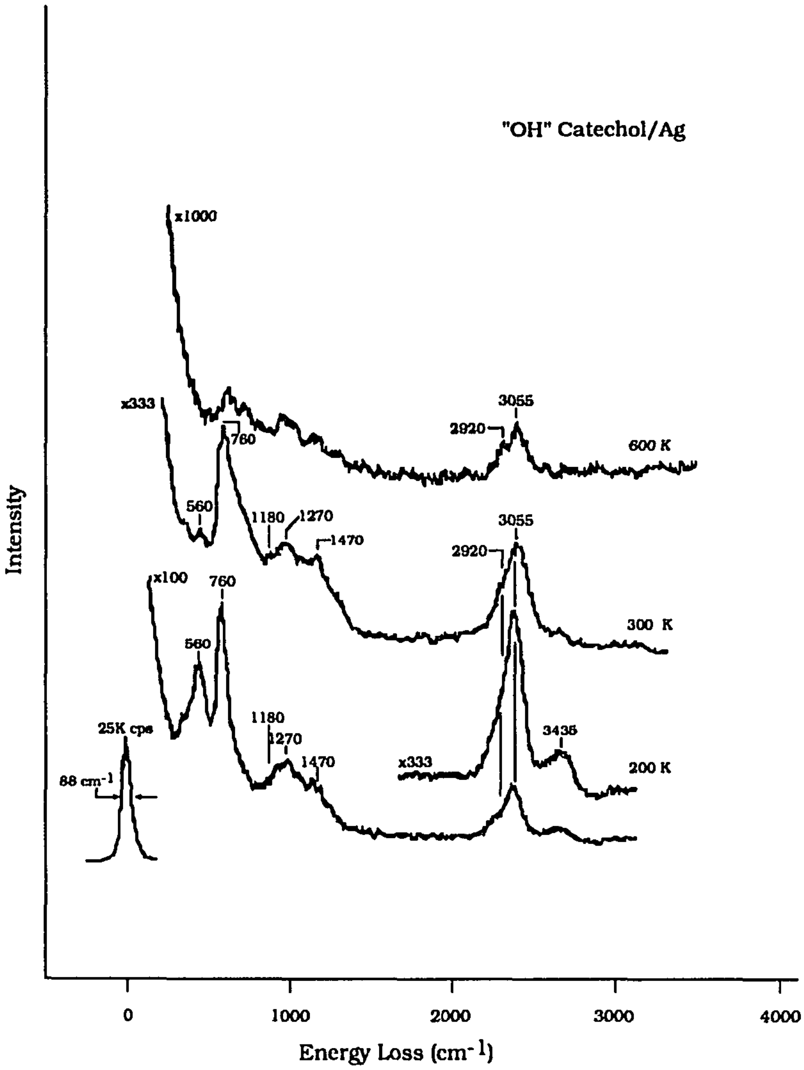

Figure 7. Electron energy loss spectra of "O-H" catechol on Ag(111) at (a) 200 K, (b) 300 K and (c) 800 K. The vibrational mode assignments are summarized in Table 1.

spectrum following crystal heating to 600 K. The frequencies of the loss features observed in the "OH" spectra are also reported in Table 1.

At 200 K, at least seven loss features can be identified in the "OH" catechol EEL spectra. The loss at 560 cm^{-1} is associated with the skeletal structure of the aromatic ring, and is assigned to a combination of in-plane and out-of-plane skeletal vibrations and radial skeletal stretches. The very strong feature observed at 760 cm^{-1} is assigned to a combination of the γ_{CH} deformation mode and radial skeletal stretches of the aromatic ring. This peak indicates aromaticity of the surface molecule. The third identifiable loss feature at this temperature appears as a shoulder at 1180 cm^{-1}, and is assigned to a combination of the β_{CH} in-plane bending mode and the β_{OH} in-plane bending mode. The peak at 1260 cm^{-1} is assigned to the $\nu_{C\text{-}OH}$ stretch associated with the aromatic ring. The fifth loss feature also appears as a shoulder at 1470 cm^{-1}, and is assigned to the ν_{CC} stretching mode. The next peak appears at 3055 cm^{-1} with a low frequency shoulder at 2920 cm^{-1}, and can be assigned to the ν_{CH} stretching mode. The low frequency of this peak is indicative of aromatic C-H stretches. Finally, the loss feature observed at 3435 cm^{-1} is assigned to the ν_{OH} stretching mode.

The main differences between the two catechol EEL spectra at 200 K include the presence of the ν_{OH} stretch and the overall shape of the curve, i.e., the relative intensities of the loss features. In the "OH" spectra, the intensities of the 560 and 1270 cm^{-1} are much greater than corresponding intensities in the previous catechol spectra. By 300 K, the two catechol EEL spectra look essentially identical, that is, all evidence of the ν_{OH} stretch is gone. Because we only obtain these "OH" spectra sporadically, we feel they do not represent the true picture of catechol on Ag(111); however, they do strengthen the mode assignments previously made for catechol.

3.2. Resorcinol

3.2.1. Thermal desorption of resorcinol The thermal desorption spectra following increasing resorcinol exposures at 200 K are shown in Figure 8. Trace (a) in Figure 8 represents mass 2, H_2^+, and is monitored to detect hydrogen loss from resorcinol. Only one exposure is shown of mass 2 since the traces are identical at all higher exposures, that is, there is no detectable desorption of H_2 at any exposure.. Traces (b) - (i) represent mass 110, $C_6H_4(OH)_2^+$, the molecular and most intense fragment in the resorcinol cracking pattern (cf. Figure 3).

Three main desorption features are observed in the mass 110 resorcinol spectra. The first desorption feature appears at ~220 K at low exposure. With increasing exposure, this feature shifts to ~240 K and grows without bound. We suggest that the low temperature feature which evolves into a shoulder of the 240 K desorption peak is due to desorption from the heating wires. The fact that the 240 K feature does not reach a maximum intensity with increasing exposure suggests that it is due to the multilayer state. The second desorption feature appears at ~280 K. The intensity of this feature does not increase substantially with increasing exposure, suggesting that it arises from the first layer of resorcinol molecules on the surface. Finally, a third, very broad, low intensity desorption feature is observed around 380 K. Experiments monitoring other characteristic

Figure 8. Thermal desorption spectra of (a) hydrogen and (b) - (i) resorcinol from Ag(111). The spectra are obtained by monitoring mass 110 ($C_6H_4(OH)_2^+$) following exposure to (b) 0.008, (c) 0.016, (d) 0.024, (e) 0.031, (f) 0.038, (g) 0.045, (h) 0.073, and (i) 0.126 L resorcinol and by monitoring mass 2 (H_2^+). Spectra equivalent to that of mass 110 are obtained if other, less-intense fragments are monitored. The sample heating rate is 7 K/s.

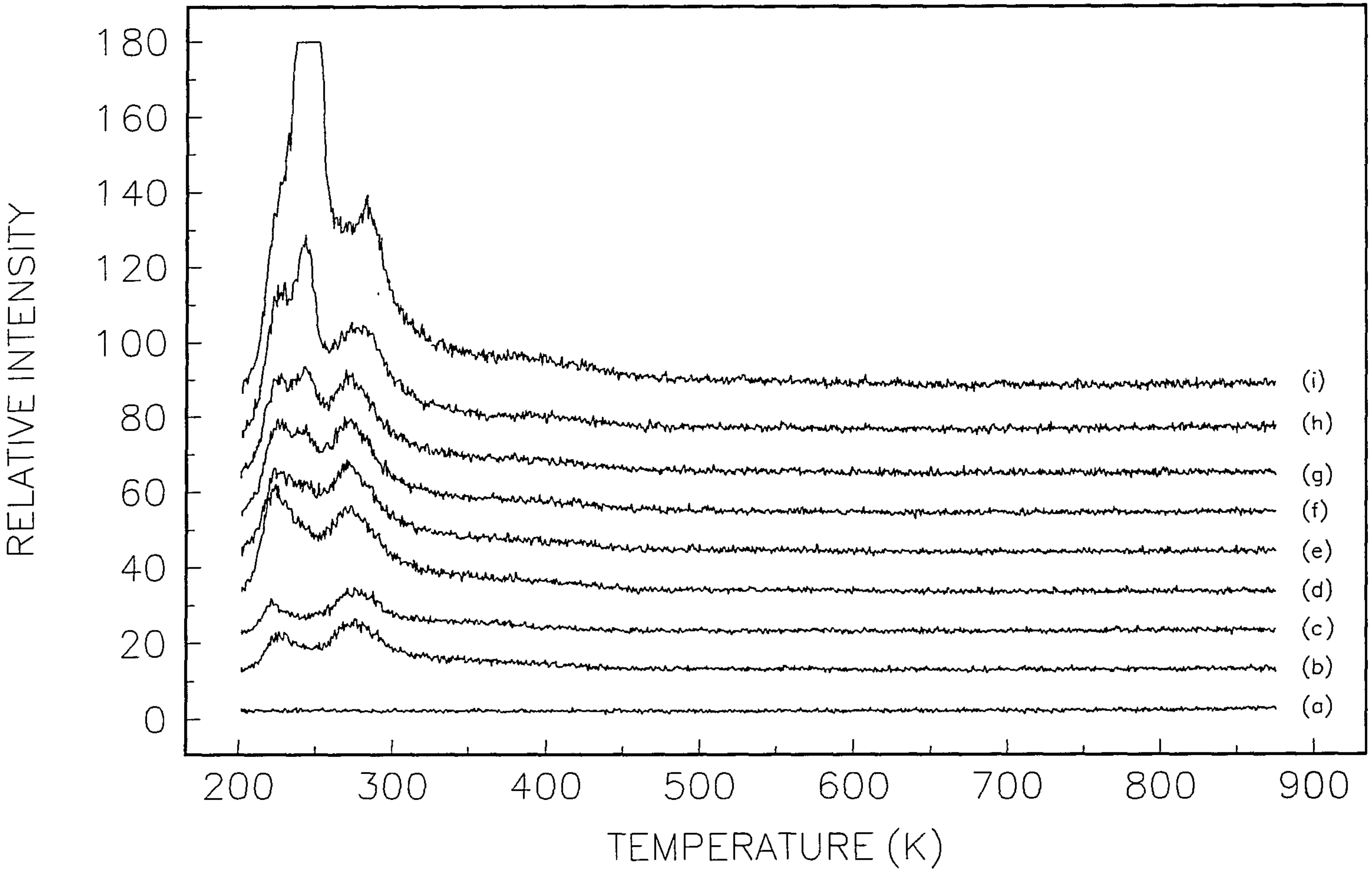
RELATIVE INTENSITY
180
160
140
120
100
80
60
40
20
0
200
300
400
500
600
700
800
900
TEMPERATURE (K)
(i)
(h)
(g)
(f)
(e)
(d)
(c)
(b)
(a)

resorcinol fragments yield equivalent spectra to resorcinol (mass 110). That is, no different desorption features from masses 39, 53, 55, 69, 81, or 111 are observed other than those due to cracking of resorcinol in the mass spectrometer ionizer. Thus, since all other fragments produce identical spectra, these features suggest molecular desorption. The desorption energy of the 280 K peak is estimated to be 16.79 kcal/mole, assuming first order kinetics and using an approximate equation for desorption energy [10].

Experiments monitoring other mass fragments associated with possible reaction products produce only flat, or featureless, desorption spectra. The other mass fragments monitored include masses 16 (O^+), 18 (H_2O^+), 28 (CO^+), 32 (O_2^+), 44 (CO_2^+), and 78 ($C_6H_6^+$). Since no desorption features are observed for these masses, they are disregarded as possible reaction intermediates or products in any surface catalyzed reactions.

3.2.2 Electron energy loss spectroscopy of resorcinol Figure 9 shows EEL spectra for the deposition of resorcinol on Ag(111). Curve (a) represents deposition of resorcinol at 200 K, curve (b) shows the spectrum after heating the crystal to 300 K, and finally, following heating to 800 K, curve (c) is obtained. The spectra shown are representative of several spectra taken at different times, and the loss frequencies reported in Table 2 are average values. Thus, the frequencies in Table 2 may not exactly match those in Figure 9.

Seven loss features are observed in the spectrum obtained following deposition of resorcinol at 200 K. The loss feature at 540 cm^{-1} is associated

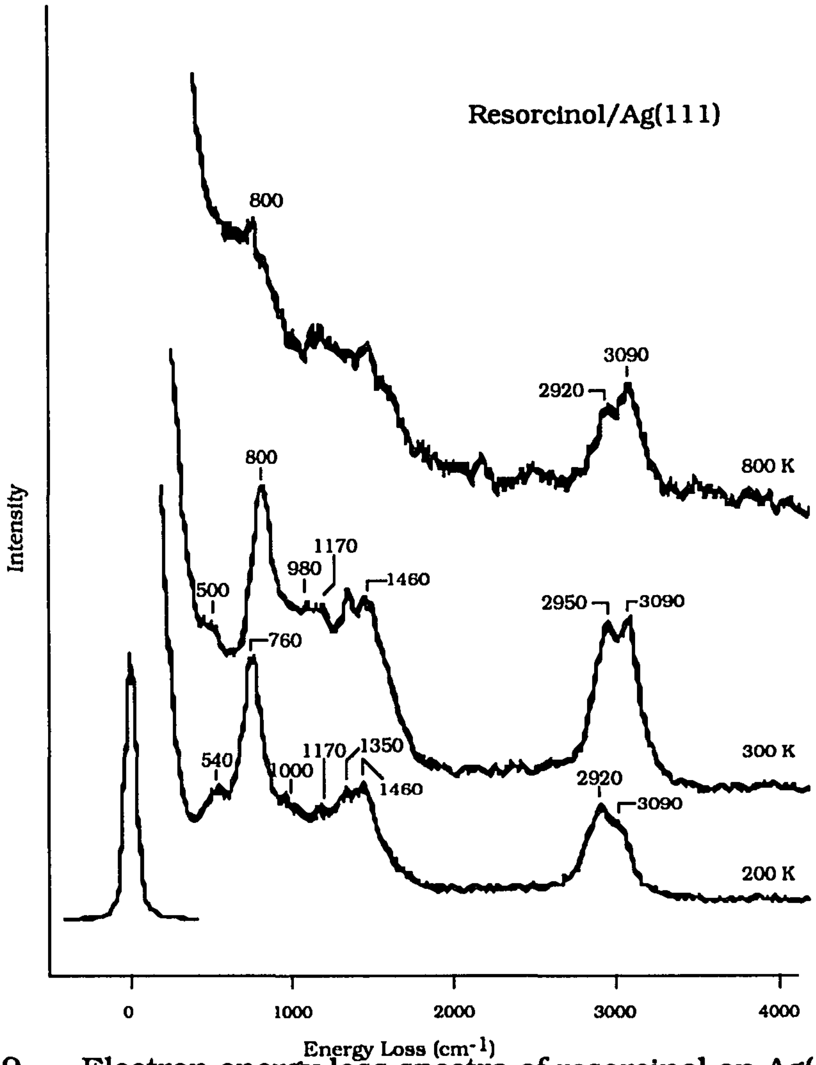

Figure 9. Electron energy loss spectra of resorcinol on Ag(111) at (a) 200 K, (b) 300 K and (c) 700 K. The vibrational mode assignments are given in Table 2.

Table 2. Vibrational mode assignments for resorcinol on Ag(111). Symmetry species for the C_{2v} and C_s point groups are presented. The shaded regions indicate symmetry species that represent totally symmetric representations of the respective point groups and obey the metal-surface selection rule.

[a] Reference [19].

Mode #	Symmetry Species		IR freq. (cm^{-1})^{a}	Intensity^{a}	Ag(111)
	C_{2v} (⊥)	C_s (//)			
1	a_1	a'	748	s	760 - 800
2	a_1	a'	---	---	
3	b_2	a"	1290	sh	
4	a_2	a'	682	s	
5	a_2	a'	931	vw	980 - 1000
6a	a_1	a'	545	s	500 - 540
6b	b_2	a"	531	sh	
7a	a_1	a'	---	---	
7b	b_2	a"	962	vs	
8a	a_1	a'	1606	vs	
8b	b_2	a"	1620	sh	
9a	a_1	a'	356	vs	
9b	b_2	a"	1162	s	
10a	b_1	a"	256	w	
10b	a_2	a'	---	---	
11	b_2	a'	768	s	760 - 800
12	b_2	a'	1001	w	980 - 1000
13	a_1	a'	1282	vs	1350
14	a_1	a"	1315-1381	s	1350
15	a_2	a"	495	w	
16a	b_1	a"	---	---	
16b	a_2	a'	458	m	
17a	a_2	a"	868	m	
17b	b_1	a'	855	m	760 - 800
18a	b_2	a"	1075	vw	
18b	a_1	a"	1120	sh	1170
19a	b_2	a'	1460	m	
19b	a_1	a"	1490	sh	1460
20a	b_2	a'	3045	vw	2920/3090
20b	a_1	a"	3072	vw	2920/3090
ν_{OH}	a_1	a'	2400-3700	vs	2920/3090
ν_{OH}	b_2	a"	2400-3700	vs	
β_{OH}	a_1	a'	1170	vs	1170
β_{OH}	b_2	a"	1225	vs	
γ_{OH}	a_2	a"	612	w	
γ_{OH}	b_1	a'	612	w	

with the skeletal structure of the aromatic ring, and is assigned to a combination of in-plane and out-of-plane radial skeletal bends. The very strong feature observed at 760 cm^{-1} is assigned to a combination of the out-of-plane γ_{CH} deformation mode and radial skeletal stretches of the aromatic ring. This peak indicates aromaticity of the surface species. The third visible loss feature, at 1000 cm^{-1}, is assigned to a combination of radial skeletal vibrations and out-of-plane γ_{CH} deformations. The next loss feature occurs at 1170 cm^{-1}, and is assigned to an in-plane β_{CH} bending mode and an in-plane β_{OH} bending mode. The loss feature at 1350 cm^{-1} is attributed, in part, to the $\nu_{C\text{-}OH}$ stretch and also to ν_{CC} stretches. The sixth identifiable loss feature appears at 1460 cm^{-1}, and is assigned to the ν_{CC} stretching mode. Finally, the peak appearing at 2920 cm^{-1} can be assigned to the ν_{CH} stretching mode. The low frequency of this feature is characteristic of aromatic C-H stretches.

The 300 K resorcinol EEL spectrum, shown in Figure 9, is very similar to the 200 K spectrum; however, some changes are apparent. For example, the loss feature at 540 cm^{-1} is shifted down in frequency to 500 cm^{-1}. Second, the peak at 760 cm^{-1} is shifted to 800 cm^{-1} and is decreased in intensity. The third loss feature is also shifted down slightly in frequency to 980 cm^{-1}. The peak at 1170 cm^{-1} is still present, as is the peak at 1460 cm^{-1}. Finally, the last feature appears as a doublet at 2950 and 3090 cm^{-1}, corresponding to the ν_{CH} stretching mode.

After heating the crystal to 800 K, the EEL spectrum is almost featureless as shown in curve (c). At this temperature, two loss features can still be identified, one at 800 cm^{-1} and another broad loss in the range between 2900 and 3070 cm^{-1}. The 800 cm^{-1} loss feature indicates some aromatic nature of the surface species, as does the low frequency of the second loss feature. Further, the peak appearing in the range between 2900 and 3070 cm^{-1} may also be due to hydrocarbon residue, presumably due to decomposition of resorcinol on the surface.

3.3. Hydroquinone

3.3.1. Thermal desorption of hydroquinone The thermal desorption spectra of increasing hydroquinone exposures at 200 K are shown in Figure 10. Traces of three mass fragments are shown in Figure 10. Trace (a) in Figure 10 represents mass 2, H_2^+, and is monitored to detect any hydrogen loss from the hydroquinone. Only one exposure of mass 2 is shown since traces at other exposures are equivalent to the one shown. Thus, no evolution of H_2^+ is ever detected. Traces (b) - (d) represent mass 110, $C_6H_4(OH)_2^+$, the molecular and most intense fragment in the hydroquinone cracking pattern (cf. Figure 4), at increasing exposures.

Three main desorption features are observed in the hydroquinone desorption spectra. The first feature appears at ~250 K and grows without bound as exposures increase. This behavior suggests a multilayer state. The second desorption feature appears at ~290 K, and is attributed to the first layer of hydroquinone molecules on the surface. Finally, a third, low intensity desorption feature is observed around 380 K. Experiments monitoring other characteristic hydroquinone fragments yield equivalent spectra to resorcinol (mass 110). That is, no different desorption features from masses 54, 55, or 81 are observed other than those due to cracking of

Figure 10. Thermal desorption spectra of (a) hydrogen and (b) - (d) hydroquinone from Ag(111). The spectra are obtained by monitoring mass 110 ($C_6H_4(OH)_2^+$) following exposure to (b) 0.105, (c) 0.158, and (d) 0.198 L hydroquinone and by monitoring mass 2 (H_2^+). Spectra equivalent to that of mass 110 are obtained if other, less-intense fragments are monitored. The sample heating rate is 7 K/s.

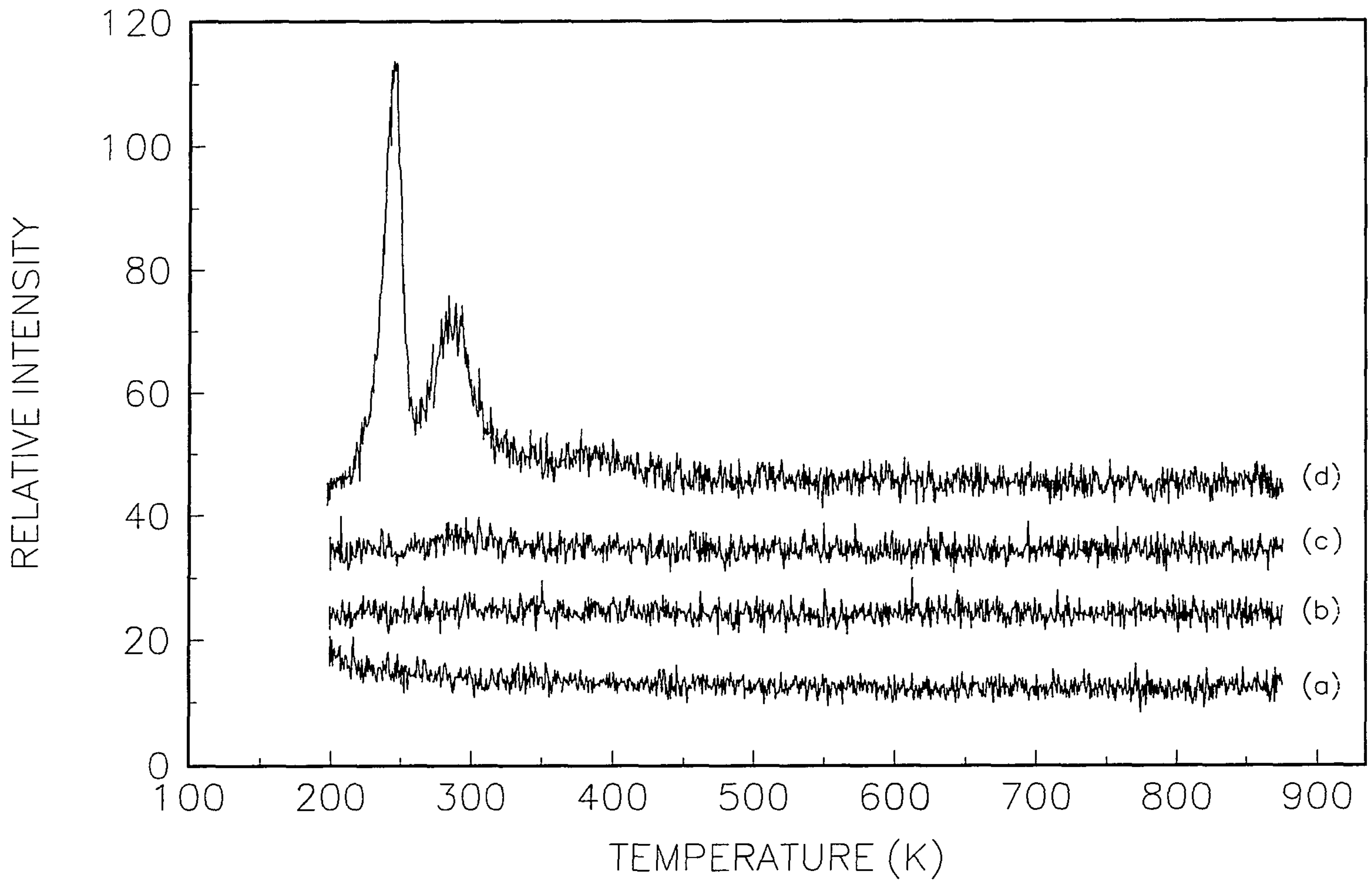
RELATIVE INTENSITY
0
20
40
60
80
100
120
100
200
300
400
500
600
700
800
900
TEMPERATURE (K)
(d)
(c)
(b)
(a)

hydroquinone in the mass spectrometer ionizer. Thus, since all other fragments produce identical spectra, these three features suggest molecular desorption. The desorption energy of the 290 K peak is estimated to be 17.41 kcal/mole, assuming first order kinetics and using an approximate equation for desorption energy [10].

Experiments monitoring other mass fragments associated with possible reaction products produce only flat, or featureless, desorption spectra. The other mass fragments monitored include masses 78 ($C_6H_6^+$), 94 ($C_6H_5OH^+$) and 66 ($C_4H_2O^+$). Mass 94 represents molecular phenol, mass 78 is benzene, and mass 66 represents a fragment characteristic in the phenol fragmentation pattern. At all exposures, one desorption feature is observed at ~240 K for mass 66; however, a desorption feature at this temperature is observed in the mass 78 and 94 spectra only at high exposures. The origin of the mass 66 feature may be due to decomposition of hydroquinone to an ethylinic ketone species ($C_4H_2O^+$) and an ethylinic alcoholic species ($C_2H_2OH^+$); of mass 44. However, mass 44 is not monitored in this study, so no reaction pathway can be proposed at this time. It is possible that masses 94 and 78 result from decomposition of the hydroquinone to phenol in the mass spectrometer ionizer. Note that these features appear at the same temperature as the multilayer state.

3.3.2. Electron energy loss spectroscopy of hydroquinone The EEL spectra for the deposition of hydroquinone on Ag(111) is shown in Figure 11. Curve (a) represents deposition of hydroquinone at 200 K, curve (b) shows the EEL spectrum after heating the crystal to 300 K, and curve (c) is the spectrum following crystal heating to 900 K. The spectra

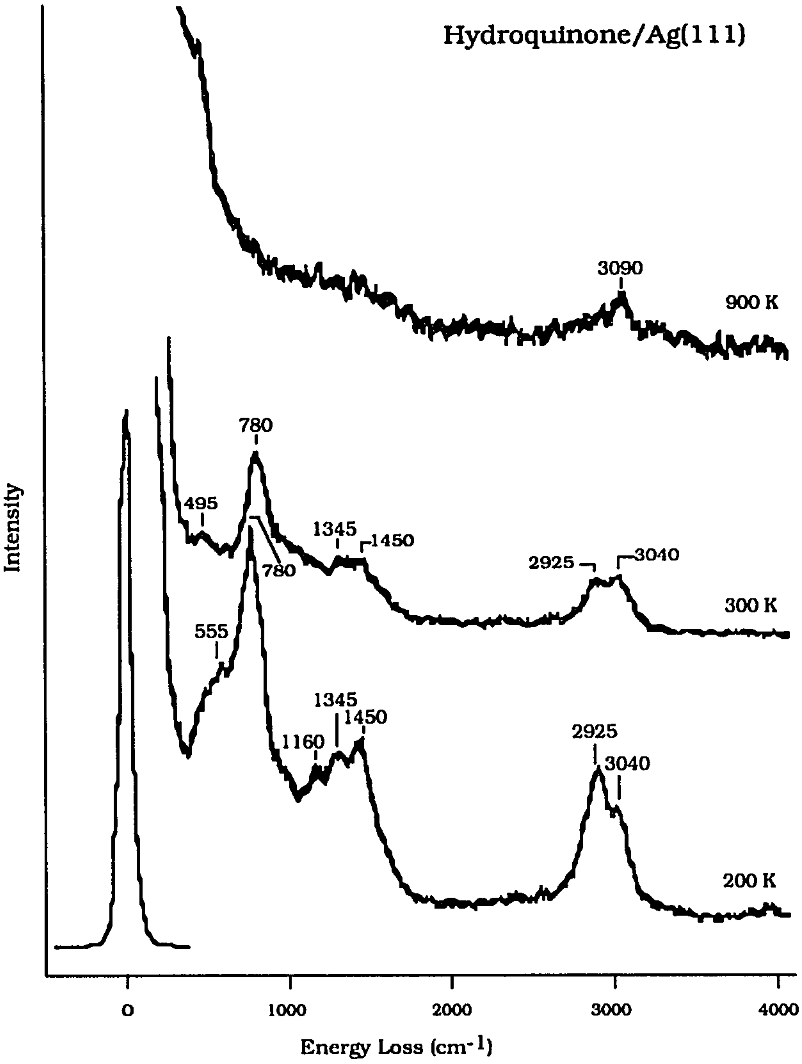

Figure 11. Electron energy loss spectra of hydroquinone on Ag(111) at (a) 200 K, (b) 300 K and (c) 900 K. The vibrational mode assignments are summarized in Table 3.

shown are representative of several spectra taken at different times, and the loss frequencies reported in Table 3 are average values. Thus, the frequencies in Table 3 may not exactly match those of Figure 11.

At 200 K, five loss features can be identified in the hydroquinone EEL spectrum. The first feature is weak and occurs at 555 cm^{-1}. This loss is associated with the skeletal structure of the aromatic ring, and is assigned to a combination of in-plane and out-of-plane skeletal bends. The second feature is a very strong loss at 780 cm^{-1}, and is assigned to a combination of the γ_{CH} deformation mode and radial skeletal stretches of the aromatic ring. Again, this peak indicates aromaticity of the surface species. The third and fourth identifiable peaks appear at 1345 and 1450 cm^{-1}, respectively, and are assigned to ν_{CC} stretching modes. The last loss feature in curve (a) appears at 2925 cm^{-1} with a high frequency shoulder at 3040 cm^{-1}, and is assigned to the ν_{CH} stretching mode. Again, the low frequency of this peak is indicative of aromatic C-H stretches.

Very few changes are observed in the hydroquinone EEL spectrum at 300 K. The frequency of the first loss feature is shifted down from 555 cm^{-1} to 495 cm^{-1}. The second loss feature remains at about the same frequency, but its intensity is considerably decreased. A new peak appears at 1160 cm^{-1}, and is attributed to a combination of in-plane β_{CH} bends and in-plane β_{OH} bends. The 1345 cm^{-1} and 1450 cm^{-1} features decrease in intensity; however, their frequencies remain about the same. Finally, the high frequency shoulder on the 2925 cm^{-1} peak has grown into a defined peak at 3040 cm^{-1}, and is now more intense than the 2925 cm^{-1} peak.

Table 3. Vibrational mode assignments for hydroquinone on Ag(111). Symmetry species for the C_{2v}^* and C_s point groups are presented. The shaded regions indicate symmetry species that represent totally symmetric representations of the respective point groups and obey the metal-surface selection rule.

[a] Reference [19].
[b] Reference [8].

Mode #	Symmetry Species		IR freq. (cm^{-1})^a	Intensity^a	Pt(111) (electrode)^b	Ag(111)
	C_{2v}* (⊥)	C_s (//)				
1	a_1	a'	850	s		780
2	a_1	a'	---	---		
3	b_2	a"	---	---		
4	a_2	a"	700	w		
5	a_2	a"	918	vw		
6a	a_1	a'	471	sh		495 - 555
6b	b_2	a"	648	w		
7a	a_1	a'	1257	s	1247	
7b	b_2	a"	---	---		
8a	a_1	a'	1616	s	1611	
8b	b_2	a"	---	---		
9a	a_1	a'	1157	m		1160
9b	b_2	a"	390	w		
10a	b_1	a'	832	w		
10b	a_2	a"	371	m		
11	b_1	a'	211	w		
12	b_2	a"	758	m	785	780
13	b_2	a"	1216	s		
14	a_1	a'	1350	m		1345
15	a_1	a'	322	vw		
16a	a_2	a"	412	m		
16b	b_1	a'	517	s	506	495 - 555
17a	a_2	a"	937	vw		
17b	b_1	a'	826	vs		790
18a	b_2	a"	1007	m	905	
18b	a_1	a'	1103	m		1160
19a	b_2	a"	1510	vs		
19b	a_1	a'	1470	m	1496	1450
20a	b_2	a"	---	---		
20b	a_1	a'	3026	m	2979	2925/3090
ν	a_1/b_2	a'/a"	3394	vs vb		
β	a_1/b_2	a'	1205	vs b		
γ	a_2/b_1	a'/a"	605	s		

Following crystal heating to 900 K, the hydroquinone EEL spectrum is essentially featureless. Only one weak loss feature can be identified at about 3090 cm^{-1}, corresponding to ν_{CH} stretches. This peak is most likely due to hydrocarbon residue resulting from decomposition of hydroquinone on the surface.

4. DISCUSSION

4.1. Catechol

This investigation of catechol allows the identification and structural characterization of the molecule on the Ag(111) surface. As discussed in detail below, TDS results suggest molecular adsorption (i.e., retention of aromaticity), as do features in the EEL spectra below 700 K. Further, although the TDS and EELS results suggest no dehydrogenation (i.e., no O-H bond scission) upon catechol adsorption, the possibility cannot be completely disregarded. Finally, the EELS data suggest that the orientation of the adsorbed species is temperature dependent, and a model is proposed.

4.1.1. Retention of aromaticity of catechol Catechol adsorbs associatively on the Ag(111) surface. This associative adsorption is evidenced in the molecular desorption observed in the TDS results. Molecular desorption is inferred since mass 110 represents the molecular fragment ($C_6H_4(OH)_2^+$) and no different desorption features arising from other fragments are observed.

The product of this molecular adsorption is catechol, as shown in the catechol EEL spectra (cf. Figure 6). Table 1 summarizes the observed losses in the catechol EEL spectra, as well as their vibrational assignments. Vibrational assignments for catechol determined in a previous study [3] are also included in Table 1 for comparison. All catechol vibrational mode assignments in this study are made by comparison to the normal modes of the benzene molecule as described in the Introduction of this dissertation. Thus, the catechol assignments are numbered according to the benzene convention. The fact that all of the observed loss features correspond to normal modes of the benzene molecule is a strong indication of the aromatic nature of the adsorbed species.

As with phenol, at least two of the catechol loss features observed in the EEL spectra, at both 200 and 300 K, indicate aromatic character in the adsorbed species. The very strong feature centered around 760 cm^{-1} is associated with the ν_1 and ν_{11} vibrations of the benzene ring. The ν_1 mode represents radial skeletal vibrations, or "ring breathing" modes, whereas the ν_{11} mode originates from γ_{CH} out-of-plane bending vibrations. Further, losses in this frequency range can indicate the type of substitution in benzene derivatives, and in this case, indicates an *ortho*-di-substituted benzene [11]. Thus, the intensity and frequency of this loss strongly suggests an aromatic surface species at these temperatures.

Further indication of the aromatic nature of the adsorbed molecule is evidenced in the ν_{CH} stretch centered between 2960 and 3060 cm^{-1} in both the 200 and 300 K spectra. This feature is assigned to the ν_{20b} vibrational mode corresponding to the benzene ring. Generally, ν_{CH} stretches for aromatic and ethylinic C-H bonds appear in the range between 3030 and 3080 cm^{-1}, whereas aliphatic and acetylinic C-H stretches occur at much lower or higher frequencies, i.e., 2840 to 3000 cm^{-1} for aliphatic ν_{CH} stretches and 3250 to 3340 cm^{-1} for acetylinic ν_{CH} stretches [11]. In addition, it is common to observe multiple peaks in this region [11] as is evidenced in the shoulders observed on this peak in Figure 6. Therefore, due to the frequency of the observed loss feature, the surface species is indeed aromatic at these temperatures.

Following crystal heating to 700 K, most of the vibrational features disappear from the EEL spectrum. The most identifiable feature at 3070 cm^{-1} is assigned to a ν_{CH} stretch. As described above, the frequency of this stretch indicates either ethylinic or aromatic ν_{CH} stretches [11]. In some spectra, there is evidence of another loss feature at 750 cm^{-1}, indicating aromaticity of the adsorbed species; however, in most instances only the high frequency loss feature is observed. Thus, we suggest that the feature at 3070 cm^{-1} is primarily ethylinic in nature, but could also arise from a combination of aromatic and ethylinic C-H stretches. Other studies of ethylene [12-14], propylene [15], and acetylene di-σ-bonded to the surface [16] support the ethylinic ν_{CH} mode assignment. Therefore, at this temperature, it is most likely that the 3070 cm^{-1} loss originates from an ethylinic hydrocarbon residue on the surface.

4.1.2. Dehydrogenation of catechol When considering the adsorption of catechol, there exists a possibility of O-H bond scission, or dehydrogenation upon adsorption. As with phenol, the TDS and EELS results can be interpreted to suggest that no dehydrogenation occurs upon catechol adsorption.

The TDS results suggest no O-H bond scission. If dehydrogenation does occur, followed by desorption of H_2, we would expect the mass 2 TDS trace to show at least one desorption feature. As shown in Figure 5, no H_2 evolution is observed up to 800 K. However, the absence of a separate desorption feature for mass 2 does not unambiguously eliminate the possibility of dehydrogenation. Perhaps the O-H bond does break upon adsorption, but the hydrogen remains coadsorbed on the surface and recombines with the dehydrogenated species to desorb as catechol. Isotopic exchange experiments are necessary to prove this dehydrogenation-recombination reaction pathway.

Dehydrogenation, or O-H bond scission, upon adsorption is suggested in previous EELS studies of catechol on Pt(111) electrode surfaces; however, no evidence is presented for the evolution of H^+ [3]. Previous studies of phenol on Mo(110) [17] and Ni(110) [18] suggest O-H bond scission and the formation of surface phenoxide, evidenced by the desorption of dihydrogen gas. No analogous thermal desorption studies of catechol are found in the literature.

At all temperatures, the EEL spectra evidence an absence of the ν_{OH} stretch. In gas phase IR data, this vibrational mode appears in the range between 3342 and 3460 cm^{-1} [19]. An absence of this feature suggests three possibilities: (a) O-H bond scission, (b) hydrogen bonding at the surface, or (c) parallel orientation of the O-H bond axis. Note that only the first possibility favors dehydrogenation of the hydroxyl groups. If dehydrogenation does occur upon adsorption, we would not expect to observe the ν_{OH} stretch in the EEL spectra [8]. Figure 12a shows how the dehydrogenated surface catechol species might appear on Ag(111). As noted in the TDS experiments, no conclusive evidence for O-H bond scission is observed; however, the absence of the ν_{OH} stretch may further support a dehydrogenation-recombination reaction pathway, followed by desorption.

A second possible dehydrogenation pathway may be a dimerization or polymerization reaction between catechol molecules, forming ether linkages. If an aromatic ether linkage were present in the EEL spectra, we would

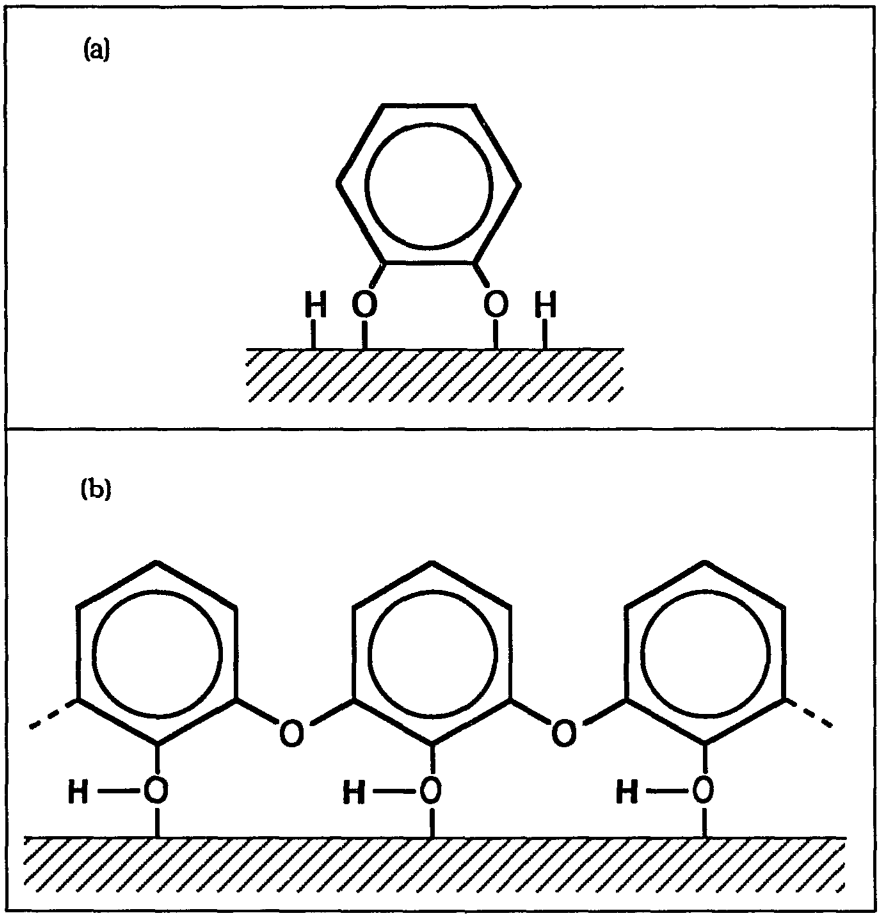

Figure 12. (a) Diagram of the dehydrogenated catechol species on the surface.
(b) Diagram of the polymerized catechol species on the surface.

expect to observe a loss feature between 1200 and 1275 cm^{-1} [11]. We do, in fact, observe a loss in this frequency range; however, as stated earlier, this feature can also be assigned to the $\nu_{C\text{-}OH}$ stretch. Figure 12b shows what dimerized or polymerized catechol species might look like on the Ag(111) surface.

Hydrogen bonding between adjacent catechol molecules may also explain the absence of ν_{OH} stretches in the EEL spectra. Hydrogen bonded O-H bonds have small scattering cross sections in EELS and/or IR spectroscopy [20, 21], thus, one might expect to observe only a very weak ν_{OH} stretch, if one at all. Evidence of hydrogen bonding between adsorbed phenol molecules has been observed previously [22, 23]. Figure 13 shows how hydrogen bonded catechol molecules might appear on the Ag(111) surface. Thus, the absence of a ν_{OH} stretch may be an indication of hydrogen bonding between adsorbed catechol species, and not of O-H bond scission.

Finally, in accordance with the metal-surface selection rule, the orientation of the O-H bond axis may render the ν_{OH} stretch virtually invisible in the EEL spectra. In this scenario, either the entire catechol molecule is oriented parallel to the surface, or at least the O-H bond axis is parallel to the surface. Figure 14 shows these two possible orientations. Briefly, the metal-surface selection rule states that only vibrations with a component of the dipole moment change perpendicular to the surface are observed in EEL spectra. In both of the above scenarios, the O-H bond is parallel to the surface; therefore, the ν_{OH} stretch should not be observed in

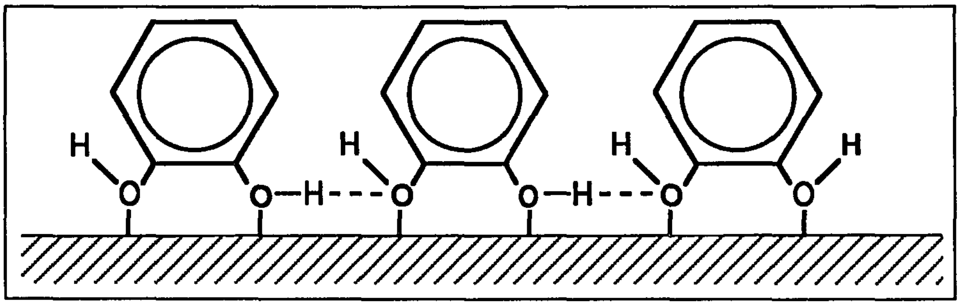

Figure 13. Diagram of hydrogen bonded catechol on Ag(111).

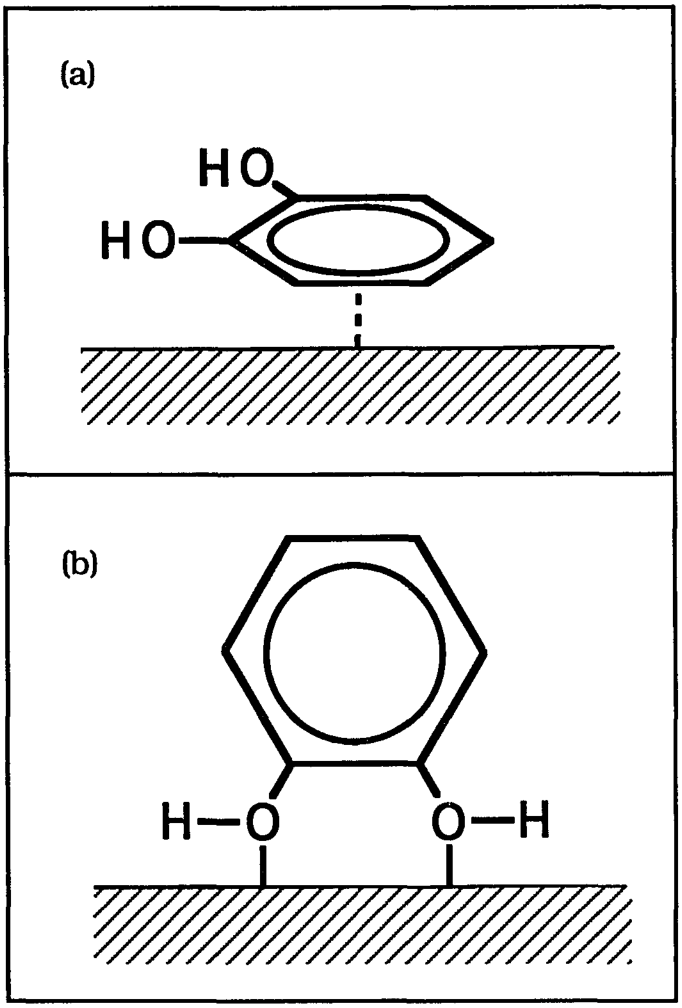

Figure 14. Two possible orientations for catechol in which the O-H bond axis lies parallel to the surface.

the EEL spectra. Thus, the absence of the ν_{OH} stretch may suggest molecular orientation and not indicate dehydrogenation.

The above arguments suggest several possible explanations for the absence of the ν_{OH} stretch in the catechol EEL spectra. Only one explanation favors dehydrogenation, and the latter two suggest no O-H bond scission upon adsorption. Instead, the orientation of the adsorbed species, along with hydrogen bonding between adsorbed molecules, would cause the ν_{OH} stretch to be essentially absent from the EEL spectra. At this point, however, dehydrogenation cannot be completely ruled out, isotopic exchange experiments would be necessary for complete proof of O-H bond scission.

4.1.3. Ring orientation models of catechol High resolution EELS experiments are done, in part, to determine the orientation of the molecule on the surface. When considering which orientation catechol adopts on the surface, we evaluate the data using two different approaches. In the first approach, we assume that only one chemical species exists on the surface at all times and temperatures. Further, we assume that this species adopts a single, well-defined molecular orientation, i.e., either perpendicular, inclined, or parallel. In the second approach, we consider the temperature dependence of the adsorbed species orientation, allowing more than one chemical species to exist on the surface. Table 1 shows the normal mode assignments for catechol EELS loss features.

In the "one species" approach, we categorize the assigned vibrational modes into specific point group symmetries according to possible orientations. The orientation described by the point group to which most of the vibrational modes belong represents the preferred orientation of the surface species. Table 1 shows the specific symmetry species and point groups which describe the catechol EELS loss features. In this case, most of the loss features, at both 200 and 300 K can be assigned to vibrational modes in accordance with the C_{2v}^* symmetry, i.e., the point group representing a perpendicular orientation of the catechol molecule. The assignment of this symmetry group assumes no perturbation from the adsorption site, but does account for the decrease in symmetry due to surface adsorption.

According to the C_{2v}^* point group designation, the peak appearing at 560 cm^{-1} is assigned to the ν_{6a} vibrational mode of benzene. This mode is attributed to the in-plane skeletal bends and belongs to the totally symmetric representation of the C_{2v}^* point group. The very intense feature centered around 760 cm^{-1} is associated with the ν_1 vibration of the benzene ring, representing radial skeletal vibrations, or "ring breathing" modes. The feature centered at 1090 cm^{-1} appears in both the 200 and 300 K spectra, and is assigned to the ν_{9a} vibrational mode of the benzene ring which corresponds to β_{CH}, the out-of-plane bending mode. The peak at 1270 cm^{-1} can be assigned to ν_{7a}, the $\nu_{C\text{-}OH}$ vibrational mode of a substituted benzene. The ν_{CC} stretch at 1450 cm^{-1} is assigned to the both the ν_{14} and the ν_{19b} vibrational modes of benzene. These assignments, ν_1, ν_{6a},ν_{7a}, ν_{9a}, ν_{14}, and ν_{19b} all correspond to totally symmetric representation of *both* the C_{2v}^* and C_s point groups, however those C_s modes do not obey the metal-surface selection rule and therefore, should not be visible in the EEL spectra. Similarly, the ν_{CH} feature centered between 2930 and 3060 cm^{-1} is assigned to the ν_{20b} vibrational mode of benzene. Again, this mode belongs to the totally symmetric representation of *both* the C_{2v}^* and C_s point groups; however, the representation in the C_s point group does not obey the metal-surface selection rule. Thus, the point group assignments of these features suggest a perpendicular molecular orientation on the Ag surface. Figure 15 shows how a perpendicular orientation might appear on the surface, assuming no O-H bond scission.

Upon closer inspection of Table 1, at least two of catechol EELS loss features may be assigned to vibrational modes that belong *only* to totally symmetric representations of the C_s point group, i.e., the symmetry representing a parallel orientation on the surface. The peak centered at 760 cm^{-1} could also originate from ν_{11}, the γ_{CH} out-of-plane bend, and the peak appearing around 560 cm^{-1} from ν_{16b}, the out-of-plane skeletal bend. Again, both modes, ν_{11} and ν_{16b}, belong only to totally symmetric representations of the C_s point group. However, a completely parallel orientation is ruled out since only two of the six loss features belong solely to totally symmetric representations of the C_s point group *and* obey the metal-surface selection rule. Therefore, the presence and assignment of these two vibrational modes may only suggest some degree of tilting of the catechol away from the surface normal. Figure 16 shows how an inclined orientation of catechol may appear on the surface, assuming no dehydrogenation.

In addition to this study on Ag(111), catechol adsorbed on Pt(111) electrodes from an aqueous solution has been investigated [3, 24]. The previous study suggests a parallel orientation based on EELS and thin-layer

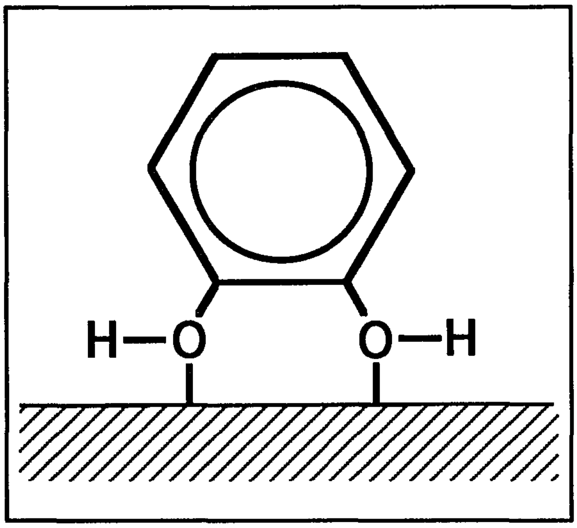

Figure 15. Diagram of catechol in a perpendicular orientation, assuming no dehydrogenation.

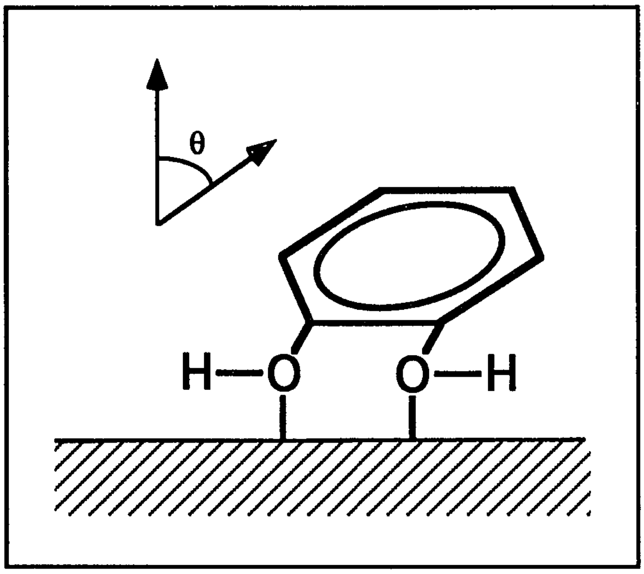

Figure 16. Diagram of catechol in an inclined orientation, at some angle, θ, from the surface normal.

electrochemical results; however does not account for symmetry reduction due to surface adsorption. The catechol vibrational assignments are made by comparison to phenol results of the same author, and are presented in Table 1 as well. Recall, a parallel orientation is synonymous with the C_s point group; however most of the mode assignments in the previous catechol study belong to the C_{2v}^* point group, i.e., suggesting a perpendicular orientation. Thus, careful attention must be paid to the molecule's reduction in molecular symmetry due to surface adsorption.

The second possible interpretation suggests that more than one species exists on the surface as a function of temperature. In this model, catechol adopts an inclined orientation on the surface upon adsorption at 200 K. An inclined orientation is inferred based on the arguments presented in the previous paragraphs. In this model, at 200 K, the features at 560 and 755 cm^{-1} are assigned solely to ν_{16b} and ν_{11}, respectively, based on their frequencies and intensities. Both vibrational modes, ν_{16b} and ν_{11}, belong to totally symmetric representations *only* of the C_s point group, i.e., representing a parallel orientation. However, since most of the other features in the EEL spectrum belong to the C_{2v}^* point group, i.e., representing a perpendicular orientation, we suggest that the molecule is inclined by some angle, θ, to the surface at this temperature.

As the crystal temperature is increased, however, changes in the EEL spectrum signal changes in the molecular orientation of the adsorbed species. The TDS results indicate molecular desorption at 240 K; however, the EEL spectrum suggests that catechol is still present on the surface at 300 K (cf. Figure 5). Further, by 300 K, the frequency of the 755 cm^{-1} loss shifts up to 765 cm^{-1}, as its intensity decreases significantly. This loss feature is now assigned solely to the ν_1 vibrational mode of benzene, the radial skeletal or "ring breathing" mode. An upward frequency shift is also observed in the 560 cm^{-1} feature as it appears at 575 cm^{-1} at 300 K. This feature is now assigned solely to ν_{6a}, the in-plane skeletal bends of benzene. As described earlier, ν_1 and ν_{6a} belong to the totally symmetric representations of *both* the C_{2v}* and Cs point groups; however, only the C_{2v}* symmetry species obeys the metal-surface selection rule. Further, the C_{2v}* point group represents a perpendicular orientation on the surface. Thus, by 300 K, the EEL spectrum suggests the catechol molecules assume the perpendicular orientation shown in Figure 15.

By 700 K, only one distinguishable feature remains in the catechol EEL spectrum, appearing at 3070 cm^{-1}. As previously discussed, this peak is assigned to a ν_{CH} stretch, most likely due to a hydrocarbon residue on the surface. However, in some spectra at this temperature, the peak at 760 cm^{-1} is still visible, thus it is possible that the residual species has some aromatic character. Thus, by 700 K, either the catechol has molecularly desorbed, decomposed to only hydrocarbon fragments, or possibly dimerized or polymerized to a small extent, leaving some aromatic fragments on the surface.

The temperature-dependent model just described suggests molecular desorption and irreversible decomposition of catechol on Ag(111). At 240 K, some catechol molecularly desorbs and some remains intact on the surface. By 700 K, the remaining catechol has decomposed, and for the most part, only a hydrocarbon residue is evident on the surface, although we can only postulate as to the residue's composition. Figure 17 depicts this temperature dependent model, assuming no O-H bond scission. This model suggests that two species may coexist on the surface at one time. The two species may be two di-hydroxide species, each adsorbed at different sites, or the two species may be a di-hydroxide species along with molecular catechol. However, our data cannot unequivocally distinguish between a di-hydroxide and a molecular catechol species. A similar reaction pathway is observed for phenol on Mo(110) [25] and is suggested for phenol on Ag(111) as described in Part 1 of this dissertation. Further, the temperature dependent orientation change from inclined to perpendicular is similar to the change observed for pyridine on Ni(100) [26], i.e., parallel to edgewise, or η_2. Thus, although we cannot unambiguously distinguish between molecular and di-hydroxide species, our data does suggest a change in orientation upon heating.

4.2. Resorcinol

This study of resorcinol allows the surface characterization of the molecule on the Ag(111) surface. As with catechol, the resorcinol TDS results suggest molecular desorption (i.e., retention of aromaticity), as do features in the EEL spectra below 800 K. Further, the TDS and EELS results suggest no dehydrogenation (i.e., no O-H bond scission) upon resorcinol adsorption; however the possibility of dehydrogenation cannot be completely ruled out. Finally, the EELS measurements suggest a temperature dependence of the adsorbed species on the surface, and a model is proposed.

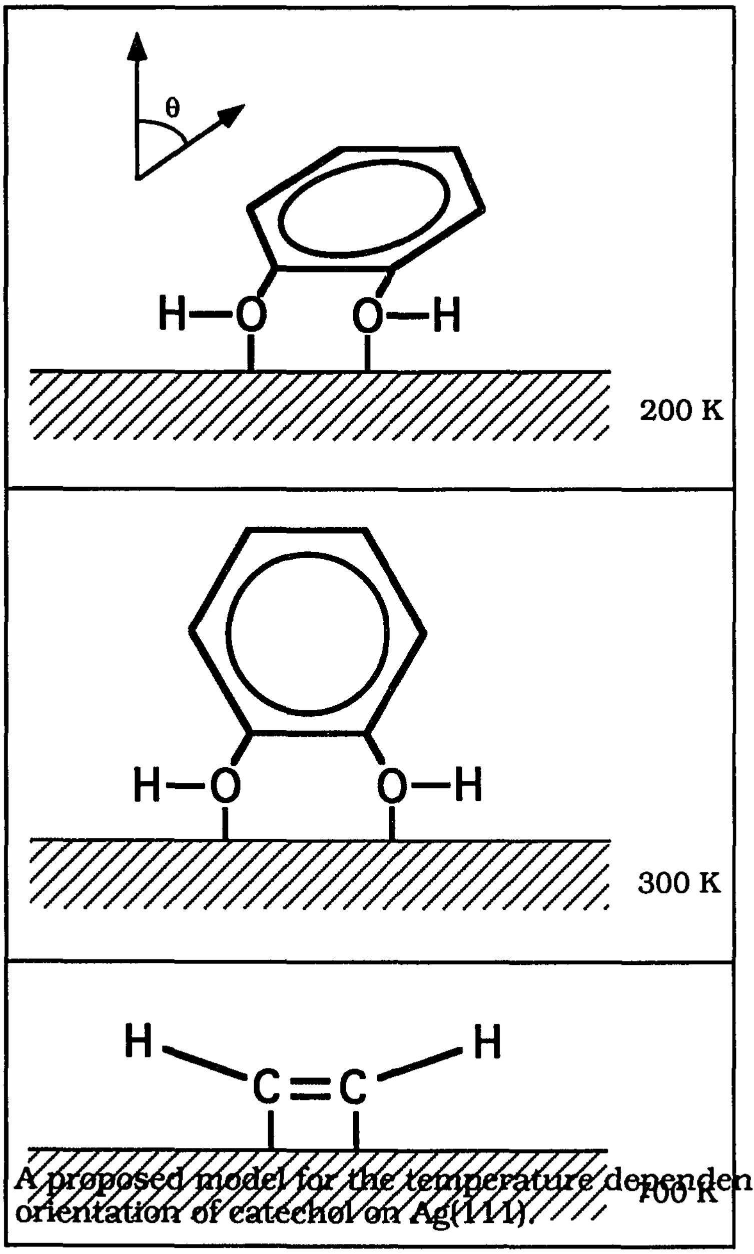

Figure 17. A proposed model for the temperature dependence of the orientation of catechol on Ag(111).

4.2.1. Retention of aromaticity Molecular desorption of resorcinol is observed in the TDS experiments; thus, resorcinol adsorbs associatively on the Ag(111) surface at 200 K. Molecular desorption is inferred since mass 110 represents the molecular fragment ($C_6H_4(OH)_2^+$) and no other desorption features arising from other characteristic fragments are observed.

As shown by the EEL spectra in Figure 9, the product of this molecular desorption is resorcinol. Table 2 summarizes the observed losses in the EEL spectra, as well as their assignments. All resorcinol vibrational mode assignments are made by comparison to the normal modes of the benzene molecule as described in the General Introduction of this dissertation. Thus, the resorcinol assignments are numbered according to the benzene vibrational mode convention. The fact that all of the observed loss features correspond to normal modes of the benzene molecule is strong evidence of the aromatic nature of the adsorbed species.

As with catechol, features in the resorcinol EEL spectra, at both 200 and 300 K, indicate aromatic character in the adsorbed species. Again, a very intense feature is observed centered between 760 and 800 cm^{-1}, and is associated with the ν_1 and ν_{11} vibrational modes of benzene. The ν_1 mode originates from radial skeletal or "ring breathing" modes, and ν_{11} originates from γ_{CH} out-of-plane bending vibrations. Generally, losses in this frequency range indicate the type of substitution in benzene derivatives [11]. For a *meta*-di-substituted benzene derivative, this mode normally appears in the range between 750 and 810 cm^{-1} [11]. On average, the frequency observed in the resorcinol EEL spectra is higher than that of the same feature in the catechol spectra, indicating *meta*-di-substitution. Thus, the aromatic nature of the adsorbed species is evidenced in the EEL spectra.

Another indication of the aromatic nature of the adsorbed resorcinol species is evidenced in the frequency of the ν_{CH} stretch centered between 2920 and 3090 cm^{-1} in both the 200 and 300 K EEL spectra. As discussed previously, this feature is assigned to the ν_{20} vibrational mode, and the frequency range of this feature is indicative of aromatic C-H bonds [11]. Therefore, due to the frequency of the observed loss feature, the adsorbed species is indeed aromatic at these temperatures.

Following crystal heating to 800 K, most of the vibrational loss features disappear from the EEL spectrum. The only prominent remaining peak centered in the range between 2920 and 3070 cm^{-1} is assigned to the ν_{CH} stretch. As mentioned previously, the frequency of this stretch indicates either ethylinic or aromatic ν_{CH} stretches. Other features are sometimes visible in the resorcinol EEL spectrum at this temperature. In particular, a feature at ~800 cm^{-1} is sometimes observed, and again, the presence of this peak indicates aromaticity of the adsorbed species. Although, when observed, the intensity of the 800 cm^{-1} peak is very low, its presence suggests that the adsorbed species may retain some aromatic nature up to this temperature. Thus, we suggest that the ν_{CH} stretch originates from a combination of ethylinic and aromatic species on the surface.

4.2.2. Dehydrogenation of resorcinol When considering the adsorption of resorcinol on Ag(111), the possibility of O-H bond scission, or dehydrogenation, exists. If O-H bond scission occurs upon adsorption, what happens to the hydrogen, and how is the resulting dehydrogenated species bound to the surface? At first glance, the TDS and EELS results suggest dehydrogenation; however, the alternate interpretations of the data suggest no O-H bond scission.

The resorcinol TDS results suggest no dehydrogenation. We do not observe any desorption feature in the mass 2, H_2, TDS trace. The absence of a desorption state suggests that no dihydrogen gas is evolved, and thus no dehydrogenation occurs. However, the absence of a mass 2 desorption feature does not unambiguously eliminate the possibility of O-H bond scission. One possible explanation might be that the resorcinol dehydrogenates upon adsorption, but the hydrogen recombines with the dehydrogenated species and then desorbs as molecular resorcinol (mass 110). Isotopic exchange experiments are needed to prove this explanation.

All the resorcinol EEL spectra exhibit an absence of the ν_{OH} stretch. If present, this feature would appear in the range between 2400 and 3700 cm^{-1} [19]. As with catechol adsorption on Ag(111), three possibilities exist for the absence of a ν_{OH} stretch in the resorcinol EEL spectra. These possibilities include: (a) O-H bond scission, (b) hydrogen bonding between the surface species, or (c) parallel orientation of the O-H bond axis in accordance with the metal-surface selection rule. Note that only one explanation favors dehydrogenation The same arguments made for catechol adsorption can be made for resorcinol adsorption.

If O-H bond scission occurs, we would not expect to observe the ν_{OH} stretch in the EEL spectra of resorcinol. Figure 18a shows how the dehydrogenated resorcinol species might appear on the surface. Again, the

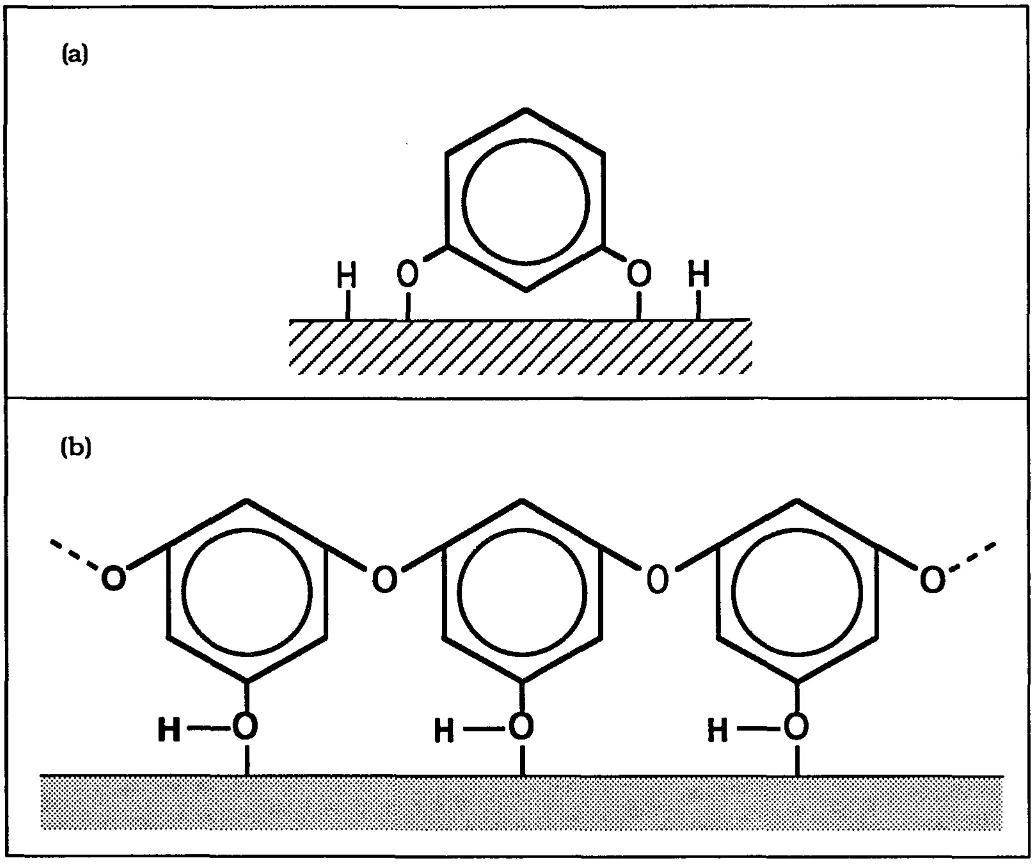

Figure 18. (a) Diagram of the dehydrogenated resorcinol species on the surface.
(b) Diagram of the polymerized resorcinol species on the surface.

TDS results give no conclusive evidence for O-H bond scission; however, the absence of the ν_{OH} stretch does support a dehydrogenation-recombination and desorption explanation. Another possible explanation for an absence of the ν_{OH} stretch is the dimerization or polymerization of the resorcinol species on the surface as shown in Figure 18b. As discussed previously for catechol, if such a reaction occurs, we might expect to observe an aromatic ether stretch in the range between 1200 and 1275 cm^{-1}. However, no such feature is observed in the resorcinol EEL spectra.

Hydrogen bonding between surface species and molecular orientation can also explain the absence of the ν_{OH} stretch in the EEL spectra. If the adsorbed species are hydrogen bonded, we would expect to observe only a very weak ν_{OH} stretch, if any at all [20, 21]. Figure 19 shows how hydrogen bonded resorcinol species may appear on the surface, assuming no O-H bond scission. Finally, according to the metal-surface selection rule, if the O-H bond axis is oriented parallel to the surface, we would not expect to observe a ν_{OH} stretch. This rule suggests that either the O-H bond or the entire resorcinol molecule is oriented parallel to the Ag surface, thus making the ν_{OH} stretch virtually invisible in the EEL spectra. Figure 20 shows these two possible orientations of the resorcinol species on the surface. Thus, the absence of a ν_{OH} stretch does not conclusively indicate O-H bond scission upon adsorption.

The above arguments suggest several possible explanations for the absence of the ν_{OH} stretch in the resorcinol EEL spectra. Only one explanation favors dehydrogenation, and the latter two suggest no O-H bond scission upon adsorption. Instead, the orientation of the adsorbed species,

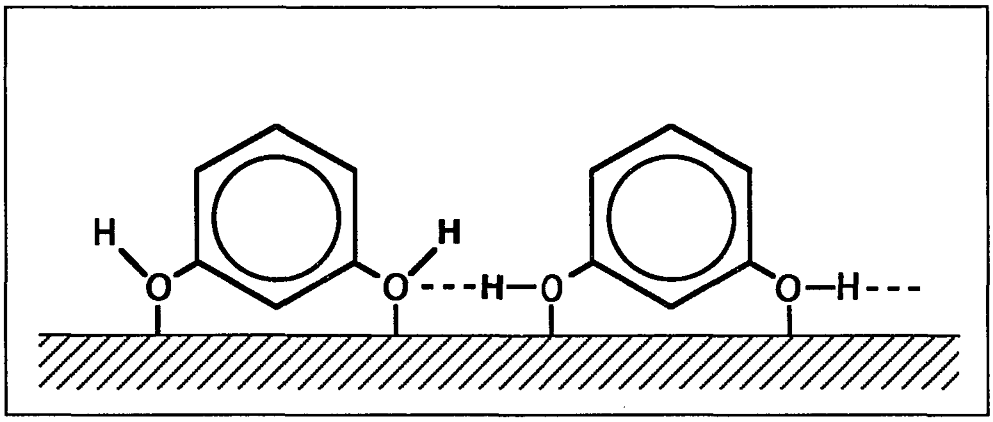

Figure 19. Diagram of hydrogen bonded resorcinol on Ag(111).

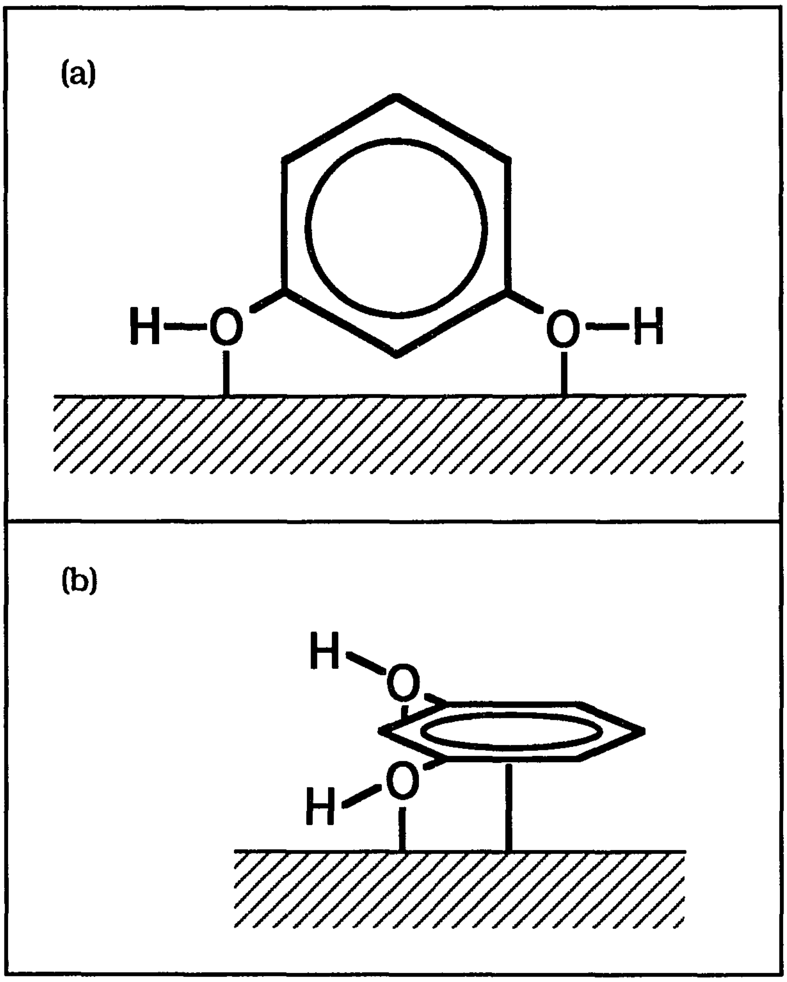

Figure 20. Two possible orientations for resorcinol in which the O-H bond axis lies parallel to the surface.

along with hydrogen bonding between adsorbed molecules, would cause the ν_{OH} stretch to be essentially absent from the EEL spectra. We must note, however, that EELS cannot unambiguously distinguish between molecular resorcinol and a dehydrogenated species, and further, dehydrogenation cannot be completely disregarded until isotopic exchange experiments are performed.

4.2.3. Ring orientation models of resorcinol The TDS spectra of resorcinol on Ag(111) indicate a temperature dependence of the adsorbed surface species. A temperature dependence may suggest a change in orientation of the adsorbed species at different temperatures. Assuming no O-H bond scission, Figure 21 shows a possible temperature dependent model, and the following paragraphs describe the model in detail.

In this model, resorcinol adsorbs perpendicularly on the surface at 200 K. At this temperature, the intense feature appearing 760 cm^{-1} can be assigned to ν_1, ν_{17b}, or a combination of the two vibrational modes. Because of the frequency of this feature at 200 K, we assign it solely to the radial skeletal, or "ring breathing" vibrational mode. Second, the feature appearing at 540 cm^{-1} can also be assigned to two vibrational modes, the ν_{6a} and the ν_{16b} modes. Again, since the frequency of this feature most closely resembles that of ν_{6a}, we shall assign it solely to the radial skeletal, C_3 in-plane bend. These vibrational modes, ν_1 and ν_{6a}, belong to totally symmetric representations of *both* the C_{2v} and C_s point groups; however, only the C_{2v} species obey the metal-surface selection rule. The C_{2v} point group represents a perpendicular orientation on the surface, and since all the other loss features are also assigned to C_{2v} symmetry species, we

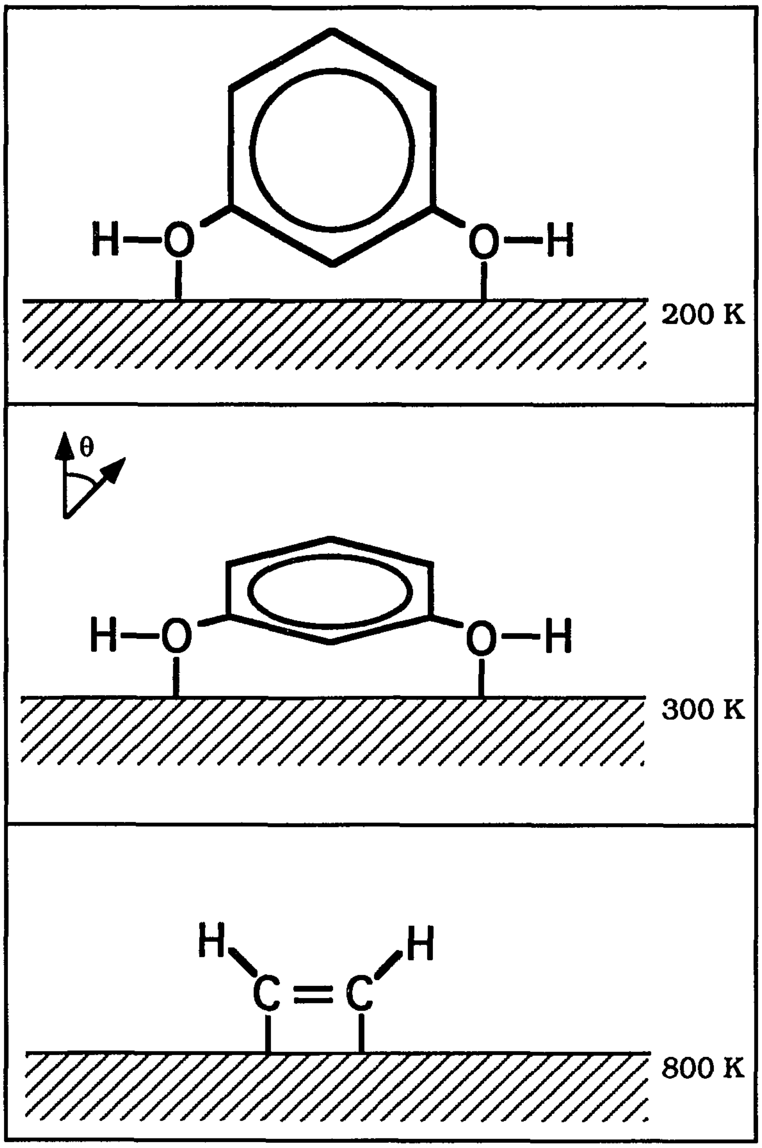

Figure 21. A proposed model for the temperature dependence of the orientation of resorcinol on Ag(111).

conclude that the molecule assumes a perpendicular orientation upon adsorption at 200 K.

As the crystal temperature is increased, changes in the EEL spectrum suggest a different molecular orientation on the surface. The resorcinol TDS results indicate molecular desorption at 280 K and again at ~380 K. The high temperature desorption state suggests that not all the resorcinol is desorbing at 280 K, but rather, some remains intact on the surface to desorb at 380 K (cf. Figure 8). The presence of resorcinol on the surface at 300 K is evidenced in the EEL spectrum at that temperature. By 300 K, the frequency of the 760 cm^{-1} feature shifts up to 800 cm^{-1}. This loss feature is now assigned solely to ν_{17b}, the γ_{CH} out-of-plane bending mode. Also, the frequency of the 540 cm^{-1} feature decreases to 500 cm^{-1} by 300 K, and this features is now assigned solely to ν_{16b}, the C_3 out-of-plane bending mode. Both vibrational modes, ν_{17b} and ν_{16b}, belong to totally symmetric representations of *only* the C_s point group, suggesting a parallel orientation. However, since most of the features in the EEL spectrum at 300 K are still assigned to symmetry species in the C_{2v} point group, we predict the adsorbed species is inclined at some angle, θ, to the surface at 300 K.

By 800 K, only one intense peak is observed in the resorcinol EEL spectrum, appearing at 3070 cm^{-1}. As discussed for catechol, this feature is assigned to the ν_{CH} stretch, presumably due to an ethylinic hydrocarbon residue on the surface. Other weak features occurring at ~800 and ~1350 cm^{-1} are present in some spectra at this temperature, possibly indicating some aromatic nature of the adsorbed species. Thus, by 800 K, the EEL spectra suggest that either the resorcinol has molecularly desorbed or decomposed to hydrocarbon fragments, or possibly aromatic fragments, as depicted in Figure 21.

The temperature dependent model just described suggests molecular desorption, possible reorientation, and irreversible decomposition of resorcinol on Ag(111). At 280 K, some resorcinol desorbs molecularly while some reorients on the surface and then desorbs around 380 K. Any remaining resorcinol decomposes to a hydrocarbon residue by 800 K. We can only postulate what this surface residue may be; however, the frequency of the ν_{CH} stretch present at this temperature suggest an ethylinic hydrocarbon residue. In this study of resorcinol, the high temperature TDS state may represent a dehydrogenated species; however, our data cannot unambiguously distinguish between molecular resorcinol or a di-hydroxide species. However, our data do suggest a reorientation of the adsorbed species upon surface heating.

4.3. Hydroquinone

The TDS and EELS study of hydroquinone on Ag(111) allows the surface characterization of the molecule on the surface. The TDS and EELS results indicate molecular desorption, or the retention of aromaticity, of the adsorbed species at temperatures below 800 K. Further, no dehydrogenation upon adsorption is observed directly by examination of the TDS and EELS results; however, the possibility cannot be completely ruled out on the basis of these experiments only. Finally, the EELS data suggest a temperature dependence of the adsorbed species orientation, and a model is proposed.

4.3.1. Retention of aromaticity The TDS results of hydroquinone on Ag(111) indicate that it desorbs molecularly, suggesting that it adsorbs associatively at 200 K. As with catechol and resorcinol, molecular desorption is inferred since mass 110 represents the molecular fragment ($C_6H_4(OH)_2^+$) and no different desorption features arising from other characteristic fragments are observed. Further, EELS results also indicate that the product of this molecular desorption is hydroquinone. Table 3 summarizes the observed losses in the hydroquinone EEL spectra as well as their assignments. All hydroquinone vibrational mode assignments are made by comparison to the normal modes of benzene as described in the General Introduction of this dissertation. Thus, the hydroquinone assignments are numbered in accordance with the benzene vibrational mode convention. Further, vibrational assignments for hydroquinone deposited from solution onto Pt(111) electrodes [8] are included in Table 3 for comparison. Again, the fact that all the loss features can be assigned to normal modes of benzene strongly suggests aromaticity in the adsorbed species.

As in the catechol and resorcinol EEL spectra, at least two of the features in the hydroquinone spectra, at both 200 and 300 K, indicate aromaticity of the adsorbed species. A feature at 780 cm^{-1} is present, and is assigned to both "ring breathing" and γ_{CH} out-of-plane vibrational modes. Further, its frequency indicates the type of substitution of benzene derivatives. Features in the frequency range between 780 and 860 cm^{-1} suggest *para*-di-substituted benzene derivatives [11]. Further indication of aromaticity of the adsorbed species is evidenced in the ν_{CH} stretch centered between 2930 and 3050 cm^{-1}, which is assigned to the ν_{20b} benzene vibrational mode. The frequency of this stretch suggests aromaticity [11]. Hence, due to the presence of these two loss features and their frequencies, the surface species is indeed aromatic.

After heating to 900 K, only one feature is discernible in the hydroquinone EEL spectrum. This peak appears at ~3050 cm^{-1} and is assigned to a ν_{CH} stretch. As previously described, the frequency of this stretch indicates either ethylinic or aromatic ν_{CH} stretches [11]. Since there is no further evidence of aromaticity in the surface species, due to the absence of the 780 cm^{-1} feature, we assume this stretch to be ethylinic in nature. This mode assignment is consistent with previous studies of ethylene [12-14], propylene [15], and di-σ-bonded acetylene [16]. Thus, we conclude that this loss originates from an ethylinic hydrocarbon residue remaining on the surface.

4.3.2. Dehydrogenation of hyroquinone As with catechol and resorcinol, the question of dehydrogenation arises when considering the adsorption of hydroquinone on Ag(111). The same arguments can be made concerning dehydrogenation as in the previous cases of catechol and resorcinol, and these arguments are substantiated with TDS and EELS results.

Thermal desorption experiments of hydroquinone suggest no dehydrogenation, or O-H bond scission, upon adsorption at 200 K. There is no evidence of H_2 evolution as no desorption feature is observed in the mass 2 TDS trace (cf. Figure 10). The absence of this desorption feature does not conclusively exclude dehydrogenation, however, as O-H bond scission could occur, followed by recombination with the dehydrogenated species and desorption. If this dehydrogenation-recombination reaction occurs, we would not detect any H_2 evolution in the TDS spectrum; however, isotopic exchange experiments are necessary to prove this reaction pathway.

We again observe an absence of the ν_{OH} stretch in all the hydroquinone EEL spectra. Recall, this stretch should appear around 3394 cm^{-1}, if present [19]. As observed in our previous studies of phenol, catechol, and resorcinol on Ag(111), the absence of this feature can be described by at least three different explanations. The possible explanations include (a) O-H bond scission, (b) hydrogen bonding, and (c) adsorption geometry. Further, the same arguments made in the previous cases can be applied to hydroquinone adsorption.

If dehydrogenation occurs, we would not expect to observe the ν_{OH} stretch in the hydroquinone EEL spectra. Figure 22a shows what the adsorbed, dehydrogenated, hydroquinone species may look like on the surface. As we do not observe the ν_{OH} feature, we may initially conclude that dehydrogenation does occur. However, the TDS results give no conclusive evidence for O-H bond scission. Further, the absence of the ν_{OH} stretch supports the dehydrogenation-recombination desorption explanation proposed earlier. Another possible explanation for an absence of the ν_{OH} stretch is dehydrogenation followed by dimerization or polymerization of the hydroquinone species on the surface. In the hydroquinone case, we might envision polymerization via oxidation to a quinone species [27, 28] as depicted in Figure 22b. If this occurs, we would expect to see a ketone ν_{CO}

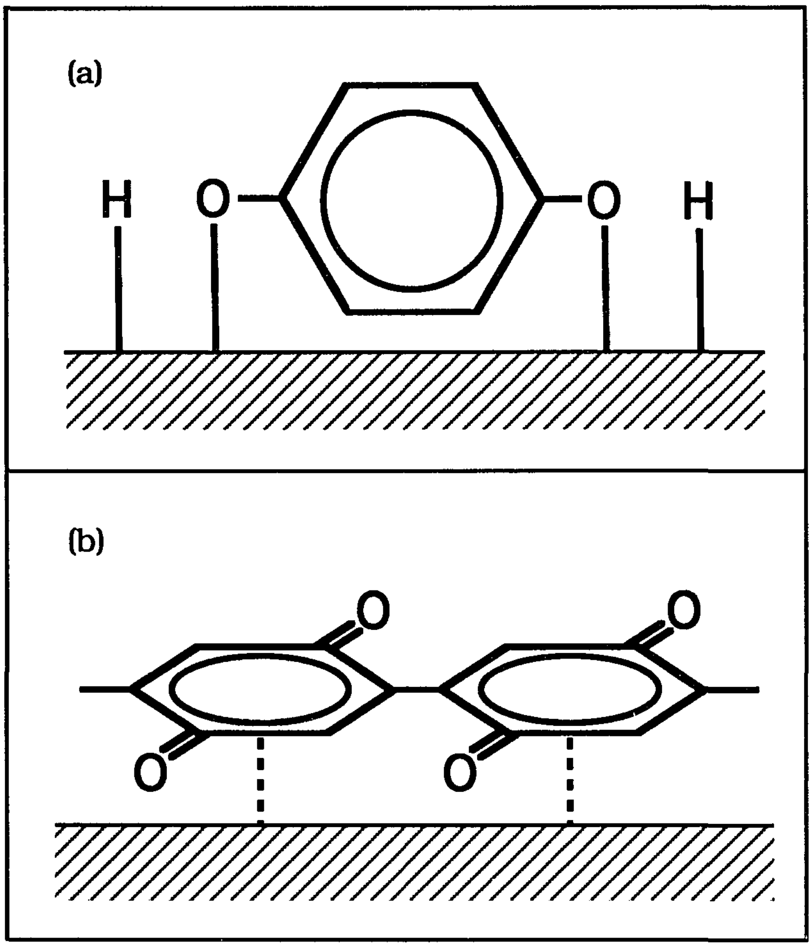

Figure 22. (a) Diagram of the dehydrogenated hydroquinone species on the surface.
(b) Diagram of the polymerized hydroquinone species on the surface.

stretch in the range between 1666 and 1685 cm^{-1} [29]. However, no such feature is observed in the hydroquinone EEL spectra.

Hydrogen bonding between surface species and adsorption geometry also provide explanations for the absence of the ν_{OH} stretch in the hydroquinone EEL spectra. Recall that if hydrogen bonds do exist, we would expect to observe only a very weak ν_{OH} stretch, if any at all [20, 21]. Figure 23 shows how hydrogen bonded hydroquinone species may appear on the surface. Finally, if the O-H bond axis is oriented parallel to the surface, we would not expect to observe the ν_{OH} stretch, in accordance with the metal-surface selection rule. This rule suggests that a parallel orientation of the O-H bond axis on the Ag surface would make the ν_{OH} stretch virtually invisible in the EEL spectra. Figure 24 shows these two possible orientations of the hydroquinone species on the surface. Thus, hydrogen bonding between adsorbed species and/or molecular orientation suggest that the absence of the ν_{OH} stretch does not conclusively indicate O-H bond scission upon adsorption.

The above arguments suggest several possible explanations for the absence of the ν_{OH} stretch in the hydroquinone EEL spectra. Only one explanation favors dehydrogenation, and the latter two suggest no O-H bond scission upon adsorption. Instead, the orientation of the adsorbed species, along with hydrogen bonding between adsorbed molecules, would cause the ν_{OH} stretch to be essentially absent from the EEL spectra. We must note, however, that a dehydrogenation reaction cannot be completely excluded until isotopic exchange experiments are performed.

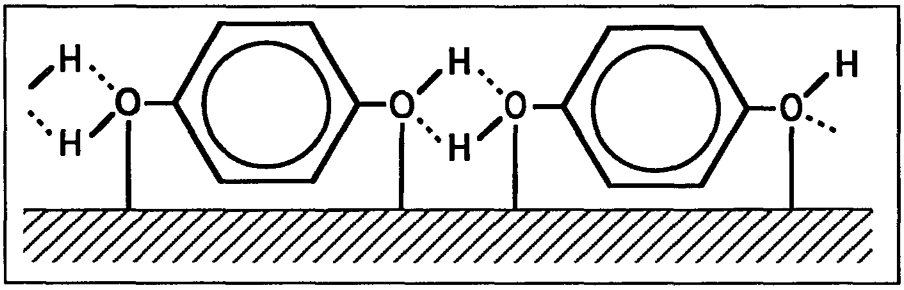

Figure 23. Diagram of hydrogen bonded hydroquinone on Ag(111).

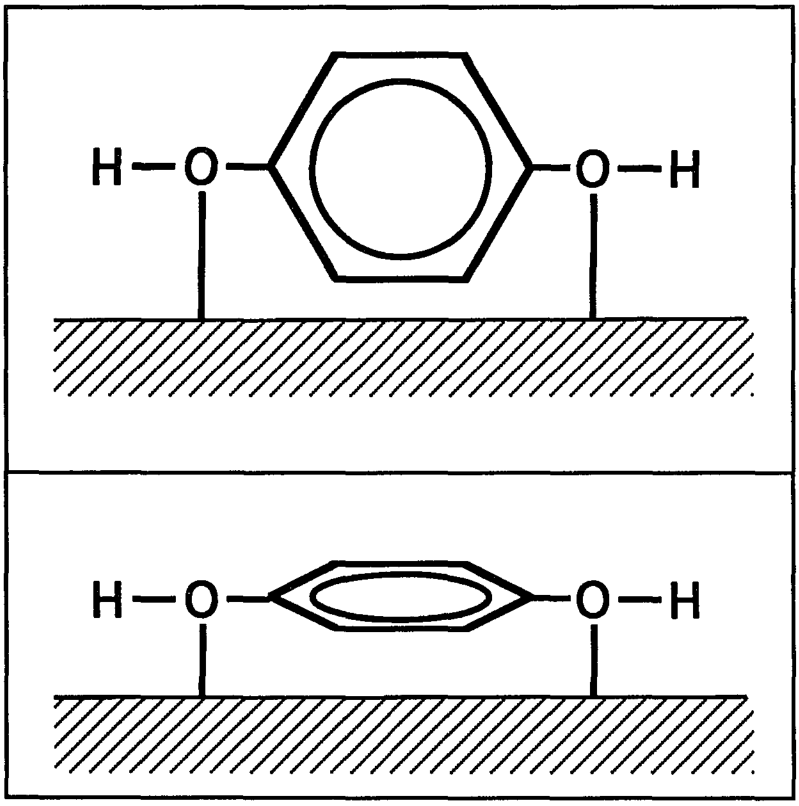

Figure 24. Two possible orientations for hydroquinone in which the O-H bond axis lies parallel to the surface.

4.3.3. Ring orientation models of hydroquinone The TDS results of hydroquinone deposited on Ag(111) at 200 K suggest a temperature dependence of the chemical species adsorbed on the surface. The temperature dependence of the molecular species may suggest different molecular orientations at different temperatures. Assuming no O-H bond scission, Figure 25 shows what this temperature dependent model may look like.

In this model, hydroquinone assumes a perpendicular orientation on the surface upon adsorption at 200 K. At this temperature, the feature appearing at 555 cm^{-1} is visible as only a low frequency shoulder on the more intense 780 cm^{-1} peak. This shoulder is assigned to either the ν_{6a} or ν_{16b} vibrational modes, or a combination of both. In the gas-phase IR data, the ν_{6a} mode appears as a shoulder, and the ν_{16b} modes as a strong feature [19]. Since the intensity of this peak is low and it only appears as a shoulder at 200 K, we shall assign it solely to the ν_{6a}, C_3 in-plane bend. The symmetry species ν_{6a} belongs to the totally symmetric representation of *both* the C_{2v}^* and C_s point groups; however, only the C_{2v}^* symmetry species obey the surface selection rule. The C_{2v}^* point group represents a perpendicular orientation on the surface. Since most of the other loss features belong to totally symmetric representations of the C_{2v}^* point group, we predict a perpendicular orientation at 200 K.

As the crystal temperature increases, changes in the vibrational spectrum signal changes in the molecular orientation. Although the TDS results indicate molecular desorption at 280 K, hydroquinone is still present on the surface as evidenced in the EEL spectrum at 300 K. Further, a very

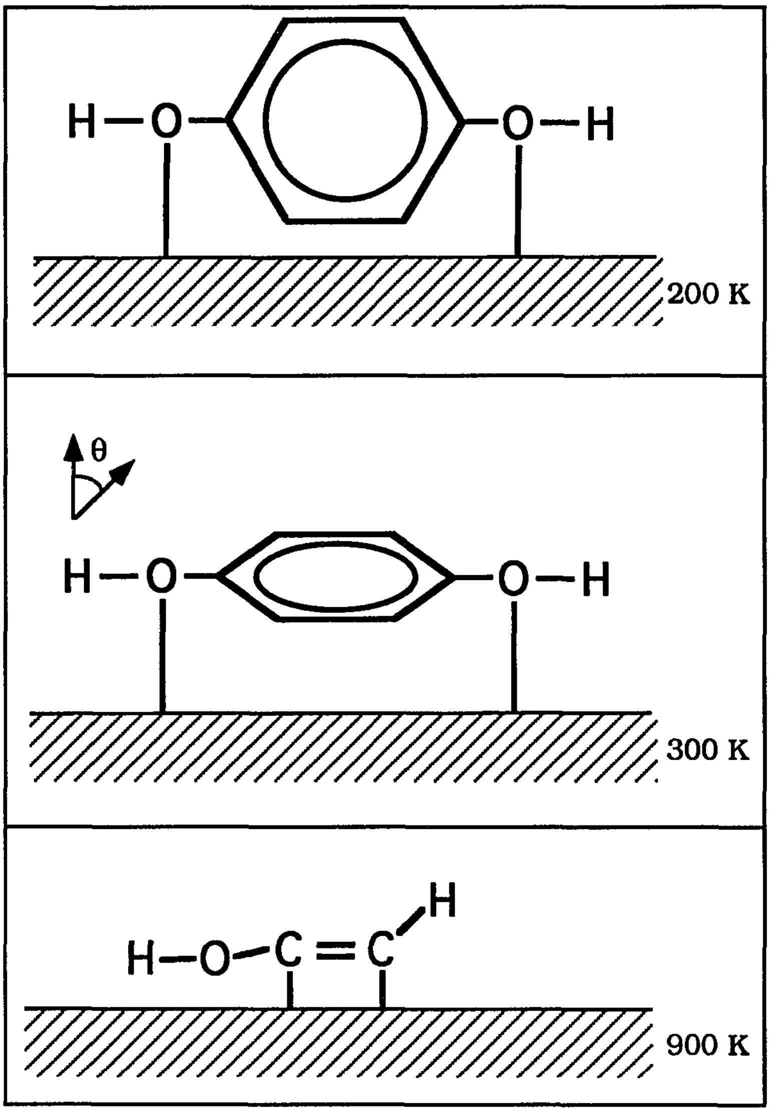

Figure 25. A proposed model for the temperature dependence of the orientation of hydroquinone on Ag(111).

weak molecular state is observed in the TDS spectrum (cf. Figure 10). At 300 K, the intensity of the 555 cm^{-1} peak is increased with respect to the 780 cm^{-1} feature. Now, the EEL spectrum suggests a strong 555 cm^{-1} feature, corresponding to the ν_{16b} vibrational mode of benzene. This symmetry species belongs to the totally symmetric representation only of point group C_s (i.e., representing a parallel orientation) and it obeys the metal-surface selection rule. However, since the remaining loss features at this temperature are assigned to representations in the C_{2v}^* point group (i.e., representing a perpendicular orientation), we predict a tilted orientation at this temperature.

By 900 K, only one peak is observed in the hydroquinone EEL spectrum, appearing at 3050 cm^{-1}. As previously discussed, this feature is assigned to a ν_{CH} stretch, presumably due to an ethylinic hydrocarbon residue on the surface. Thus, by 900 K, either the hydroquinone has molecularly desorbed or decomposed to only hydrocarbon fragments, as depicted in Figure 25.

The temperature dependent model just described suggests molecular desorption, reorientation, and irreversible decomposition of hydroquinone on Ag(111). At 280 K, some hydroquinone desorbs molecularly and some hydroquinone species reorients on the surface and desorbs around 400 K. The remaining hydroquinone decomposes to a hydrocarbon residue by 900 K, and the frequency of the ν_{CH} stretch present at this temperature suggests a residue that is ethylinic in nature. Evidence of an ethylinic hydrocarbon residue may be found in the TDS data. Recall the mass 66 feature observed at ~240 K, presumably leaving an ethylinic alcohol species (mass 44) on the surface. The presence of this species at 900 K may account for the ν_{CH} stretch observed in the EEL spectrum at this temperature; however, since no mass 44 TDS data is available, this reaction pathway can only be hypothesized at this time. Further, studies of phenol on Mo(110) suggest that two species coexist on the surface, phenoxide and either phenoxide adsorbed on a different site or molecular phenol [25]. In this study of hydroquinone, the high temperature TDS state may represent a di-hydroxide species; however, our EELS data cannot unambiguously distinguish between a molecular hydroquinone or a di-hydroxide species. Our data do, however, suggest a reorientation of the adsorbed species upon surface heating.

5. CONCLUSIONS

We identify and characterize three di-hydroxybenzene molecules adsorbed on Ag(111) using thermal desorption and high resolution electron energy loss spectroscopies. The molecules studied include catechol, resorcinol, and hydroquinone. All three molecules exhibit associative adsorption at 200 K and molecular desorption at temperatures below 400 K. Catechol desorbs molecularly at 240 K, resorcinol exhibits molecular desorption at 240 K, 280 K and ~380 K, and hydroquinone desorbs molecularly at 250 K, 290 K and ~380 K. Further, the TDS and EELS data for all three compounds suggest no dehydrogenation upon adsorption or molecular desorption; however, our data cannot unambiguously rule out O-H bond scission. Further, in all three cases, the EEL spectra indicate that some of the di-hydroxybenzene molecule remains on the surface at 300 K, suggesting some irreversibly bound molecular species. Decomposition to a hydrocarbon residue is observed in each case. We observe catechol decomposition by 700 K, decomposition of resorcinol by 800 K, and by 900 K, hydroquinone is decomposed to a hydrocarbon residue.

The vibrational losses observed in the EEL spectra can be assigned by comparison to normal vibrational modes of the benzene molecule and by comparison with assignment made by others in previous studies. Upon adsorption of catechol at 200 K, the EELS loss features indicate an inclined orientation on the surface; however, the EEL spectra of resorcinol and hydroquinone at this temperature suggest a perpendicular orientation. By

300 K, the catechol's orientation becomes more perpendicular; whereas, resorcinol's and hydroquinone's becomes more inclined. Irreversible decomposition is observed for catechol, resorcinol and hydroquinone at 700, 800 and 900 K, respectively.

REFERENCES CITED

1. M. G. Ramsey, G. Rosina, D. Steinmüller, H. H. Graen and F. P. Netzer, Surf. Sci. 232 (1990) 266.

2. B. F. Lewis, W. M. Bowser, J. L. Horn, T. Luu and W. N. Weinberg, J. Vac. Sci. Technol. 11 (1974) 262.

3. B. E. Kahn, S. A. Chaffins, J. Y. Gui, F. Lu, D. A. Stern and A. T. Hubbard, Chem. Phys. 141 (1990) 21.

4. N. Batina, D. G. Frank, J. Y. Gui, B. E. Kahn, C.-H. Lin, F. Lu, J. W. McCargar, G. N. Salaita, D. Stern, D. C. Zapien and A. T. Hubbard, Electrochim. Acta 34 (1989) 1031.

5. V. K. F. Chia, M. P. Soriaga and A. T. Hubbard, J. Phys. Chem. 91 (1987) 78.

6. J. H. White, M. P. Soriaga and A. T. Hubbard, J. Electroanal. Chem. 177 (1984) 89.

7. M. P. Soriaga, J. H. White and A. T. Hubbard, J. Phys. Chem. 87 (1983) 3048.

8. F. Lu, G. N. Salaita, L. Laguren-Davidson, D. A.Stern, E. Wellner, D. G. Frank, N. Batina, D. C. Zapien, N. Walton and A. T. Hubbard, Langmuir 4 (1988) 637.

9. Material Safety Data Sheet, Aldrich Chemical Co.

10. P. A. Redhead, Vacuum 12 (1962) 203.

11. E. Pretsch, T. Clerc, J. Seibl and W. Simon, Tables of Spectral Data for Structure Determination of Organic Compounds (Springer-Verlag, Berlin Heidlberg, 1983).

12. B. E. Bent, C. M. Mate, C.-T. Kao, A. J. Slavin and G. A. Somorjai, J. Phys. Chem. 92 (1988) 4720.

13. L. L. Kesmodel and J. A. Gates, Surf. Sci. 111 (1981) L747.

14. H. Ibach and S. Lehwald, J. Vac. Sci. Technol. 15 (1978) 407.

15. B. E. Bent, C. M. Mate, J. E. Crowell, B. E. Koel and G. A. Somorjai, J. Phys. Chem. 91 (1987) 1493.

16. L. L. Kesmodel, G. D. Waddill and J. A. Gates, Surf. Sci. 138 (1984) 464.

17. J. T. Roberts and C. M. Friend, J. Chem. Phys. 88 (1988) 7172.

18. D. Seinmuller, M. G. Ramsey, F. P. Netzer and M. Neuber, Surf. Sci. 271 (1991) 567.

19. G. Varsányi, Assignments For The Vibrational Spectra of Seven Hundred Benzene Derivatives, Volume 1, (John Wiley & Sons, Inc., New York, 1974).

20. M. V. Thiel, E. D. Becker and G. C. Pimentel, J. Chem. Phys. 27 (1957) 486.

21. G. C. Pimentel and A. L. McClellan, The Hydrogen Bond (Reinhold, New York, 1960).

22. J. L. Solomon, R. J. Madix and J. Stöhr, Surf. Sci. 255 (1991) 12.

23. A. K. Myers and J. S. Benziger, Langmuir 5 (1989) 1270.

24. M. Soriaga and A. T. Hubbard, J. Am. Chem. Soc. 104 (1982) 2735.

25. C. M. Friend in: Adsorption Structure of Organic Molecules on Mo(110), Vol. 17 (Springer-Verlag Berlin, Heidleberg, 1989) p. 67.

26. G. R. Schoofs and J. B. Benziger, J. Phys. Chem. 92 (1988) 741.

27. A. Furlani, M. V. Russo and F. Cataldo, Syn. Metals 29 (1989) E507.

28. K. Yamamoto, T. Asada, H. Nishide and E. Tsuchida, Chem. Lett. (1989) 65.

29. R. M. Silverstein, G. C. Bassler and T. C. Morrill, Spectrometric Identification of Organic Compounds, Fourth Edition (John Wiley & Sons, Inc., New York, 1981).

PART 3:

THE SURFACE CHARACTERIZATION OF PYROGALLOL ON Ag-COATED POLYESTER AND ON Ag(111): AN EELS STUDY

1. INTRODUCTION

As described in the previous two sections of this text, phenolic functionalities are often added as adhesion promoters, to enhance the adhesive bonding of a polymer to a substrate [1]. Recall that a phenolic functionality is defined as a compound similar to phenol, i.e., a benzene ring with pendant hydroxyl groups. We are interested in examining the effect of position and number of hydroxyl substituents on the metal-surface bond.

Previous chapters described the surface chemistry of phenol and three dihydroxybenzene molecules. In this chapter, we describe the surface characterization of 1,2,3-tri-hydroxybenzene, or pyrogallol. Pyrogallol, illustrated in Figure 1, is the most complex hydroxybenzene compound studied in this work. We are motivated to study its surface chemistry on Ag(111) because pyrogallol is a starting material for polymeric films formed on silver substrates; the films have potential industrial significance.

Pyrogallol has been studied by linear potential scan voltammetry and potential-step chronocoulometry using thin-layer electrodes. In the previous study, pyrogallol was deposited from solution on a smooth Pt electrodes, and was determined to lie flat (i.e., parallel) on the electrode surface. Pyrogallol has not been studied using EELS or any other surface science technique, to the best of this author's knowledge.

As described previously, great pains are taken with all of the hydroxybenzenes to ascertain their purity within the sample bulb and also

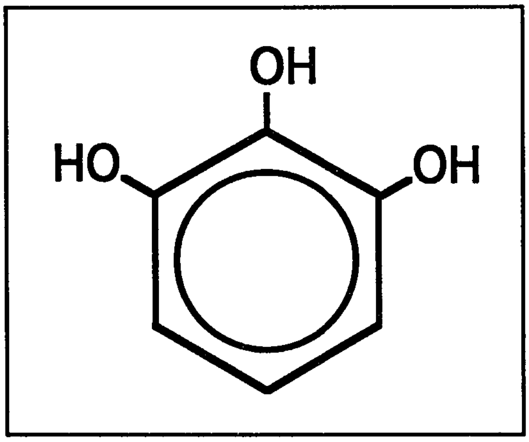

Figure 1. Diagram of the pyrogallol molecule.

after introduction to the UHV chamber via the gas doser. While the four simpler hydroxybenzenes discussed until now could be introduced to the UHV chamber with little apparent decomposition (except a minor amount of decomposition to phenol), this proved not to be the case for pyrogallol. Severe, yet sporadic, problems were encountered in producing pyrogallol within the UHV environment. These problems were never completely alleviated, despite our intense efforts.

The following material is divided into two parts. First, we describe these problems and our efforts to solve them, and also present a possible reaction model to explain their origin. Second, we present EELS data for pyrogallol films obtained during a period when the decomposition problems were not severe. We compare these EELS data with data obtained for industrially-prepared films, and with EELS data for the simpler hydroxybenzenes presented in preceding sections.

2. EXPERIMENTAL

The pyrogallol experiments were performed in a standard stainless steel UHV chamber with a typical base pressure of ~1 to 2 x 10^{-10} Torr. A complete description of this chamber, along with a schematic diagram, can be found in the Experimental Procedures section of this dissertation. Experimental details specific to the pyrogallol study are included below.

The pyrogallol used in this study is reagent grade, purchased from Aldrich and specified as 99% pure. The pyrogallol is used without further purification except to pump out any volatile impurities from the sample bulb. Pyrogallol is air and light sensitive [2]; thus, special precautions must be taken in its storage and handling. Further, pyrogallol is a difficult molecule to work with as it is a solid with a very low vapor pressure at room temperature. The low vapor pressure makes it difficult to introduce pyrogallol into the vacuum chamber. Also, pyrogallol is very sensitive to heating and decomposes if the temperature is raised too fast or too high.

Initially, due to pyrogallol's low vapor pressure, we devised a method similar to head space analysis in gas chromatography to introduce the vapor into the chamber. In this method, the glass sample bulb was immersed in an oil bath and the bath was heated to 70-75 ^{o}C, yielding a reasonably high pyrogallol vapor pressure (later measured with a thermocouple gauge under similar conditions at 500-1000 mTorr). Components of the manifold external to the UHV system were also heated to about 50-75 ^{o}C with heating tapes, to help prevent pyrogallol condensation. In this early arrangement, the vapor could *only* be directed straight into the mass spectrometer ionizer, as shown in Figure 2.

With this apparatus, the pyrogallol looked pure; that is, a mass spectrum of the vapor introduced directly into the mass spectrometer showed only major fragments attributable to pyrogallol. This spectrum is shown in Figure 3; the table accompanying this figure shows that the major fragments we observed were the same as those reported in the literature [3]. Relative intensities were slightly different, perhaps due to the fact that spectra in the literature and from our lab were obtained with different types of spectrometers. Note particularly that Figure 3 shows no peak at mass 136.

The apparatus of Figure 2, however, had several severe drawbacks, which prompted us to build the improved system shown in Figure 4. The main changes included substitution of four glass bulbs for the single one, allowing a larger reservoir of pyrogallol, and addition of a more elaborate (and longer) stainless steel manifold. This manifold could route pyrogallol vapor directly to the surface of the crystal (left side of Figure 4), or it could direct the gas straight into the mass spectrometer ionizer (right side of Figure 4), without losing vacuum. The latter part of this manifold is constructed specifically to facilitate checks of gas purity.

Irreproducible results obtained in preliminary TDS experiments prompted us to recheck the composition of the pyrogallol vapor. We obtained the new pyrogallol cracking pattern shown in Figure 5; note it has changed substantially from that shown in Figure 3. Although traces of

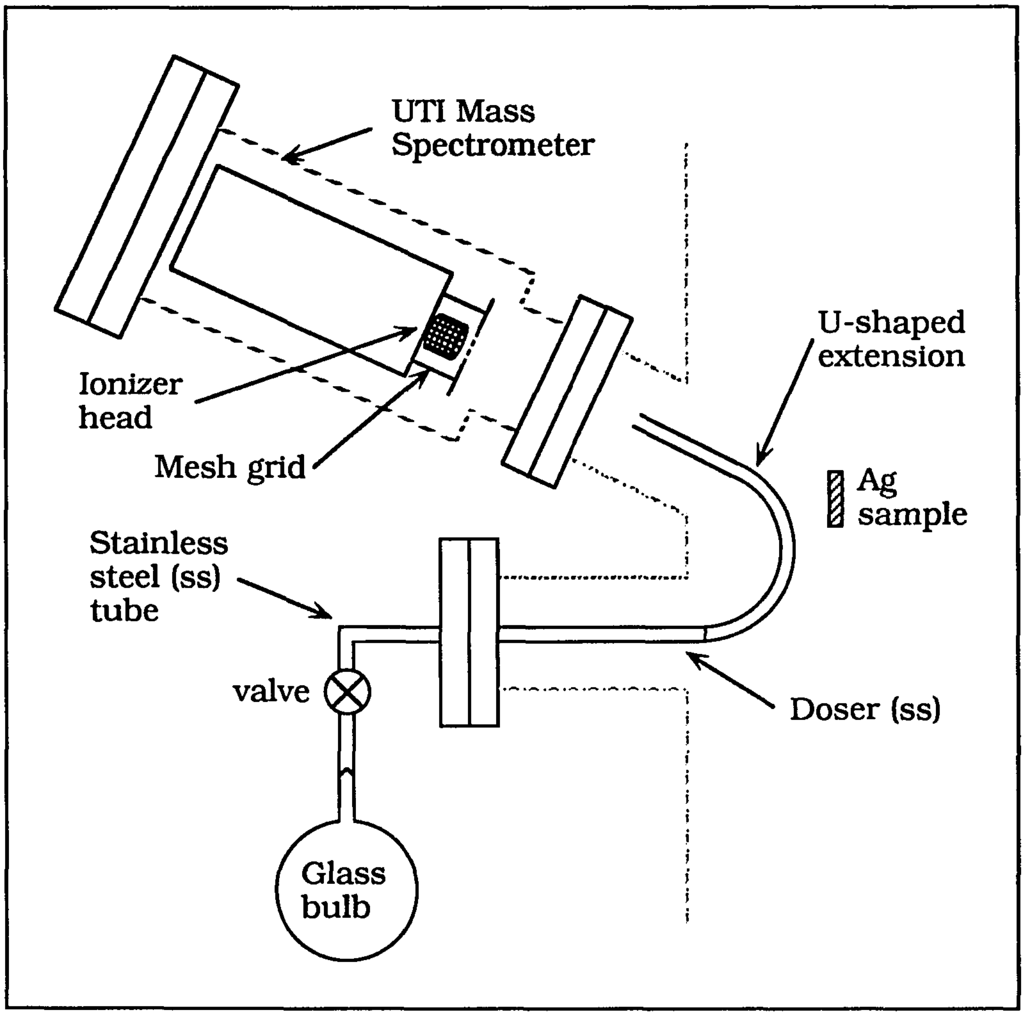

Figure 2. Schematic diagram of the original dosing apparatus.

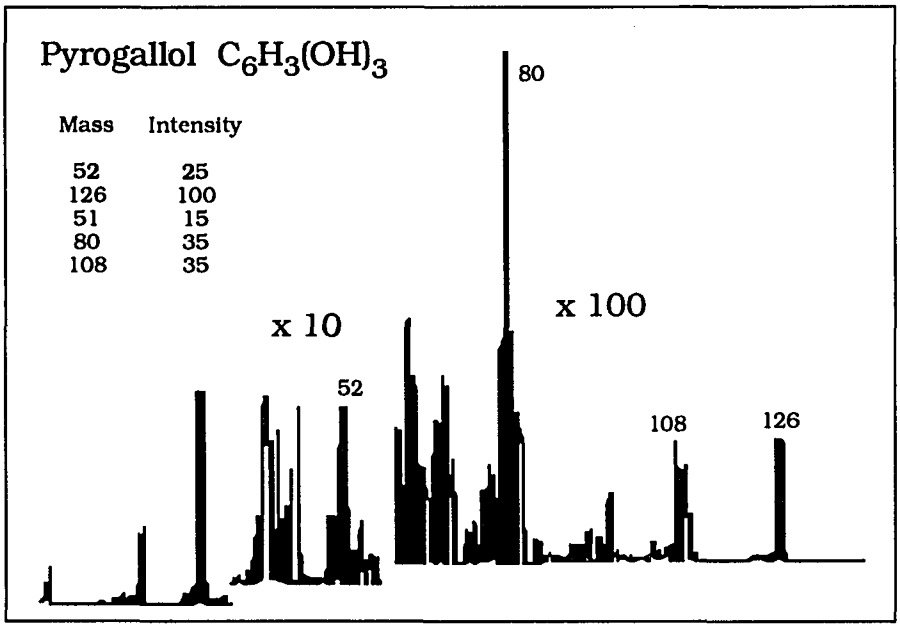

Figure 3. Initial mass spectrum of pyrogallol in the UHV chamber using the original dosing apparatus. Electron energy is 70 eV.

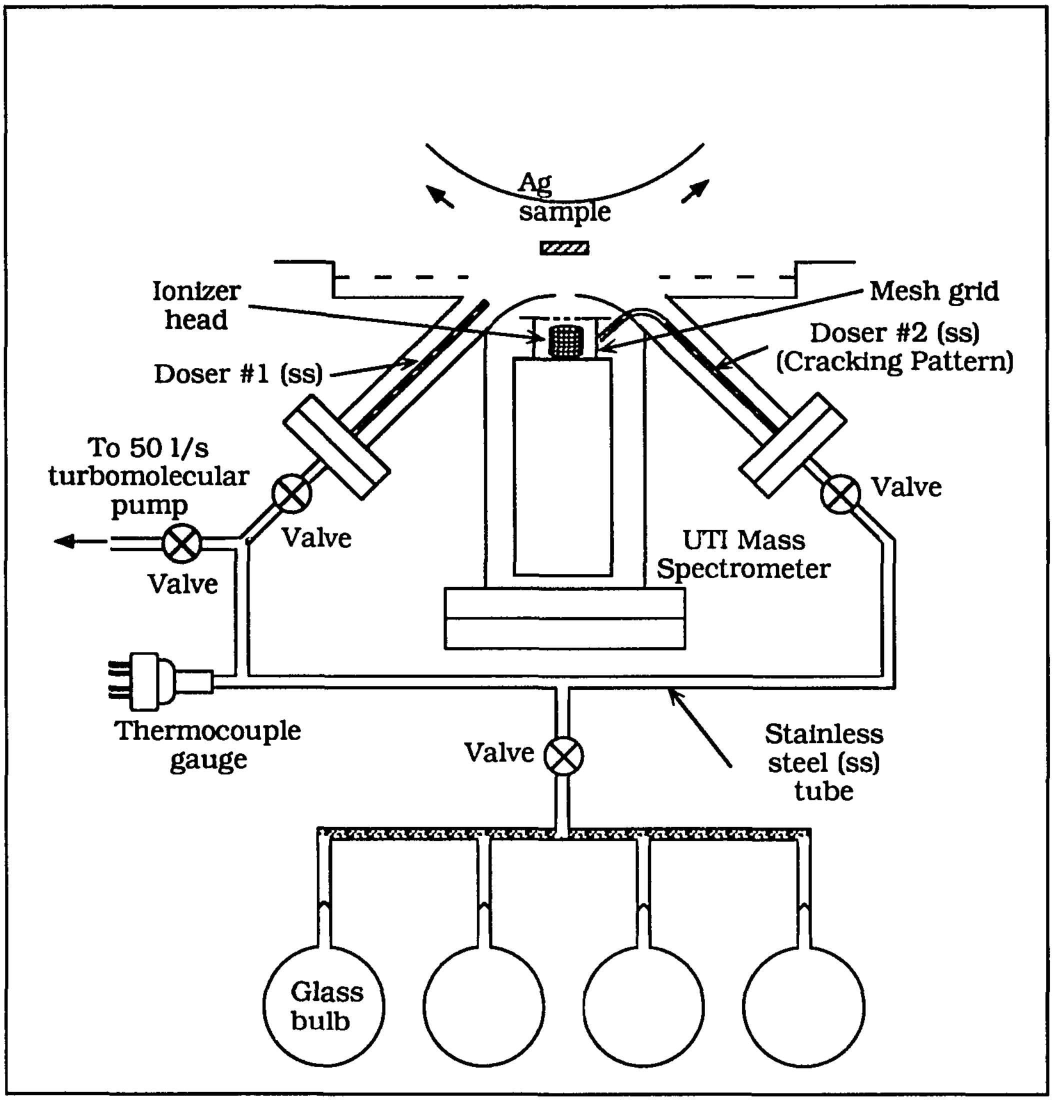

Figure 4. Schematic diagram of the improved dosing apparatus, including the stainless steel manifold.

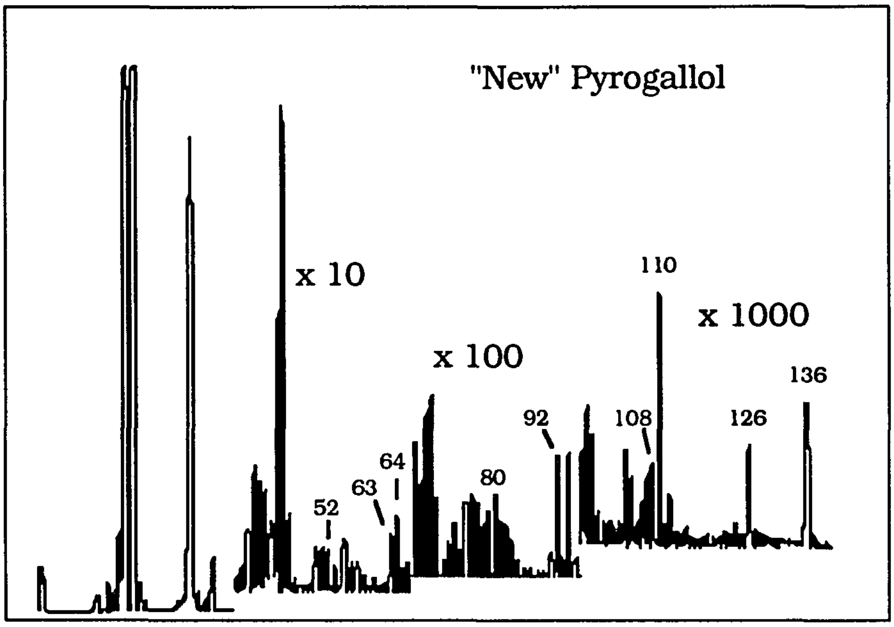

Figure 5. Mass spectrum of "new" pyrogallol in the UHV chamber using the stainless steel manifold. Electron energy is 70 eV.

the characteristic pyrogallol fragments are still visible, the spectrum in Figure 5 shows new, abundant fragments at masses 63 and 64, with smaller new features at masses 136 and 110. Clearly, the vapor being introduced at the silver surface was no longer pure pyrogallol; indeed, it was no longer even predominantly pyrogallol.

We suspected several possible sources of this degradation problem and set out to make the appropriate changes. First, the pyrogallol in the sample bulbs was replaced several times, and in several different ways; a new batch of pyrogallol was obtained from the vendor and tested; the pyrogallol was purified under vacuum with freeze-thaw cycles; the chamber was purged with flowing pyrogallol for extended periods of time; the thermocouple gauge (with its hot filament) was left unused, and even removed entirely from the system; the configuration of the gas introduction system immediately adjacent to the mass spectrometer was rearranged such that the vapor was not routed directly into the hot filament of the ionizer; a water bath was used instead of an oil bath to heat the glass sample bulbs; the mass spectrometer was re-tuned using xenon to calibrate the high-mass range; a stainless steel sample bulb was substituted for the glass; and finally, the entire manifold was disassembled, cleaned, and reassembled. None of these changes, however, alleviated the degradation problem.

Our next approach was to have independent purity tests of the pyrogallol done in-house at the Chemistry Department Instrument Services Facility using a solid probe, Finnigan 4000 quadrupole mass spectrometer. The mass spectrum of the pyrogallol obtained in this manner is shown in Figure 6. This spectrum confirms that, indeed, the material in the sample bulb is pure pyrogallol. However, the pyrogallol vapor was passed into the solid probe mass spectrometer differently than into our mass spectrometer. To compensate for this difference, an all-stainless steel manifold was assembled, similar to that used on our chamber, and interfaced with the solid probe mass spectrometer in the Instrument Services Lab. Using this arrangement to mimic our experiments, we obtained the mass spectrum shown in Figure 7: note the peaks at masses 136, 110, 63, and 64. These results indicated that the pyrogallol in the storage bulbs was pure, but the vapor passing *through* the stainless steel manifold was not. Furthermore, the reaction products detected with the solid probe mass spectrometer, after passing through a steel manifold, were the same or very similar to the ones which we had detected using our UHV chamber.

The cracking pattern of the degraded vapor, most noticeably the relative intensity of mass 110, was dependent upon the temperature of the oil/water bath. For instance, at 125-135 ^{o}C, the spectrum of Figure 7 was obtained, with strong intensity at mass 110 relative to mass 136. At lower temperature (70-75 ^{o}C) the spectrum at the top of Figure 8 is obtained, with lower intensity at mass 110 relative to 136. This indicated that there are at least two reaction products, distinguished by mass fragments 110 and 136. Several aromatic compounds can be identified as candidates for the high- and low-temperature reaction products, using the Instrument Services Laboratory's computerized

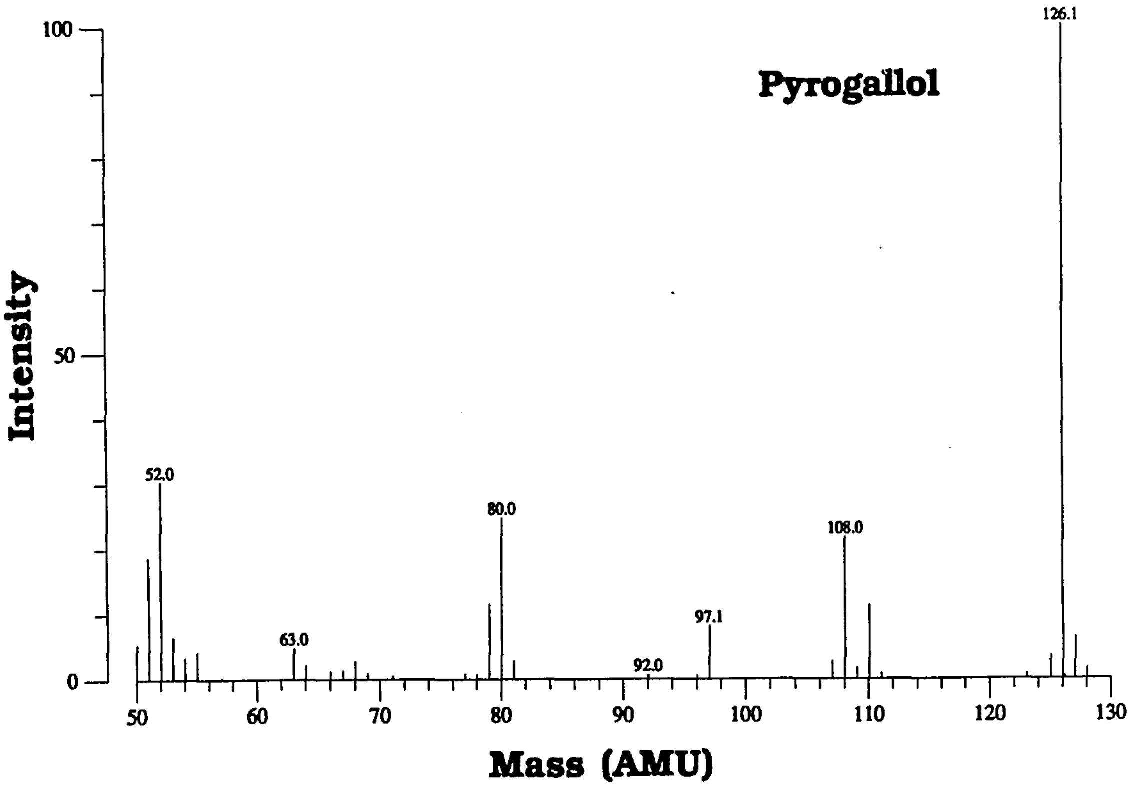

Figure 6. Mass spectrum of sample from the sample bulb, obtained from the Chemistry Department's Instrument Services. Electron energy is 70 eV.

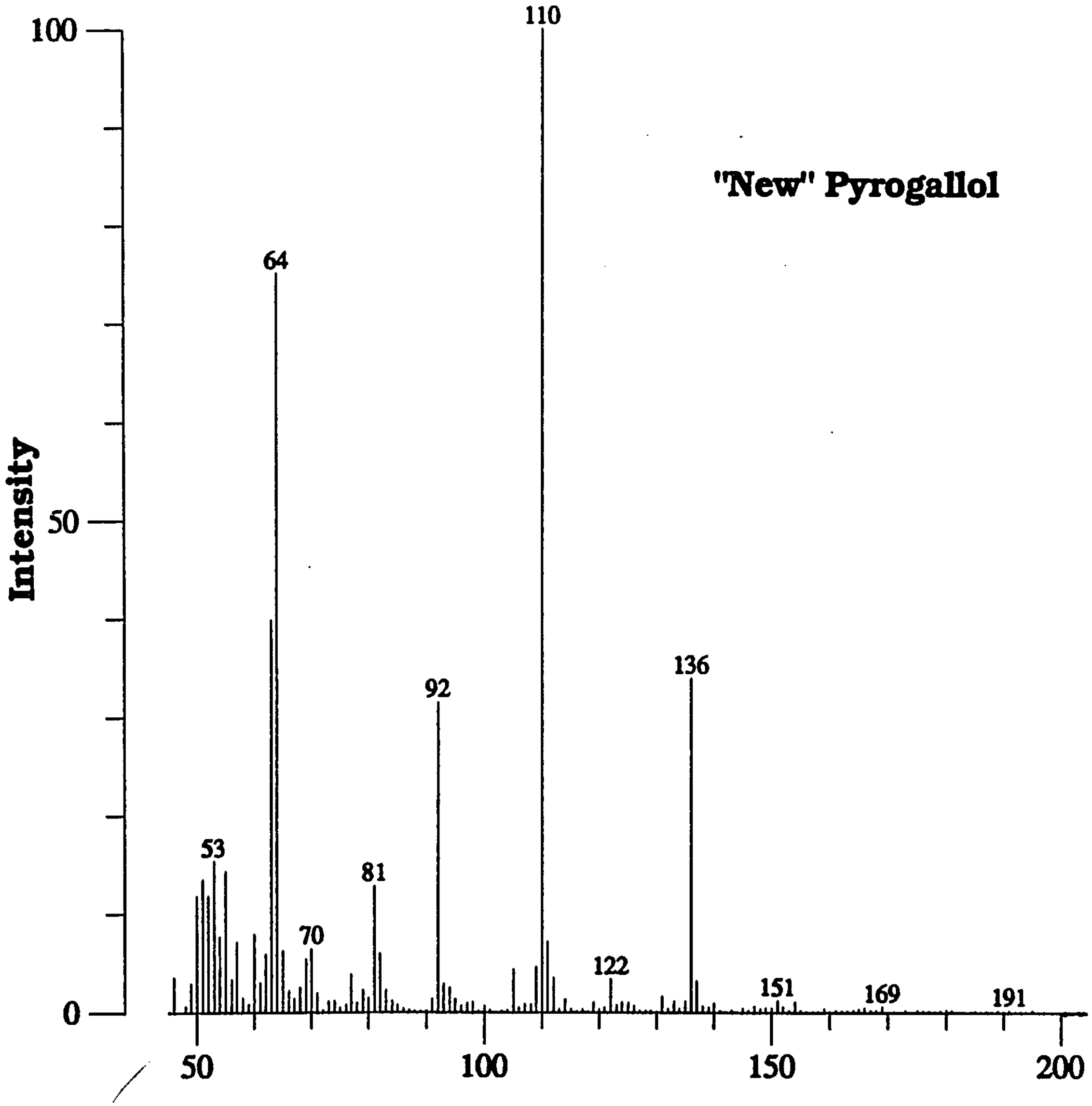

Figure 7. Mass spectrum of "New" pyrogallol through the stainless steel manifold, obtained from the Chemistry Department's Instrument Services. Electron energy is 70 eV.

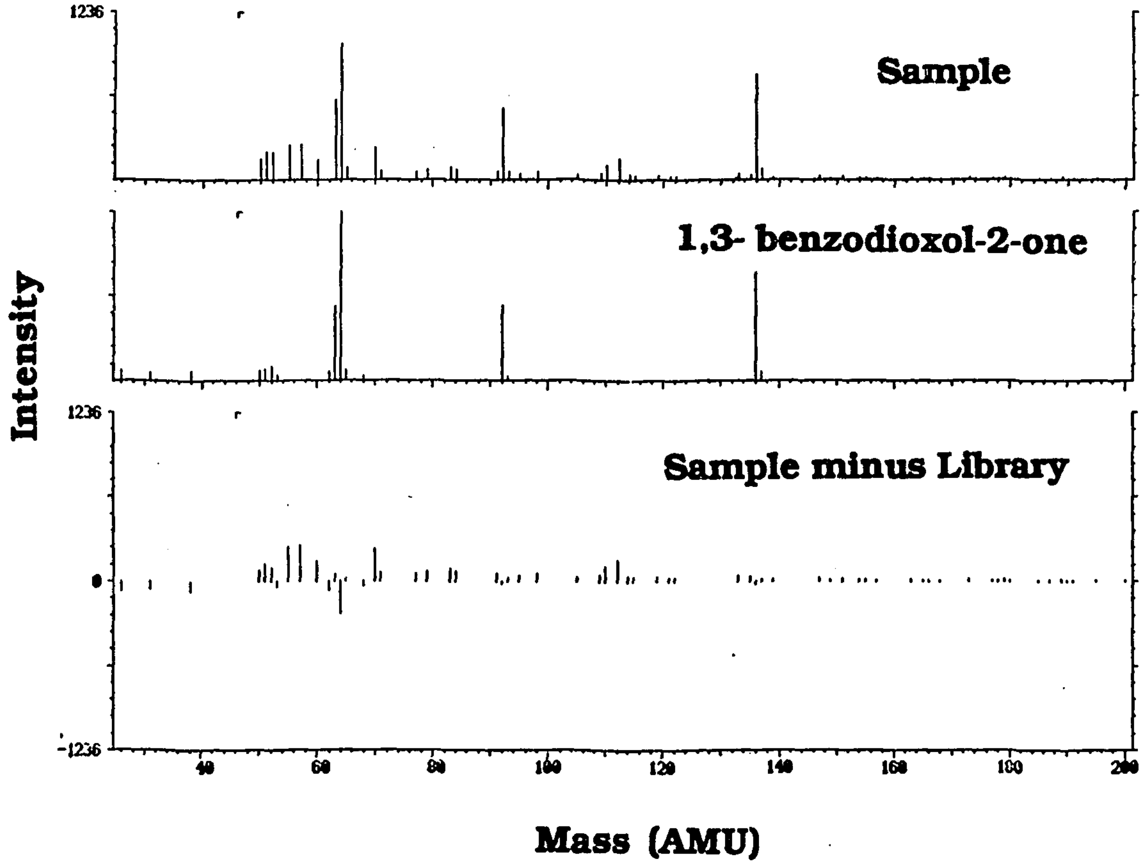

Figure 8. Comparison of the low-temperature sample (mass 136) through the stainless steel doser to a library (database) spectrum of 1,3-benzodioxol-2-one.

database. However, upon closer examination, only two yielded favorable agreement between measured and published cracking patterns.

The low-temperature (mass 136) product is probably 1,3-benzodioxol-2-one, based upon the good agreement with the published cracking pattern illustrated in Figure 8. The synthesis of this chemical from pyrogallol requires loss of two protons and addition of one carbon atom. We suggest that this most probably occurs by loss of H_2O and addition of CO, as shown in Figure 9.

The three candidates for the high-temperature (mass 110) product were 1,2-, 1,3- and 1,4-benzenediol, all of which are closely related to pyrogallol. The 1,2- and 1,3- compounds can form from pyrogallol simply by removal of one oxygen atom; however, the 1,4-compound requires, in addition, migration of a hydroxyl group on the benzene ring. These chemical structures, and their published mass spectra, are shown in Figure 10. While the data do not allow us to unequivocally pinpoint one of these three isomers as the high-temperature (mass 110) product, we feel that the most reasonable possibility is 1,2-benzenediol.

At this point, we are uncertain whether degradation of the pyrogallol is catalyzed by the stainless steel surfaces of the manifold, or whether decomposition occurs in the gas-phase. It is interesting to hypothesize that the degradation reaction is catalyzed by the stainless steel surfaces, and to note that both 1,2-benzenediol and 1,3-benzodioxol-2-one can form only if an oxygen atom is lost from the 3- (or equivalent 1-) position of the parent pyrogallol molecule. Additionally, the fact that the yields of the two species are highly

Pyrogallol

1,3-Benzodioxol-2-one

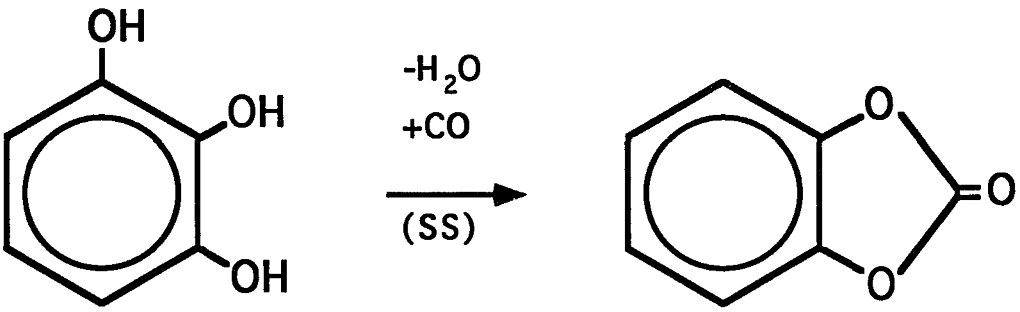

Figure 9. Proposed reaction pathway (pyrogallol to 1,3-benzodioxozl-2-one).

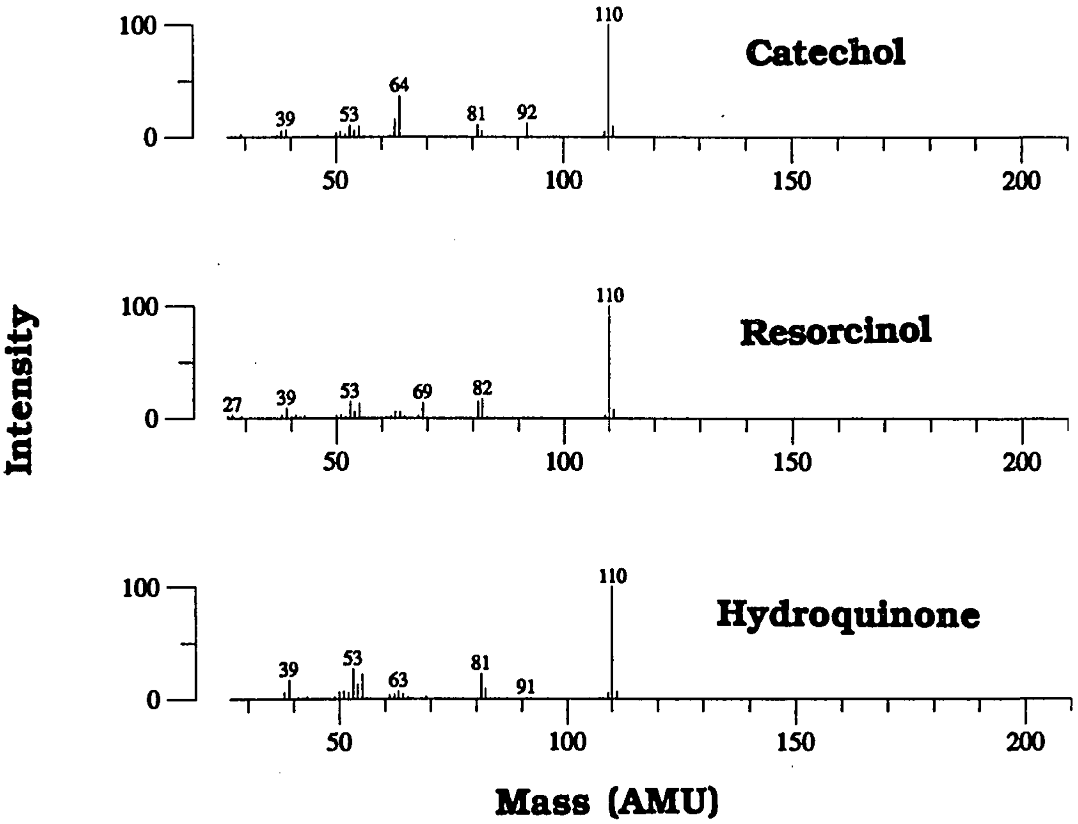

Figure 10. Library mass spectra of three possible, high-temperature (110), reaction products (catechol, resorcinol, hydroquinone).

temperature-dependent might lead one to postulate the reaction sequence shown in Figure 11, wherein the adsorbed form of the diol is a synthetic intermediate leading to the ketone. At high temperatures, the residence time of the intermediate would be so short as to make addition of CO unlikely. Note that hydrogen and CO are not contaminants in the pyrogallol; rather, they must be available for reaction either as pre-existing impurities on the stainless steel surface, or as products of pyrogallol degradation. The former explanation is disfavored by the fact that purging the chamber for long periods of time does not alleviate pyrogallol decomposition; pre-existing surface impurities would certainly have been consumed by reaction under these conditions.

According to Figure 11, two conditions must be met for the degradation reaction to proceed: dehydration must occur and stainless steel must be present to catalyze the reaction. The first step toward degradation of pyrogallol would be dehydration of the adsorbed molecule, as shown in Figure 11. Therefore, the presence of water vapor should inhibit degradation, at least by this route. Attempts to suppress degradation by deliberately introducing water to the gas phase proved unsuccessful, however, as the cracking pattern of the mixture indicated no substantial increase in mass 126 (pyrogallol) signal over the mass 136 (1,3-benzodioxol-2-one). Thus, the presence of water did not enhance the stability of pyrogallol in the gas line.

The proposed mechanism also suggests the degradation reaction is catalyzed by the stainless steel manifold. Thus, replacement of the steel manifold by an all glass one should inhibit the degradation reaction.

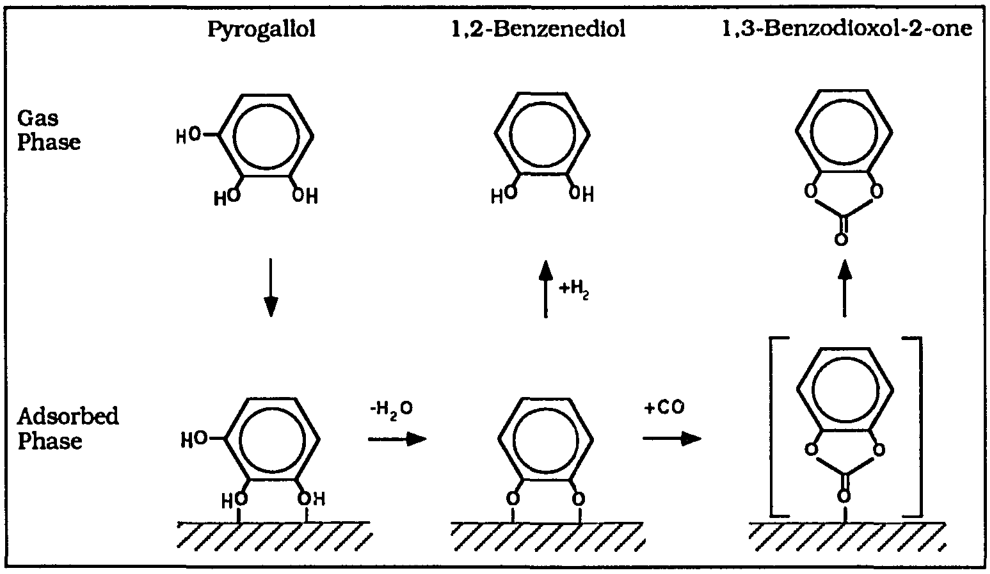

Figure 11. Proposed dehydration reaction pathway (pyrogallol to [1,2-dihydroxybenzene] intermediate to 1,3-benzodioxol-2-one).

Following up on this logic, a Pyrex dosing system (with the same configuration of the stainless steel one shown in Figure 4) was designed and fabricated; however, the all glass line introduced its own set of experimental difficulties. For example, the thermal conductivity of the glass was so low that pyrogallol recrystallizes on the Pyrex tubing, before reaching the dosing needle. This problem was somewhat alleviated by wrapping the line with heating tapes, but this method was not foolproof either, as hot and cold spots could develop along the line. Further, any pyrogallol making it into the capillary dosing needle condensed and could block the needle, since the needle itself was unwrapped in vacuum. Wrapping the needle with tungsten wire and heating it in vacuum produced no significant change in the pyrogallol mass spectrum.

Assuming that some pyrogallol must be getting into the chamber and simply not reaching the mass spectrometer, a glass extension to the capillary doser leading directly into the ionizer was attached. Hopefully, this modification would guide the pyrogallol into the mass spectrometer so its purity could be verified. However, again, there was no significant improvement in the pyrogallol mass spectrum.

To further examine this problem of introducing pyrogallol at the Ag crystal, an all glass probe was custom built for use in the Instrument Service Lab. This new probe was essentially a model of the larger system used on the UHV chamber in that it had a Pyrex glass capillary, wrapped with W wire for heating, and was attached to a glass sample bulb via a standard tube fitting connection. The probe allowed direct introduction of pyrogallol into the ionizer of a quadrupole mass spectrometer. While acquiring mass spectra, both the dosing line of the probe and the glass sample bulb were heated. The results of these experiments are described below.

Electron impact mass spectrometry (EI-MS) experiments in the Instrument Services Lab were performed in the same manner as on the UHV chamber; that is, the sample bulb and dosing line were slowly heated (up to a final temperature of 145 °C) to produce some gas-phase pyrogallol which was then leaked directly into the mass spectrometer ionizer (note that pyrogallol's melting point is ~133 °C). The results of this experiment agreed with our previous results; it appeared that no significant amount of pyrogallol (identified by the presence of mass 126) passed into the mass spectrometer. However, a large H_2O (mass 18) ion signal was observed, due either to dehydration of pyrogallol, hydroxyl groups adsorbed on the sides of the glass bulb, or a combination of the two. It is interesting to note that as the temperature of the oil bath surrounding the sample bulb reached 100 °C, the signal intensity of mass 18 decreased drastically and we observed the appearance of mass 136. Recall, mass 136 is indicative of 1,3-benzodioxol-2-one, the product of a pyrogallol molecule after losing one H_2O molecule and acquiring one CO molecule. The above observations would support our proposed reaction pathway; however, since the reaction still progressed with an all glass dosing line, it appears that stainless steel is not necessary for the reaction to proceed. Therefore, as written, the proposed reaction pathway shown in Figure 11 is probably incorrect.

On occasion, pure pyrogallol does enter the UHV chamber, and EEL spectra are obtained. Industrial films prepared from pyrogallol as a starting material are also analyzed by EELS. The following results are based on the EEL spectra obtained from pyrogallol deposited on Ag(111) and from the industrial pyrogallol films, deposited in atmosphere, on Ag films.

3. RESULTS

3.1. EELS of Pyrogallol on Ag(111)

Figure 12 shows EEL spectra for the deposition of pyrogallol on Ag(111). Curve (a) represents deposition of pyrogallol at ~250 K, curve (b) depicts the spectrum after heating the crystal to 280 K, and curve (c) is the spectrum following crystal heating to 700 K. The spectra shown are representative, and the loss frequencies reported in Table 1 are average values. Thus, the frequencies listed in Table 1 may not exactly match those in Figure 12.

As with the previously studied hydroxybenzenes, the EEL spectra of pyrogallol are rich in that at least 5 main loss features are identified. At 250 K, the first loss feature appears at 745 cm^{-1}, and is associated with the skeletal structure of the aromatic ring. The vibration is assigned to a combination of out-of-plane skeletal vibrations and the out-of-plane γ_{CH} deformation mode. This peak indicates aromaticity of the surface adsorbate, as discussed for the previous hydroxybenzene molecules; however, note its decreased intensity compared to the same peak of the other molecules studied. The second observable peak occurs at 995 cm^{-1}, and is assigned to the out-of-plane γ_{CH} deformation mode. The next prominent loss feature appears at 1470 cm^{-1}, with a low frequency shoulder at 1340 cm^{-1}. Both of these features are associated with ν_{CC} stretching modes of the benzene ring. Also, the shoulder at 1340 cm^{-1} can be assigned to a ν_{CH} stretching mode. Finally, a doublet appears in the range between 2935 and 3005 cm^{-1}, and is assigned to ν_{CH}

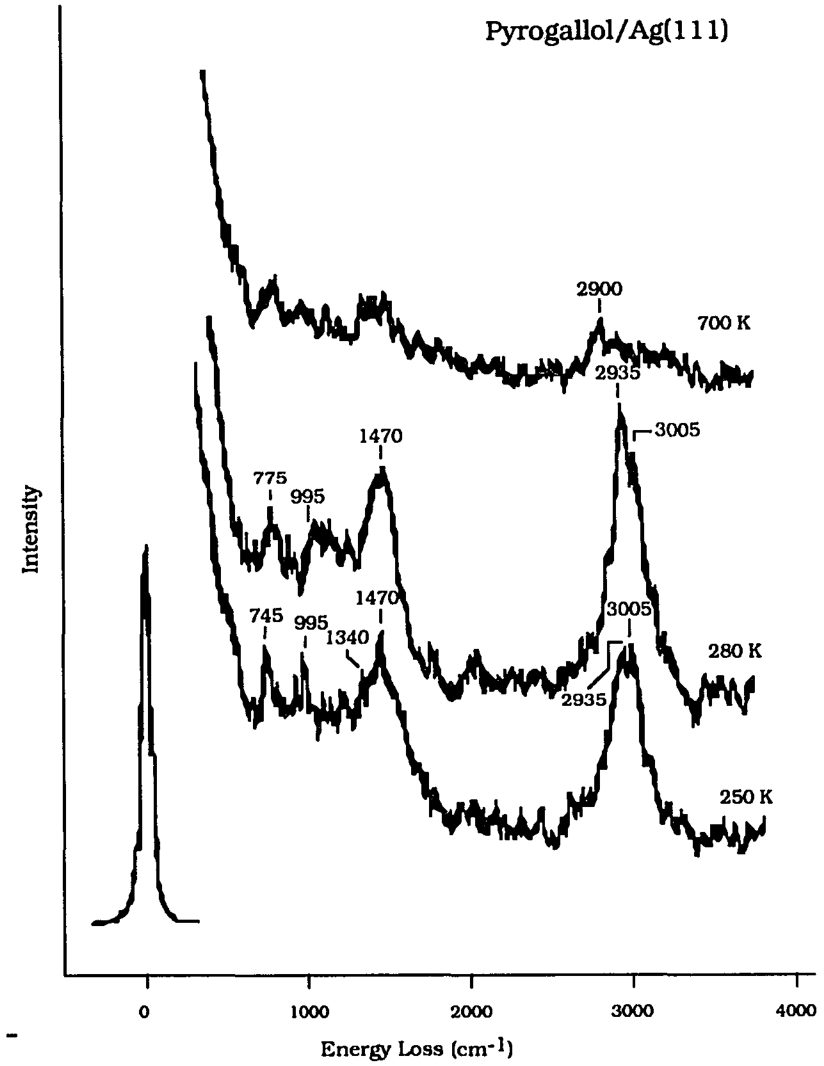

Figure 12. Electron energy loss spectra of pyrogallol on Ag(111) at (a) 250 K, (b) 250 K and (c) 700 K, deposited in UHV. The vibrational mode assignments are summarized in Table 1.

Table 1. Vibrational assignments for pyrogallol on Ag(111) and Ag-coated polyester films. Symmetry species for the C_{2v} and C_s point groups are presented. The shaded regions indicate symmetry species that represent totally symmetric representations of the respective point groups *and* obey the metal-surface selection rule.

[a] Reference [5].

Mode #	Symmetry Species		IR freq. (cm^{-1})^{a}	Intensity^{a}	Pyrogallol/ Ag(111)^{b}	Pyrogallol/ Ag/PET
	C_{2v} (⊥)	C_s (//)				
1	a_1	a'	---	---		
2	a_1	a'	---	---		
3	b_2	a"	1289	m		
4	a_2	a'	709	vs	775 - 805	775
5	a_2	a'	950	vw	995	
6a	a_1	a'	---	---		
6b	b_2	a"	562	vw		
7a	a_1	a'	---	---		
7b	b_2	a"	1001	vs		
8a	a_1	a'	1621	s		
8b	b_2	a"	1633	w		
9a	a_1	a'	320	w		
9b	b_2	a"	1141	m		
10a	b_1	a"	---	---		
10b	a_2	a'	---	---		
11	b_2	a'	761	s	775 - 805	
12	b_2	a'	841	m		
13	a_1	a'	1243	s	1230	
14	a_1	a"	1366	s	1370	~1300
15	a_2	a"	---	---		
16a	b_1	a"	---	---		
16b	a_2	a'	578	w		
17a	a_2	a"	---	---		
17b	b_1	a'	---	---		
18a	b_2	a"	1063	s		
18b	a_1	a"	369	w		
19a	b_2	a'	1524	vs		
19b	a_1	a"	1487	vs	1470	1470
20a	b_2	a'	1323	vs	1370	~1300
20b	a_1	a"	3055	w	2900/3005	2935
ν_{OH}	a_1	a'	3250-3450	3 maxima		
β_{OH}	b_2	a"	1190	vs		
γ_{OH}	b_1	a'	501	vs		

stretching mode. The low frequency of this peak is indicative of aromatic C-H stretches.

The 280 K pyrogallol spectrum shown in curve (b) is quite similar to that of curve (a); only minor changes are observed. First, the peak at 745 cm^{-1} is shifted up to 775 cm^{-1}. Second, the 1470 cm^{-1} feature is more defined and appears more intense, relative to the 775 and 995 cm^{-1} features. Further, the doublet feature in the high frequency region is now a prominent peak at 2935 cm^{-1} with a high frequency shoulder at 3005 cm^{-1}. The vibrational mode assignments for these features all remain the same.

After heating the crystal to 700 K, the EEL spectrum evidences only very broad, low intensity loss features. A very broad feature is observed in the range between 805 and 1470 cm^{-1}, and another low intensity feature is observed at ~2900 cm^{-1}. The features are most likely due to a hydrocarbon residue resulting from decomposition of pyrogallol on the surface.

3.2. EELS of Industrial Pyrogallol Films

Figure 13 shows EEL spectra for the deposition of pyrogallol on Ag-coated polyester (PET) films at atmospheric pressure. The spectra shown are representative of several taken at different times, and the loss frequencies reported in Table 1 are average values. Thus, the frequencies in Table 1 may not exactly match those of Figure 13.

In the pyrogallol film spectrum shown in Figure 13, three prominent features are observed. The first loss feature appears at

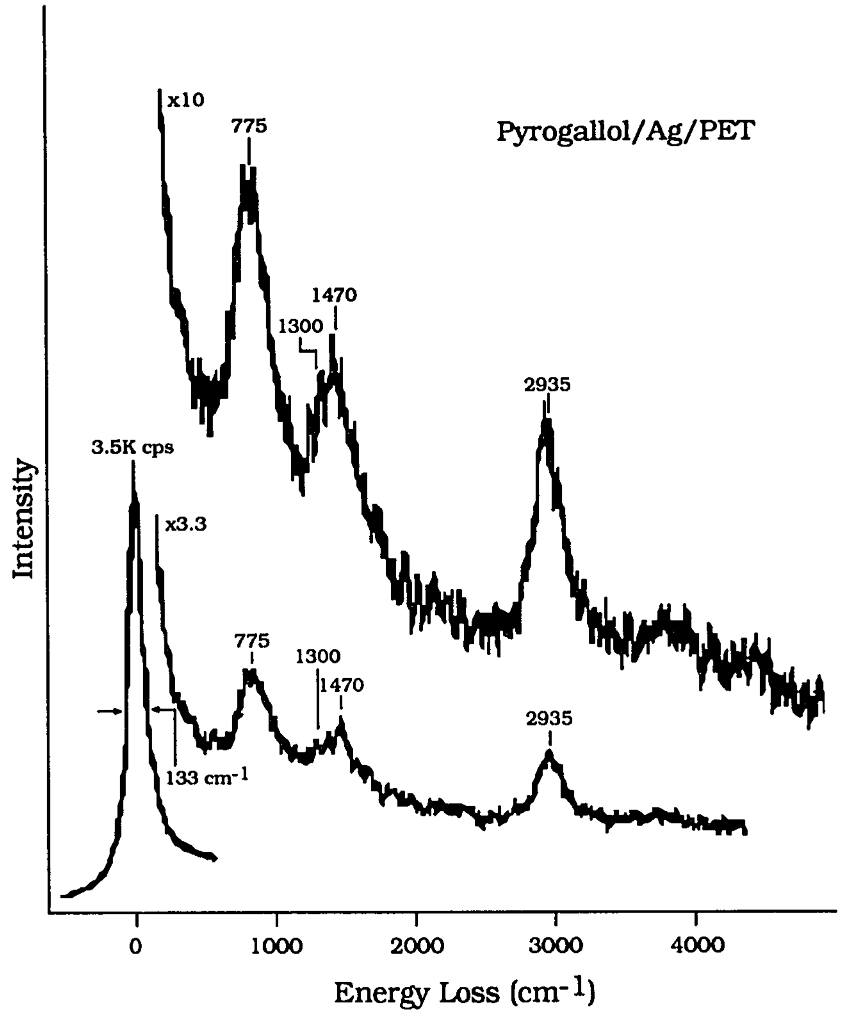

Figure 13. Electron energy loss spectrum of industrial pyrogallol films on Ag-coated polyester films. The vibrational mode assignments are summarized in Table 1.

755 cm^{-1}, and is assigned to a combination of out-of-plane skeletal vibrations and an out-of-plane γ_{CH} deformation mode. Both of these modes are associated with skeletal vibrations of the benzene ring. The second most prominent feature occurs in the frequency range between ~1300 and 1470 cm^{-1}. We assign this feature to two ν_{CC} stretching modes. Finally, the last loss feature occurs at 2935 cm^{-1} and is assigned to the ν_{CH} stretching mode. The low frequency of this feature suggests aromaticity of the adsorbed species.

4. DISCUSSION

This study allows the identification, structural characterization and comparison of pyrogallol deposited on Ag(111) and Ag films. We compare the EELS results of the pyrogallol films with those of the simpler hydroxybenzenes discussed previously and with published IR spectra to identify and assign the observed loss features. Features in the EEL spectra indicate the retention of aromaticity in the industrial pyrogallol films as well as in the films deposited under UHV conditions. Further, the EELS results suggest no dehydrogenation (i.e., O-H bond scission) upon adsorption, however, the possibility still exists. Finally, an inclined molecular orientation is postulated, and a model is proposed.

4.1. Retention of Aromaticity

Table 1 summarizes the observed loss features in the EEL spectra of both the UHV deposited and industrially prepared pyrogallol films. All pyrogallol vibrational mode assignments are made by comparison to the normal modes of the benzene molecule as described in the Introduction of this dissertation. Thus, the pyrogallol assignments are numbered according to the benzene vibrational mode convention. The fact that *all* of the observed loss features correspond to normal modes of the benzene molecule is a strong indication of the aromatic nature of the adsorbed species.

At least two loss features observed in the 250 K, 280 K and industrially deposited pyrogallol EEL spectra suggest aromatic character in the adsorbed species. The feature centered between 745 and 805 cm^{-1} is associated with the ν_4 and ν_{11} vibrations of the benzene ring. The ν_4 mode represents out-of-plane skeletal stretches, also described as a "C-C-C puckering" of the aromatic ring. The ν_{11} mode originates from γ_{CH} out-of-plane bending modes. Further, losses in this frequency range can indicate the type of substitution in benzene derivatives, and in this case, indicates a 1,2,3- trisubstituted benzene [4]. As indicated in Table 1, the intensity of this feature is very strong in IR spectra, and in fact does appear very strong in the previous EEL spectra of the simpler hydroxybenzene molecules. In the pyrogallol films, this feature appears with only a medium intensity; however, the mere presence of a loss at this frequency strongly indicates an aromatic species.

Further indication of aromaticity in the adsorbed species is evidenced by the ν_{CH} stretch centered between 2935 and 3005 cm^{-1} in these same pyrogallol EEL spectra. This feature is assigned to the ν_{20b} vibrational mode of the benzene ring. Generally, ν_{CH} stretches for aromatic and ethylinic C-H bonds occur in the range between 3030 and 3080 cm^{-1}, whereas for aliphatic and acetylinic C-H stretches occur at much lower or higher frequencies, i.e., 2840 to 3000 cm^{-1} for aliphatic ν_{CH} stretches and 3250 to 3340 cm^{-1} for acetylinic ν_{CH} stretches [4]. Further, it is common to observe multiple peaks in this region [4] as is present in the EEL spectrum of the UHV deposited pyrogallol film. Therefore, due to the frequency of the observed ν_{CH} stretch, the adsorbed species is indeed aromatic.

After heating to 700 K, most of the features in the UHV deposited pyrogallol film EEL spectrum appear as very broad, low intensity losses. A very low intensity, broad feature appears in the range between 805 and 1470 cm^{-1}, and another broad feature centered around 2900 cm^{-1} is observed. The absence of a definite peak around 805 cm^{-1} and the low frequency of the 2900 cm^{-1} feature suggest loss of aromaticity in the adsorbed species at this temperature. As mentioned in the previous paragraph, the low frequency of the ν_{CH} stretch indicates aliphatic C-H stretches. Thus, by 700 K, the adsorbed species no longer appears aromatic.

4.2. Dehydrogenation

Although no TDS data exist for the pyrogallol films, we can hypothesize about possible dehydrogenation (O-H bond scission) upon adsorption on Ag(111). All the EEL spectra evidence an absence of a ν_{OH} stretch. If present, this loss should appear in the range between 3250 and 3450 cm^{-1} [5]. Using only evidence obtained from the EEL spectra, three possible explanations exist for the absence of this feature: (a) O-H bond scission upon adsorption, (b) hydrogen bonding on the surface or (c) parallel orientation of the O-H bond in accordance with the metal-surface selection rule. Note that only one of these explanations invokes O-H bond scission. If O-H bond scission occurs, we would not expect to observe a ν_{OH} stretch in the EEL spectra [6]. Figure 14 shows how the dehydrogenated surface species might appear on Ag(111).

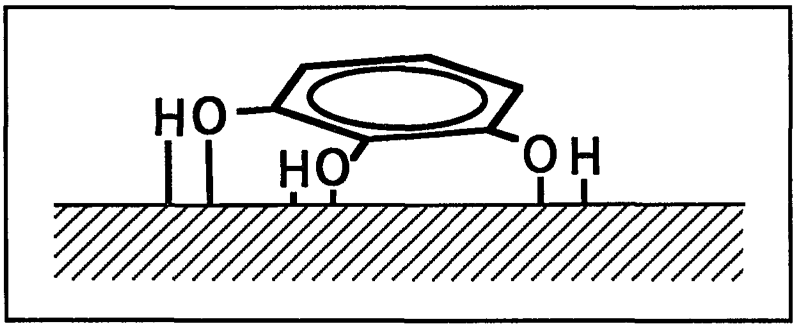

Figure 14. Diagram of dehydrogenated pyrogallol on Ag(111).

A second possibility, hydrogen bonding between adjacent pyrogallol molecules could also explain the absence of a ν_{OH} stretch. Hydrogen bonded O-H bonds have small scattering cross sections in EELS and IR [7, 8], thus, one might expect to observe only a very weak ν_{OH} stretch, or none at all. Further, evidence of hydrogen bonding between adsorbed phenol molecules has been observed previously [9, 10]. Figure 15 shows how hydrogen bonded pyrogallol species might appear on the surface. Thus, the absence of a ν_{OH} stretch does not conclusively indicate O-H bond scission.

Finally, the orientation of the O-H bond axis may make the ν_{OH} stretch virtually invisible in the EEL spectra, in accordance with the metal-surface selection rule. One can envision this possibility in two ways: either the entire pyrogallol molecule lies flat on the surface, or at least the axis of the O-H bonds lie parallel to the surface. Figure 16 shows these two possible orientations. Briefly, the metal-surface selection rule states that only vibrations with a component of the dipole moment change perpendicular to the surface will be observed in EEL spectra. In either of the above cases, the O-H bond would be parallel to the surface, and the ν_{OH} stretch would not be observed. Therefore, again the absence of a ν_{OH} stretch does not conclusively indicate O-H bond scission.

The above arguments suggest several possible explanations for the absence of the ν_{OH} stretch in the pyrogallol EEL spectra. Only one explanation favors dehydrogenation, and the latter two suggest no O-H bond scission upon adsorption. Instead, the orientation of the adsorbed species, along with hydrogen bonding between adsorbed molecules,

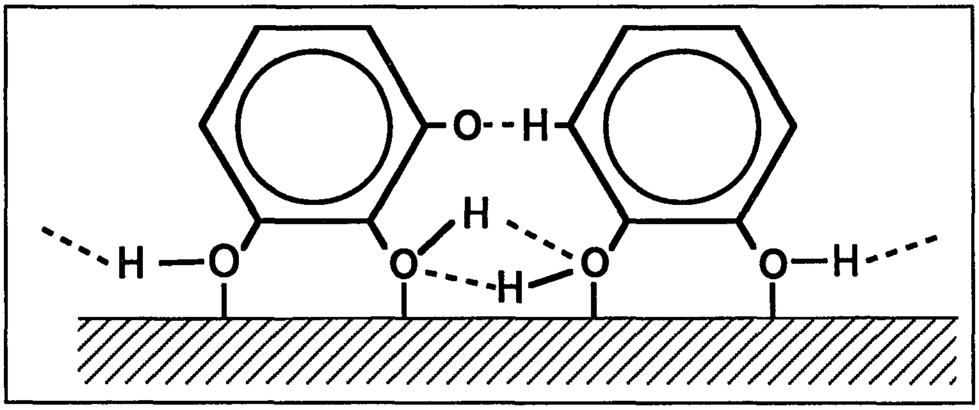

Figure 15. Diagram of hydrogen bonded pyrogallol on Ag(111).

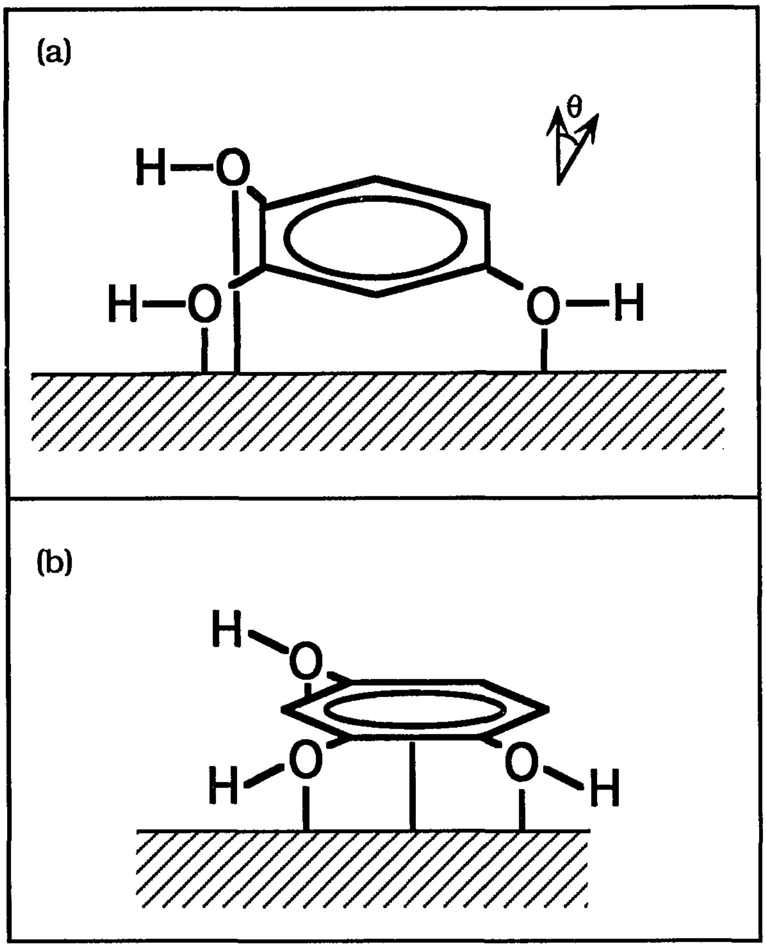

Figure 16. Two possible orientations in which the O-H bond axis lies parallel to the surface.

would cause the ν_{OH} stretch to be essentially absent from the EEL spectra. At this point, dehydrogenation cannot be completely ruled out; however, TDS and isotopic exchange experiments would be necessary for complete proof of O-H bond scission.

4.3. Ring Orientation and Normal Mode Assignment

To determine the molecular orientation of pyrogallol on the surface, we first categorize all the vibrational modes into different point groups representing different geometric orientations. In this case, two point groups are chosen for comparison; the C_{2v} point group represents a perpendicular orientation and the C_s point group represents a parallel molecular orientation. Further, each vibrational mode can be described by a specific symmetry species within each point group, as listed in columns 2 and 3 in Table 1. The observed loss features will either correspond to one, both, or neither of the specific point groups. The point group to which most of the vibrational modes can be assigned describes the molecular orientation of the surface species.

Most of the loss features observed in both the UHV and industrially deposited pyrogallol films can be assigned to vibrational modes in the C_s point group, i.e., the symmetry point group representing a parallel orientation of the pyrogallol molecule. The assignment of this symmetry point group assumes no perturbation from the adsorption site. The peak appearing in the frequency range between 745 and 805 cm^{-1} is assigned to a combination of the ν_4 and ν_{11} vibrational modes of the benzene ring. The ν_4 vibrational mode is associated with puckering of the aromatic ring, and ν_{11} originates from out-of-plane γ_{CH} bending modes. Although the frequency of this peak shifts up with increasing temperature, the frequency shift does not change the assignment of the feature. The peak at 995 cm^{-1} appears only in the UHV deposited films, and is assigned to the ν_5 vibrational mode of the benzene ring which also corresponds to out-of-plane γ_{CH} deformations. Finally, the loss feature appearing at 1340 cm^{-1} is assigned to ν_{20a}, the $\nu_{C\text{-}OH}$ stretching mode. All of these vibrational modes belong to totally symmetric representations of the C_s point group *and* obey the metal-surface selection rule.

According to the above evidence, we might speculate that pyrogallol assumes a parallel orientation on the surface. However, two of the observed loss features would also be consistent with a perpendicular orientation. The feature appearing as a shoulder at 1340 cm^{-1} can also be assigned to the ν_{14} vibrational mode of benzene. This vibrational mode is associated with C-C stretches and belongs to the totally symmetric representation of the C_{2v} point group. Recall the C_{2v} point group represents a perpendicular molecular orientation. Further, the peak appearing in the frequency range between 2900 and 3005 cm^{-1} is assigned to ν_{20b}, the vibrational mode associated with ν_{CH} stretches. This vibrational mode also belongs to the totally symmetric representation of the C_{2v} point group. Thus, some vibrational mode assignments suggest a perpendicular molecular orientation.

Since only one loss feature shows any temperature dependence, based only on the EELS results, we suggest that there exists only one species on the surface. Further, this species adopts a single well-defined molecular orientation, i.e., either perpendicular, tilted, or parallel. As discussed above, most of the assigned vibrational modes belong to the C_s point group (i.e., a parallel orientation); however, ν_{14} can also be assigned to the C_{2v} point group, while ν_{20a} is assigned solely to the C_{2v} point group. The presence and assignment of these features to the C_{2v} point group suggests some tilting of the pyrogallol away from the surface. Figure 17 shows how a inclined orientation might appear on the surface.

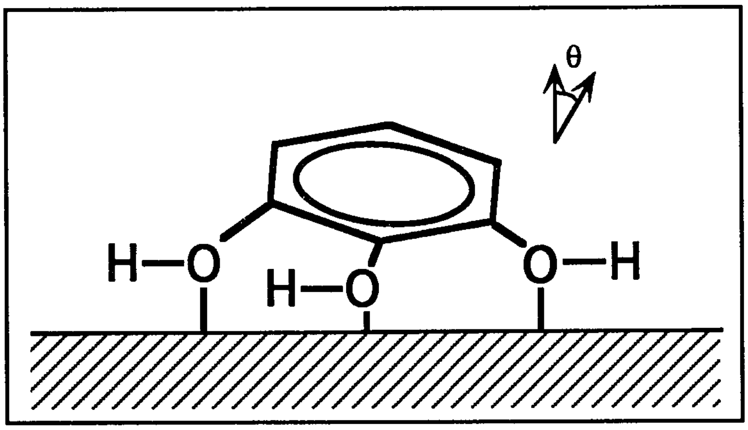

Figure 17. Diagram of pyrogallol in an inclined orientation, at some angle, θ, from the surface normal.

5. CONCLUSIONS

We identify and characterize pyrogallol adsorbed on Ag(111) and on Ag-coated PET films using high resolution EELS. Upon adsorption, the aromatic nature of the pyrogallol molecule is preserved, as evidenced in the EEL spectra. Further, the EELS data cannot unambiguously determine if dehydrogenation occurs upon adsorption; further studies using TDS and isotopic exchange are necessary to determine if O-H bond scission occurs.

The vibrational losses observed in the EEL spectra can be assigned by comparison to normal vibrational modes of the benzene molecule and by comparison with assignments of the simpler hydroxybenzenes studied previously by this author. Upon adsorption, the EELS loss features observed in the spectra for both the UHV deposited films and the industrially deposited films indicate an inclined molecular orientation on the surface.

REFERENCES CITED

1. M. G. Ramsey, G. Rosina, D. Steinmüller, H. H. Graen and F. P. Netzer, Surf. Sci. 232 (1990) 266.
2. Material Safety Data Sheet, Aldrich Chemical Co.
3. J. G. Grasselli and W. M. Ritchey, Atlas of Spectral Data and Physical Constants of Organic Compounds, Second Edition (CRC Press, 1973).
4. E. Pretsch, T. Clerc, J. Seibl and W. Simon, Tables of Spectral Data for Structure Determination of Organic Compounds (Springer-Verlag, Berlin Heidlberg, 1983).
5. G. Varsányi, Assignments For The Vibrational Spectra of Seven Hundred Benzene Derivatives, Volume 1, (John Wiley & Sons, Inc., New York, 1974).
6. F. Lu, G. N. Salaita, L. Laguren-Davidson, D. A. Stern, E. Wellner, D. G. Frank, N. Batina, D. C. Zapien, N. Walton and A. T. Hubbard, Langmuir 4 (1988) 637.
7. G. C. Pimentel and A. L. McClellan, The Hydrogen Bond (Reinhold, New York, 1960).
8. M. V. Thiel, E. D. Becker and G. C. Pimentel, J. Chem. Phys. 27 (1957) 486.
9. J. L. Solomon, R. J. Madix and J. Stöhr, Surf. Sci. 255 (1991) 12.
10. A. K. Myers and J. S. Benziger, Langmuir 5 (1989) 1270.

GENERAL CONCLUSIONS

In this dissertation, we investigate the interaction of a series of hydroxybenzene molecules with the Ag(111) surface in an attempt to model how technologically important phenolic adhesives bond to metal surfaces. The main conclusions that can be drawn are summarized below:

(a) All of the hydroxybenzene molecules studied undergo associative adsorption and molecular desorption, indicating that the molecules retain their aromaticity upon adsorption on the Ag(111) surface.

(b) Evidence of aromaticity of the surface species in the industrially prepared films of pyrogallol on Ag-coated polyester is observed in their vibrational spectra.

(c) Dehydrogenation of the hydroxyl groups upon adsorption is not directly observed in the thermal desorption results of the mono- and di-hydroxybenzene molecules; however, the vibrational spectra suggest possible O-H bond scission. We attribute the apparent O-H bond scission to hydrogen bonding between the adsorbed species or to the parallel orientation of the O-H bond axis with respect to the surface.

(d) The EELS results suggest that not all the hydroxybenzene molecules desorb molecularly below 400 K. Instead, some molecules are irreversibly bound to the surface and undergo decomposition at higher temperatures.

(e) The vibrational losses observed in the EEL spectra are assigned by comparison to the normal vibrational modes of benzene or to the assignment proposed in previous studies of these molecules.

(d) Phenol and catechol are oriented in an inclined position, at some angle θ from the surface normal, upon adsorption at 200 K. By 300 K, the orientation becomes perpendicular to the surface, and by 700 K, the molecules decompose, forming a hydrocarbon residue on the surface..

(e) Resorcinol and hydroquinone are oriented perpendicular to the surface upon adsorption at 200 K. As the temperature is increased, the molecules assume an inclined position, tilted away from the surface normal by some angle θ. Both molecules undergo decomposition by 800 K, leaving a hydrocarbon residue on the surface.

(f) The orientation of pyrogallol appears not to be temperature dependent. The molecule assumes an inclined orientation (i.e., tilted by some angle θ away from the surface normal) upon adsorption around 250 K. As the temperature increases, pyrogallol's orientation remains the same until the molecule decomposes.

These studies are performed in an effort to model how technologically important phenolic resins interact with metal surfaces. Fundamental research on the interaction of hydroxybenzenes with metal surfaces, such as that described here, may potentially improve the related industrially important phenolic resins.

BIBLIOGRAPHY

1. J. Robins, Structural Adhesives: Chemistry and Technology (Plenum Press, New York, 1986).
2. G. Ertl and J. Küppers, Low Energy Electrons and Surface Chemistry, Second Edition (VCH, Weinheim, 1985).
3. D. A. King, Surf. Sci. 47 (1975) 384.
4. G. D. Waddill and L. L. Kesmodel, Surf. Sci. 182 (1987) L248.
5. J. W. Rogers Jr., R. L. Hance and J. M. White, Surf. Sci. 100 (1980) 388.
6. M. D. Crapper, D. P. Woodruff, M. Bader and J. Haase, Surf. Sci. 182 (1987) L241.
7. M. Bader, A. Puschmann and J. Haase, Phys. Rev. B 33 (1986) 7366.
8. M. Bowker and R. J. Madix, Surf. Sci. 116 (1982) 549.
9. M. Bowker and R. J. Madix, Surf. Sci. 95 (1980) 190.
10. K. Christmann and J. E. Demuth, J. Chem. Phys. 76 (1982) 6308.
11. K. Christmann and J. E. Demuth, J. Chem. Phys. 76 (1982) 6318.
12. M. Rebholz, V. Matolini, R. Prins and N. Kruse, Surf. Sci. 251/251 (1991) 1117.
13. J. Hrbek, R. A. dePaola and R. M. Hoffmann, J. Chem. Phys. 81 (1984) 2818.
14. J. E. Demuth and H. Ibach, Chem. Phys. Lett. 60 (1979) 395.
15. F. L. Baudais, A. J. Borschke, J. D. Fedyk and M. J. Dignam, Surf. Sci. 100 (1980) 210.
16. J. Xu, X. Zhang, R. Zenobi, J. Yoshinobu, Z. Xu and J. T. Yates Jr., Surf. Sci. 256 (1991) 288.
17. M. E. Castro and J. M. White, Surf. Sci. 257 (1991) 22.
18. R. L. Brainard and R. J. Madix, Surf. Sci. 214 (1989) 396.

19. J. N. Russell Jr., S. M. Gates and J. T. Yates Jr., Surf. Sci. 163 (1985) 516.

20. Q. Dai and A. J. Gellman, Surf. Sci. 257 (1991) 103.

21. R. Ryberg, Chem. Phys. Lett. 83 (1981) 423.

22. B. A. Sexton, Surf. Sci. 88 (1979) 299.

23. J. L. Solomon and R. J. Madix, J. Phys. Chem. 91 (1987) 6241.

24. J. L. Solomon, R. J. Madix and J. Stöhr, J. Chem. Phys. 89 (1988) 5316.

25. P. Yannoulis, R. Dudde, K. H. Frank and E. E. Koch, Surf. Sci. 189/190 (1987) 519.

26. J. Tabony, J. W. White, J. C. Delachaume and M. Coulon, Surf. Sci. 95 (1980) L282.

27. M. R. Albert and J. T. Yates Jr., The Surface Scientist's Guide to Organometallic Chemistry, First Edition (American Chemical Society, Washington, DC, 1987).

28. A. K. Myers, G. R. Schoofs and J. B. Benziger, J. Phys. Chem. 91 (1987) 2230.

29. J. C. Bertolini and J. Rousseau, Surf. Sci. 89 (1979) 467.

30. J. C. Bertolini, G. Dalmai-Imelik and J. Rousseau, Surf. Sci. 67 (1977) 478.

31. W. Huber, M. Weinelt, P. Zebisch and H.-P. Steinrück, Surf. Sci. 253 (1991) 72.

32. S. Lehwald, H. Ibach and J. E. Demuth, Surf. Sci. 78 (1978) 577.

33. Z. Jing and J. L. Whitten, Surf. Sci. 250 (1991) 147.

34. W. Huber, P. Zebisch, T. Bornemann and H.-P. Steinrück, Surf. Sci. 258 (1991) 16.

35. H. Jobic, J. Tomkinson, J. P. Candy, P. Fouilloux and A. J. Renouprez, Surf. Sci. 95 (1980) 496.

36. H. Jobic and A. Renouprez, Surf. Sci. 111 (1981) 53.

37. T. E. Fischer, S. R. Kelemen and H. P. Bonzel, Surf. Sci. 64 (1977) 157.

38. M. Surman, S. R. Bare, P. Hofmann and D. A. King, Surf. Sci. 126 (1983) 349.

39. M. Surman, S. R. Bare, P. Hofmann and D. A. King, Surf. Sci. 179 (1987) 243.

40. D. Haaland, Surf. Sci. 102 (1981) 405.

41. G. L. Nyberg and N. V. Richardson, Surf. Sci. 85 (1979) 335.

42. G. D. Waddill and L. L. Kesmodel, Phys. Rev. B 31 (1985) 4940.

43. P. Hofmann, K. Horn and A. M. Bradshaw, Surf. Sci. 105 (1981) L260.

44. J. F. M. Aarts and N. R. M. Sassen, Surf. Sci. 214 (1989) 257.

45. H. Hoffmann, F. Zaera, R. M. Ormerod, R. M. Lambert, L. P. Wang and W. T. Tysoe, Surf. Sci. 232 (1990) 259.

46. F. P. Netzer and J. U. Mack, J. Chem. Phys. 79 (1983) 1017.

47. V. H. Grassian and E. L. Muetterties, J. Phys. Chem. 91 (1987) 389.

48. F. P. Netzer, G. Rangelov, G. Rosina, H. B. Saalfeld, M. Neumann and D. R. Lloyd, Phys. Rev. B 37 (1988) 10399.

49. H. Ohtani, M. A. V. Hove and G. A. Somorjai, J. Phys. Chem. 92 (1988) 3974.

50. F. P. Netzer, E. Bertel and J. A. D. Matthew, Surf. Sci. 92 (1980) 43.

51. A. C. Liu and C. M. Friend, J. Chem. Phys. 89 (1988) 4396.

52. B. E. Koel, J. E. Crowell, C. M. Mate and G. A. Somorjai, J. Phys. Chem. 88 (1984) 1988.

53. F. P. Netzer, H. H. Graen, H. Kuhlenbeck and M. Neumann, Chem. Phys. Lett. 133 (1987) 49.

54. P. Avouris and J. E. Demuth, J. Chem. Phys. 75 (1981) 4783.

55. K. H. Frank, P. Yannoulis, R. Dudde and E. E. Koch, J. Chem. Phys. 89 (1988) 7569.

56. P. Jakob and D. Menzel, Surf. Sci. 201 (1988) 503.

57. P. Gao and M. J. Weaver, J. Phys. Chem. 89 (1985) 5040.

58. F. P. Netzer, A. Goldmann, G. Rosina and E. Bertel, Surf. Sci. 204 (1988) 387.

59. G. R. Schoofs and J. B. Benziger, Surf. Sci. 192 (1987) 373.

60. G. R. Schoofs and J. B. Benziger, J. Phys. Chem. 92 (1988) 741.

61. B. J. Bandy, D. R. Lloyd and N. V. Richardson, Surf. Sci. 89 (1979) 344.

62. D. Harradine and A. Campion, J. Vac. Technol. A 4 (1986) 1467.

63. P. Avouris, N. J. DiNardo and J. E. Demuth, J. Chem. Phys. 80 (1984) 491.

64. N. J. DiNardo, P. Avouris and J. E. Demuth, J. Chem. Phys. 81 (1984) 2169.

65. G. Mizutani and S. Ushioda, J. Chem. Phys. 91 (1989) 598.

66. J. E. Demuth, K. Christmann and P. N. Sanda, Chem. Phys. Lett. 76 (1980) 201.

67. J. E. Demuth, P. Avouris and P. N. Sanda, J. Vac. Sci. Technol. 20 (1982) 588.

68. X. Jiang and A. Campion, Chem. Phys. Lett. 140 (1987) 95.

69. F. P. Netzer, G. Rangelov, G. Rosina and H. B. Saalfeld, J. Chem. Phys. 89 (1988) 3331.

70. F. P. Netzer and J. U. Mack, Chem. Phys. Lett. 95 (1983) 492.

71. M. Connolly, J. Sommers, M. E. Bridge and D. R. Lloyd, Surf. Sci. 185 (1987) 559.

72. V. H. Grassian and E. L. Muetterties, J. Phys. Chem. 90 (1986) 5900.

73. J. U. Mack, E. Bertel and F. P. Netzer, Surf. Sci. 159 (1985) 265.

74. H. Lüth, G. W. Rubloff and W. D. Grobman, Surf. Sci. 74 (1978) 365.

75. Y. Song, P. Gardner, H. Conrad and A. M. Bradshaw, Surf. Sci. Lett. 248 (1991) L279.

76. J. T. Roberts and C. M. Friend, J. Chem. Phys. 88 (1988) 7172.

77. C. M. Friend in: Adsorption Structure of Organic Molecules on Mo(110), Vol. 17 (Springer-Verlag Berlin, Heidleberg, 1989) p. 67.

78. Y. Takata, T. Yokoyama, S. Yagi, N. Happo, H. Sato, K. Seki, T. Ohta, Y. Itajima and H. Kuroda, Surf. Sci. 259 (1991) 266.

79. D. A. Stern, E. Wellner, G. N. Saliata, L. Laguren-Davidson, F. Lu, N. Batina, D. G. Frank, D. C. Zapien, N. Walton and A. T. Hubbard, J. Am. Chem. Soc. 110 (1988) 4885.

80. J. Y. Gui, D. A. Stern, D. G. Frank, F. Lu, D. C. Zapien and A. T. Hubbard, Langmuir 7 (1991) 955.

81. J. G. Serafin and C. M. Friend, Surf. Sci. 209 (1989) L163.

82. J. G. Serafin and C. M. Friend, J. Am. Chem. Soc. 111 (1989) 4233.

83. A. C. Liu, C. M. Friend and J. Stöhr, Surf. Sci. Lett. 236 (1990) L349.

84. F. Lu, G. N. Salaita, L. Laguren-Davidson, D. A.Stern, E. Wellner, D. G. Frank, N. Batina, D. C. Zapien, N. Walton and A. T. Hubbard, Langmuir 4 (1988) 637.

85. B. E. Kahn, S. A. Chaffins, J. Y. Gui, F. Lu, D. A. Stern and A. T. Hubbard, Chem. Phys. 141 (1990) 21.

86. M. P. Soriaga, J. H. White and A. T. Hubbard, J. Phys. Chem. 87 (1983) 3048.

87. J. L. Solomon, R. J. Madix and J. Stöhr, Surf. Sci. 255 (1991) 12.

88. A. K. Myers and J. S. Benziger, Langmuir 5 (1989) 1270.

89. D. Steinmüller, M. G. Ramsey and F. P. Netzer, Surf. Sci. 271 (1992) 567.

90. M. G. Ramsey, G. Rosina, D. Steinmüller, H. H. Graen and F. P. Netzer, Surf. Sci. 232 (1990) 266.

91. N. Batina, D. G. Frank, J. Y. Gui, B. E. Kahn, C.-H. Lin, F. Lu, J. W. McCargar, G. N. Salaita, D. Stern, D. C. Zapien and A. T. Hubbard, Electrochim. Acta 34 (1989) 1031.

92. V. K. F. Chia, M. P. Soriaga and A. T. Hubbard, J. Phys. Chem. 91 (1987) 78.

93. G. Varsányi, Assignments For The Vibrational Spectra of Seven Hundred Benzene Derivatives, Volume 1, (John Wiley & Sons, Inc., New York, 1974).

94. E. B. Wilson, Phys. Rev. 45 (1934) 706.

95. N. Sheppard and J. Erkelens, Appl. Spectrosc. 38 (1984) 471.

96. N. V. Richardson and N. Sheppard in: Normal Modes at Surfaces, Vol. 1 (Plenum Press, New York, 1987) p. 1.

97. F. A. Cotton, Chemical Applications of Group Theory, Second Edition (John Wiley & Sons, Inc., New York, 1971).

98. P. W. Palmberg, G. E. Riach, R. E. Weber and N. C. MacDonald, Handbook of Auger Electron Spectroscopy (Physical Electronic Industries, Inc., Edina, 1972).

99. R. G. Musket, W. McLean, C. A. Colenares, D. M. Makowiecki and W. J. Siekhaus, Appl. Surf. Sci. 10 (1982) 143.

100. 3M Company, St. Paul, MN.

101. H. Herz, H. Conrad and J. Küppers, J. Phys. E 12 (1979) 369.

102. Macallister EEL spectrometer.

APPENDIX A:

A COMPUTER PROGRAM FOR THERMAL DESORPTION EXPERIMENTS

1. INTRODUCTION

Thermal desorption spectroscopy (TDS) is a technique widely used in surface analysis. In the TDS experiment, an adsorbate covered crystal is heated linearly while monitoring the gas phase of the vacuum chamber with a mass spectrometer. As the crystal temperature increases the adsorbate may desorb, decompose, decompose and recombine to desorb at a higher temperature, or react with a second adsorbate and desorb. A typical thermal desorption spectrum is shown elsewhere in this text (Part 2, Figure 5), and is a measure of the partial pressure of a gas with a specific mass as a function of time or crystal temperature.

The TDS experiment becomes long and tedious if monitoring only one mass at a time; however, computer control allows essentially "simultaneous" examination of several in one experiment. In this way, a very complex reaction, with several desorption products, can be studied in one experiment rather than repeating the experiment for each possible reaction product.

As well as expediating the TDS experiment, computer controlled TDS has several other advantages. For example, data may be stored permanently on floppy disks, thus minimizing the possibilty of damage or loss. Second, the data may be manipulated and plotted more easily, conveniently, and repeatedly using a computer plotting routine. Finally, mathematical calculations can be performed more precisely and reproducibly from stored data as opposed to hand measurements and calculations.

The remainder of this appendix describes a computer program written for an IBM compatible Electra computer to acquire, plot, and mathematically manipulate thermal desorption data.

2. EQUIPMENT

The ELECTRA personal computer is interfaced to a UTI 100C quadrupole mass spectrometer and a commercial temperature controller [1] via a Data Translation DT2821 interface board. The DT2821 board has eight differential analog-to-digital (A/D) input channels and two digital-to-analog (D/A) output channels. Further, 16 I/O ports are available for writing or reading data. The computer also supports a Hewlett-Packard 7470A two pen plotter, a Hewlett-Packard Laser-Jet printer and a STAR Micronics NX-1000 dot matrix printer. Figure 1 schematically illustrates the interface.

2.1. Mass Control

Mass control is achieved through D/A channel 0 on the DT2821 board. The board is configured to provide 0 to +10 V to the "EXTERNAL PROGRAM" connector on the rear panel of the mass spectrometer. This voltage range corresponds to 0 to 300 AMU, and is internally scaled by the mass spectrometer electronics and applied to the quadrupole rods. Thus, mass is represented in three ways: atomic mass units (0 to 300 AMUs), a voltage (0 to 10 V) proportional to that applied to the mass spectrometer, or a DAC output (0 to 4095, binary notation). The computer accepts a binary DAC value, converts this value to the corresponding voltage, and sends the voltage to the mass spectrometer controller. An external program "CALIBRAT" is used to determine the DAC output corresponding to individual masses.

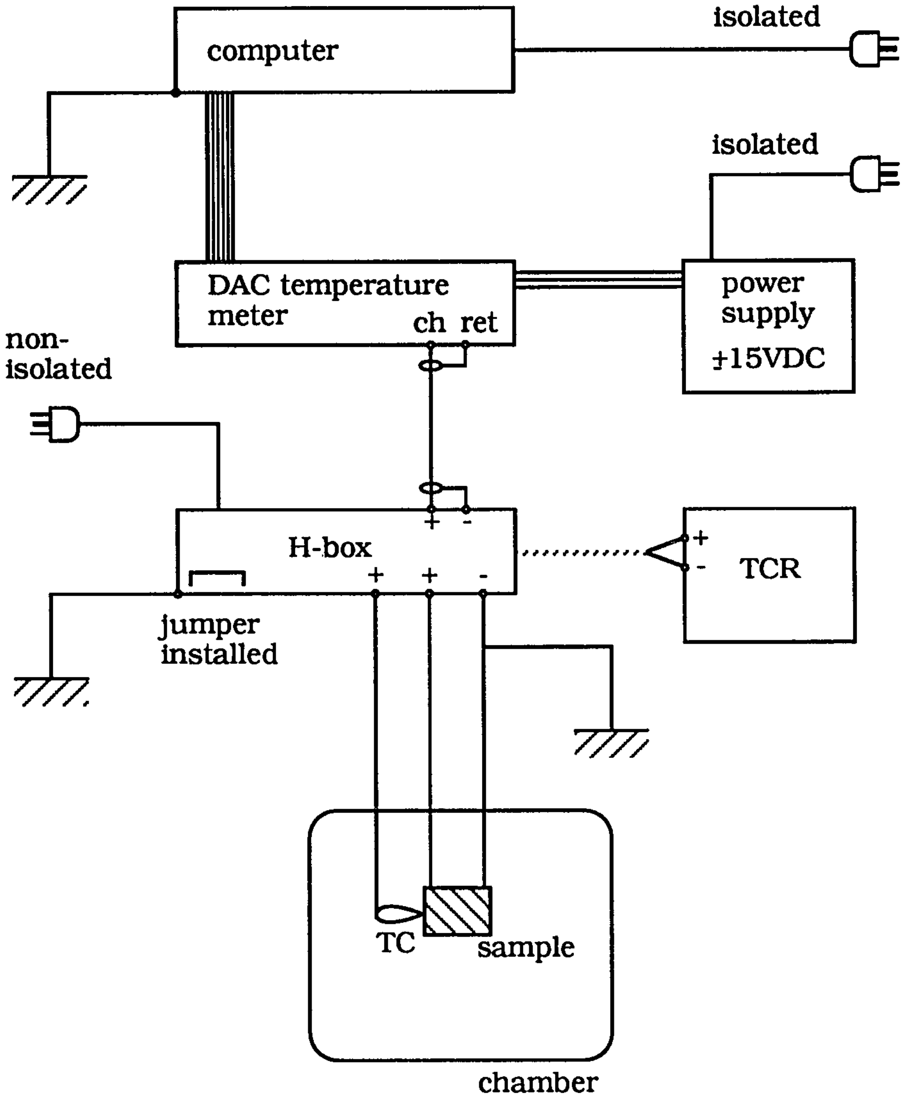

Figure 1. Schematic diagram of the Electra computer interface and peripheral equipment.

The CALIBRAT program is used to determine the relationship between DAC output and mass for a particular mass spectrometer. The operator enters a DAC value between 0 and 4095 and the computer sets the mass spectrometer to the corresponding AMU value. An approximate DAC value for a specific AMU can be calculated as follows

$$\text{DACVAL} = \text{AMU} \times (4095/300)$$

The computer then reads the signal intensity for the entered DAC value and the preceding seven DAC values and displays all eight DAC vaslues and signal intensities on the screen In this manner, the operator actually sees which DAC value produces the maximum signal intensity and records this value. When the DAC values for all masses are determined and recorded, the operator enters these values into the AMU table on the menu screen in the HTDS program. This calibration procedure need only be repeated weekly.

2.2. Mass Intensity and Temperature

The mass signal intensity and temperature are measured via two A/D channels on the DT2821 interface board. The A/D channels are read differentially, that is, the amplifier sees only the "difference" in voltage between the high end and return side of the input channel. Differential operation connections have the advantage of reducing the common mode noise (i.e., voltage noise common to both sides of the analog input). The A/D channels are configured to accept bipolar voltages between -10 and +10 V. The computer reads mass intensity on A/D channel 0 from the connector labeled "SIGNAL OUT" on the rear panel of the mass spectrometer controller.

An independent commercial temperature controller [1] regulates the sample heating rate. The computer reads the temperature on A/D channel 5 from the "DVM" connector on the rear panel of the temperature controller. The thermocouple output from "DVM" is internally amplified 100 times within the temperature controller, and this amplification factor is accounted for during the voltage (mV) to temperature (K) within the HTDS program.

The temperature controller is computer regulated to start, stop, and reset the heating ramp. This control is accomplished using I/O Port 0 on the DT2821 interface board in conjuntion with an external circuit comprised of a HEX inverter, three reed relay IC chips and a voltage regulator. A schematic drawing of this circuit is depicted in Figure 2. Reverse logic is used in this command sequence, thus a LO signal sent to the appropriate I/O bit activates the relay. Specifically, bits 5, 6 and 7 of I/O Port 0 correspond to the start, stop and reset functions of the temperature controller, respectively. Programming the I/O ports is described in detail in the DT2821 user's manual, beginning on page 7-54, and the sequence is also documented extensively within the HTDS program.

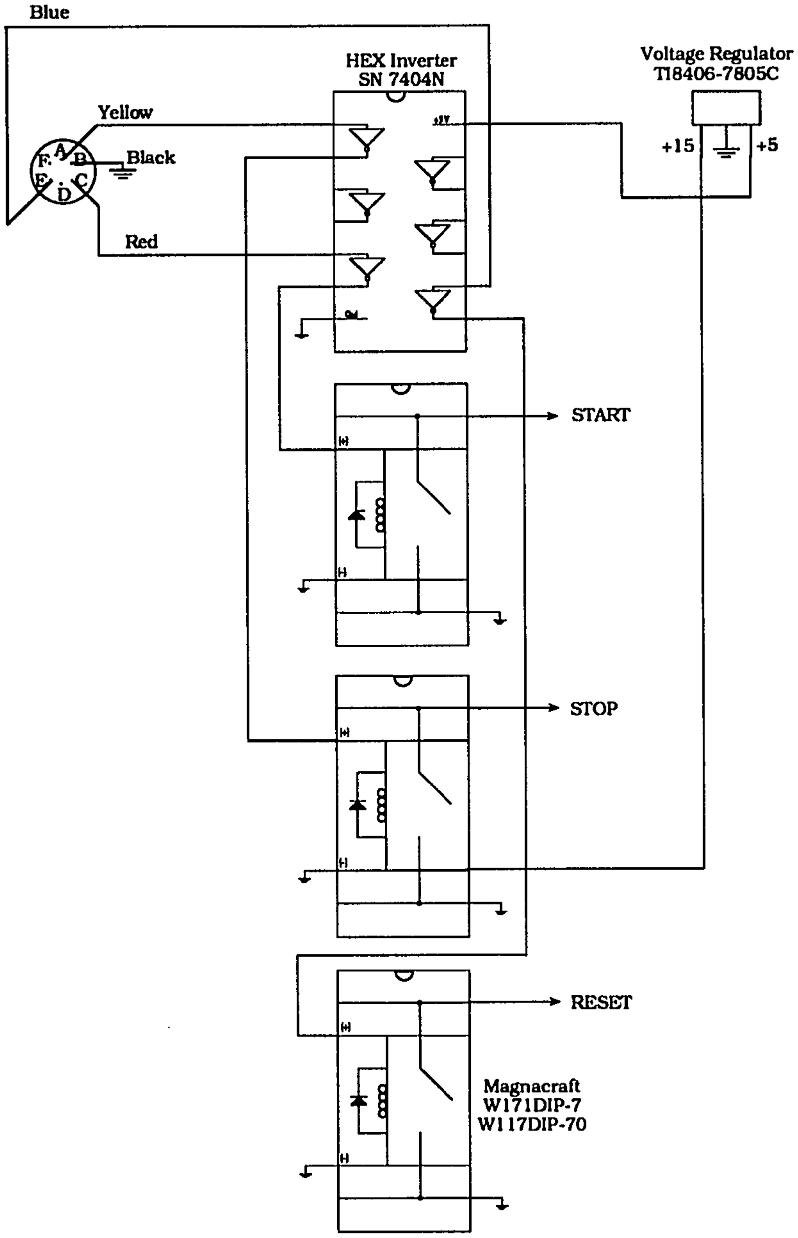

Figure 2. Schematic representation of the relay circuit for controlling the temperature controller.

3. ELECTRA TDS PROGRAM

3.1. Program Overview

The Electra TDS computer program is written in Fortran using the "top-down" programming style, i.e., extensive use of subroutines. The subroutines are listed in Table 1 along with a brief statement of each subroutine's purpose and location within the program. The subroutines are divided into two categories, minor and major. The minor subroutines are usually short and called upon often by several other routines. In general, these subroutines are used for conversion between integer and character values (INTCHAR, CHARINT, etc.) or to change various parameters on the menu display (AMUP, COP, OFFP, etc.). Major subroutines are generally longer and comprise the backbone of the program. Some of these subroutines are used to acquire data (MSREAD), store or load data to or from floppy disks (LOAD or STORE), or plot data to the screen or the Hewlett-Packard plotter (K-PLOT, T-PLOT, R-PLOT, or D-PLOT). The remainder of this section is devoted to describing the HTDS program.

3.2. Menu

The menu screen that appears when the operator executes the HTDS program is shown in Figure 3. The message "ENTER THE FIRST TWO LETTERS OF YOUR CHOICE TO CHANGE:" is displayed at the bottom of the screen.

Filename	Subroutine / Function	Purpose
CONVERT	FXR,FYR	Converts a real% to an X- or Y-graphics unit.
	FXTR,FYTR	Converts an integer% to an X- or Y-graphics unit.
	INTCHAR	Converts an integer to a character*3.
	INTCHAR4	Converts and integer to a character*4.
	RCHAR5	Converts a real (5.2) to a character*5.
	CHARINT4	Converts a character*4 to an integer (I5).
HERZTDS	HTDS	Executable program.
INOUT	STORE	Stores datafile on a floppy disk.
	LOAD	Loads datafile into HTDS.
	PRINT	Prints datafile to the chosen printer.
MENU	FNAMEP	Accepts & displays the filename, device, & extension on the menu screen.
	DATEP	Accepts & displays the date on the menue screen.
	MENU	Arranges the options list on the menu screen.

Table 1. Subroutines used in the thermal desorption program, along with the location and purpose of each.

Filename	Subroutines/ Function	Purpose
MENU	AMUP	Accepts & displays the AMU table information (AMU, DACVAL, and GAIN) on the menu screen.
	COP	Accepts & displays 4 comment lines on the menu screen.
	MSGAINP	Accepts & displays the UTI gain, set externally, to the menu screen.
	OFFP	Accepts & displays the Y-offset value for the current data to the menu screen.
	YSCP	Accepts & displays the Y-scale multiplier for the current data to the menu screen.
	OPRARP	Accepts & displays the operator'e name to the menu screen.
	NOAVGP	Accepts & displays the number of times the signal should be sampled during one acquisition loop to the menu screen.
	SLOPEP	Accepts & displays the heating ramp slope to the menu screen.
	ITEMPP	Accepts & displays the initial temperature to the menu screen.
	FTEMPP	Accepts & displays the end temperature to the menu screen.
	NMASSP	Accepts & displays the number of masses monitored to the menu screen.

Filename	Subroutine/ Function	Purpose
MENU	SHOW	Accepts & displays the number of masses monitored to the menu screen.
MISC	ASZRO	Adds or removes an ASCII zero from the end of a string.
	ERASE	Clears the screen.
	ABSCSR	Positions the choices on the menu screen.
	VIDATR	Sets the video attributes of the screen.
	MESSON	Prints a blinking message on the screen.
	MESSOFF	Shuts off a blinking message on the screen.
	POSDATA	Corrects two's complement errors.
	WAIT	Wastes time.
PLOT	M2	Plots the data to various devices, uses the Graphics Development Toolkit.
	AREACALC	Calculates the peak area.

Filename	Subroutine/ Function	Purpose
TDSEXP	TPDRUN	Performs the actual TDS experiment.
	BRDINIT	Initializes the DT2821 board.
	READY	Waits for the multiplexer to settle.
	ADCONV	Performs a single analog-to-digital conversion.
	DACOUT	Outputs values to DAC0, DAC1, or both DACs.
	TEMPREAD	Reads the current temperature of the sample from the temperature controller.
	TCHANSET	Loads the CHLCSR register with the number of channels employed.
	MSREAD	Reads the mass-spec signal for a given AMU value.
	MCHANSET	Loads the CHLCSR register with the number of channels employed.

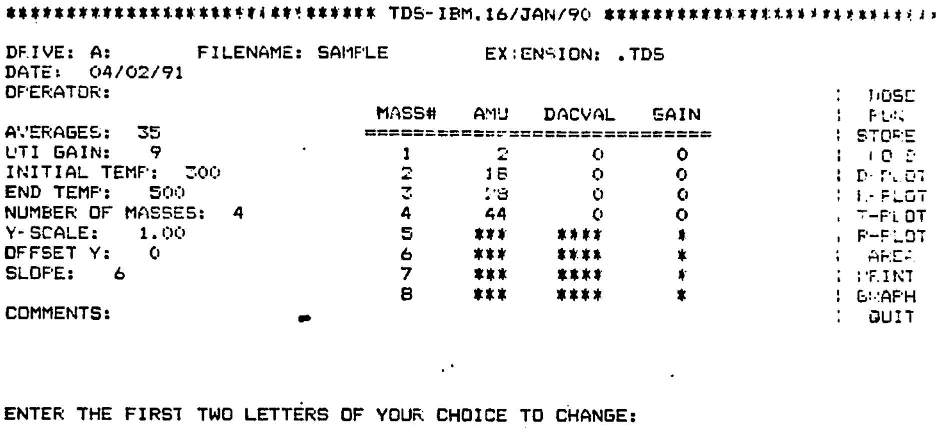

```
************************************ TDS-IBM.16/JAN/90 ********************************

DRIVE: A:        FILENAME: SAMPLE        EXTENSION: .TDS
DATE:  04/02/91
OPERATOR:                                                                   :  DOSE
                                   MASS#   AMU   DACVAL   GAIN              :  RUN
AVERAGES:  35                      ============================             : STORE
UTI GAIN:   9                        1       2      0       0               :  LOAD
INITIAL TEMP:  300                   2      18      0       0               : D-PLOT
END TEMP:   500                      3      28      0       0               : I-PLOT
NUMBER OF MASSES:  4                 4      44      0       0               , T-PLOT
Y-SCALE:   1.00                      5     ***    ****      *               , P-PLOT
OFFSET Y:   0                        6     ***    ****      *               :  AREA
SLOPE:   6                           7     ***    ****      *               : PRINT
                                     8     ***    ****      *               : GRAPH
COMMENTS:                                                                   :  QUIT


ENTER THE FIRST TWO LETTERS OF YOUR CHOICE TO CHANGE:
```

Figure 3. Thermal desorption program's main menu. The menu displays important documentation about the datafile.

To change a parameter, the operator must type the first two letters of the parameter choice, followed by a carriage return, <RET>. If the letters entered are not capitalized, the blinking message, "ACTIVATE CAPS-LOCK KEY AND RETRY COMMAND", will appear on the screen. When capital letters are used, a prompt is displayed for that parameter and the operator enters the new value, followed by <RET>. The computer updates the menu screen and again displays the prompt "ENTER THE FIRST TWO LETTERS OF YOUR CHOICE TO CHANGE:".

For example, to change the filename of a datafile, the operator types FI. The computer will then prompt "ENTER FILENAME", and the operator types the new filename. The computer accepts the information and updates the menu screen by calling subroutine FILENAMEP in file MENUB.FOR.

The menu screen is divided into three sections: a parameter list, the AMU table, and an option list. The parameter list includes DRIVE, FILENAME, EXT, OPERATOR, AVERAGES, UTI GAIN, INITIAL TEMP, END TEMP, NUMBER OF MASSES, Y-SCALE, OFFSET Y, SLOPE, and COMMENTS. All parameters can be changed in the manner described above. The location of and subroutine corresponding to each parameter is listed in Table 1. Several of the parameter functions are briefly described below.

DRIVE refers to the drive where the datafile can be found or will be stored. The default drive is A, and the data is stored on or retrieved from a floppy disk.

DATE refers to the date on which the data is acquired. The date is retrieved from the computer's clock using subroutine GDATE (get date), an MEF No-Limit FORTRAN subroutine. The date may be changed in the same manner as any other parameter.

AVERAGES refers to the number of times (INOAVG) the signal is sampled for each AMU in one cycle. Thus, the computer will sample the signal of one AMU for INOAVG number of times, calculate the average value, and return this average value to the program. The default AVERAGES value is 35.

UTI GAIN refers to the mass spectrometer electrometer gain. The electrometer gain is not computer controlled, but is used to calculate peak areas. The correct gain should be used in these calculations to accurately compare experiments. Internally, the DT2821 interface board amplifies the incoming signal by preselected factors of 8, 4, 2, or 1. Thus, approximately one order of magnitude of computer controlled gain is available. Selecting the internal gain is controlled in subroutine AMUP when the AMU table is created and will be discussed later in this text.

The INITIAL TEMP and END TEMP (K) are read directly from the temperature controller as a voltage, converted to K, and displayed on the updated menu screen upon completion of an experiment. The INITIAL TEMP default value of 300 K is essentially meaningless, so the operator need not enter or change this parameter. The END TEMP (K), however, is crucial to the TDS experiment since data acquisition terminates when the sample temperature reaches the input final temperature. The default END TEMP value is 500 K.

NUMBER OF MASSES refers to the number of masses studied in one experiment. The default value is 4 and must be changed if less than four masses are studied since the computer will cycle through four AMU voltages even if only two values are entered in the AMU table. When a new NUMBER OF MASSES value (NMASS) is entered, the AMU table is updated to display the appropriate number, denoting the remaining table entries as blank (***). The maximum number of masses that can be examined in one experiment is eight. The arrangement of the AMU table will be discussed later in this text.

Y-SCALE and OFFSET Y refer to the scale multiplier and position of the plotted data on the screen or plotter. For example, a Y-SCALE value of 2 doubles the amplitude of the plotted trace, and an OFFSET Y value of 3 moves the trace up three integral units on the plot.

SLOPE refers to the heating rate slope set on the temperature controller. The values for SLOPE may be 1 through 10, corresponding to heating rates of 0.1, 0.2, 0.5 1, 2, 5, 10, 20, 50, and 100 mV/min, respectively. This value is not computer controlled, but used strictly for documentation purposes when comparing experiments.

COMMENTS refers to any documentation the operator chooses to enter. There are four COMMENTS lines available for text describing the experiment. For example, the operator may describe the background pressure, exposure, sample temperature, or any other information pertinent to the experiment. To access these comment lines the operator may either type C, CO, or C1, C2, C3, or C4 corresponding to an individual comment line.

The AMU table comprises the second section of the menu screen. When the menu screen is displayed, four masses (2, 18, 28, and 44) are entered in the table. No DACVALs or GAINs for these masses are displayed however. To change a table entry, the operator must choose a MASS # (1-8). The prompt, "ENTER AMU#:" appears and the operator must enter some AMU (0-300). The computer will then prompt, "ENTER DACVAL:" and the operator enters a numerical value (0-4095) corresponding to the input AMU value. The DACVALs are obtained using an external program named CALIBRAT, and must be determined prior to initiating the TDS experiment. Finally, the prompt, "ENTER GAIN (0-3):" appears, and the operator sets the internal DT2821 board gain as 0, 1, 2, or 3, corresponding to multiplication factors of x1, x2, x4, or x8, respectively. The AMU table is updated after each complete entry.

The final portion of the menu screen contains the list of program options, including DOSE, RUN, STORE, LOAD, D-PLOT, K-PLOT, T-PLOT, R-PLOT, AREA, PRINT, GRAPH, and QUIT (see Figure 3). The remainder of this section describes these options, and Table 1 lists the location of the subroutines corresponding to each option in program HTDS.

3.3. Dose

The DOSE option allows the operator to run adsorption experiments and monitor the signal intensities as the crystal is exposed to the adsorbate of interest. In these experiments the sample temperature is constant, and the computer monitors the signal intensities for a preset length of time. As the program is written, the cycle time is two minutes (or JCOUNT3 = 2200 counts on the internal computer clock). This time length may be changed by altering the program software.

3.4. Run

Selecting the RUN option begins the data acquisition routine. When RUN is selected, the subroutine TPDRUN is called and the computer prompts "ARE THE TCR AND UTI TURNED? (Y/N)". At this time, the operator can make a final check of the electronics before actually starting the experiment. If N is chosen, the program returns to the menu screen. If Y is selected, the temperature ramp is started and data acquisition begins. The first step is to initialize the A/D circuits on the DT2821 interface board. Next, the blinking message, "TDS EXPERIMENT IN PROGRESS!" is displayed on the screen. Also, the initial clock count is read from the computer's internal clock using TIMASM, a MEF No-Limit FORTRAN subroutine.

Next, the program reads the initial temperature. Using the subroutine TEMPREAD the thermocouple voltage is read, converted from an analog voltage to a digital bit value (subroutine ADCONV), and averaged over INOAVG number of times. This value (TEMP) is converted back to a millivolt value, and finally converted to a Kelvin temperature. One conversion equation is used over the entire temperature range. This equation was derived empirically by fitting chromel-alumel thermocouple output and temperature data to a third degree polynomial. If tungstenrhenium thermocouple wires are used, three fifth degree polynomial conversion equations are used, and the program software must be altered.

The signal intensity for each AMU is now acuired by calling subroutine MSREAD. The point count (SCNT) is set at 1 for the first data point. When the mass spectrometer is set to a voltage corresponding to an individual AMU, the subroutine WAIT is called 20 times to allow sufficient time for the mass spectrometer to settle on this voltage. The signal intensity at this voltage is sampled INOAVG number of times, internally converted from an analog signal to a digital value, and the average value (MSOUT) is returned to TPDRUN where it is stored in an array, W2. This MSREAD loop is repeated for each input AMU, and when all the signal intensities are acquired, the SCNT is increased by 1. The sample temperature is now compared with the input end temperature (FTEMP). If the current temperature is less than FTEMP, the TEMPREAD subroutine is called and the entire data acquisition loop is repeated.

When the sample reaches a temperature greater than FTEMP, the final clock count is read by calling TIMASM again. The elapsed time is calculated, converted to milliseconds, and divided by SCNT to obtain time intervals which are stored in the TIME2 array. At this time the heating ramp is terminated.

3.5. Store and Load

The STORE and LOAD options allow storage to and retrieval from floppy disks. When STORE is selected, subroutine STORE is called from the INOUTB file. The computer prompts, "IS THERE A DISK IN DRIVE A? (Y/N)", allowing the operator to check the disk drive. If 'N' is entered, the same prompt is repeated. If 'Y' is entered, the disk drive is checked for possible errors using CHKDRV, a MEF No-Limit FORTRAN subroutine. Three possible blinking messages may appear depending on the nature of the error, if any is found, including: "UNKNOWN STORAGE DEVICE ERROR--TRY AGAIN", "DRIVE NOT READY", or "UNFORMATTED DISK". Next, DISKINF, another MEF No-Limit FORTRAN subroutine, is called to check if there is enough disk space for the current datafile. If not enough space is found, the message "NOT ENOUGH SPACE ON DISK" will blink on the screen. If the current filename has been used previously on the disk, the computer will prompt "THE FILE ALREADY EXISTS--OVERWRITE?? (Y/N)". If the answer is 'N' the program returns to the menu screen, but if 'Y', the data is stored under the current filename while the message "STORING" blinks on the screen. If some writing error occurs, the message "WRITING ERROR !!!!!!" blinks on the screen. In the above sequence, the data is stored to drive A with the TDS default three letter extension. If no writing errors were detected, the "STORING" message quits blinking and the program returns to the menu screen.

When LOAD is selected, subroutine LOAD is called, and the chosen datafile is retrieved from the floppy disk into the HTDS program. As in STORE, the CHKDRV subroutine is used to check for drive errors. If no errors are found, the datafile is loaded into HTDS while the blinking message "LOADING" appears. If an error occurs while opening a file, "ERROR OPENING FILE" blinks and if an error reading the file occurs, the message line will blink "ERROR READING FILE". If no errors are detected the program returns to the menu screen after the "LOADING" message quits blinking.

3.6. *-Plot

D-PLOT, K-PLOT, T- PLOT, and R-PLOT allow the datafile to be plotted, in various formats, to the screen or the plotter. The plotting options are chosen by the operator. D-PLOT allows the adsorption data to be plotted vs. time, K-PLOT and T-PLOT allow plotting of signal intensity vs. temperature or time, respectively, and R-PLOT allows the temperature ramp (temperature vs. time) to be plotted. After selecting a plotting option, flags are set in the program to establish specific plotting formats, and then a generic plotting initialization is used for all plots. Once initialized, subroutine M2 is called for the actual plotting.

The flags used in this routine include TFLAG, AFLAG, DFLAG, and RFLAG. TFLAG is the time or temperature flag, and a value of 1 selects plotting the signal intensity vs. time, whereas a value of 0 means the signal intensity is plotted vs. temperature. AFLAG is the area flag, and a value of 1 calls the AREACALC subroutine. If DFLAG, the data only flag, is set to 1, only the data is plotted, with no documentation. Finally, RFLAG is the temperature ramp flag, and a value of 1 means temperature is plotted vs. time.

Once the plotting format is chosen and the flags are set, the plotting initialization begins. The screen is set up and when the prompt, "ENTER MASS# (1-(NMASS))", appears, the operator responds by entering a mass number between 1 and NMASS. Next, the computer prompts, "WHAT DEVICE (QUIT=0, SCREEN=1, PRINTER=2, PLOTTER=3)?:" and the operator selects to which device the data will be plotted. If quit (0) is chosen, the program returns to the menu screen. If the printer or the plotter is chosen (2 or 3), the operator is asked if everything (i.e., documentation, axes, scale, etc.) or only the data should be plotted as the prompt, "DATA ONLY (Y/N)?:", appears.

Next, the plotting device is set up, and the program proceeds by asking the operator to make several choices regarding the plots. For example, when the plotter is used, a pen color (PICO, corresponding to pen position) must be selected in response to the prompt, "PEN COLOR (1 OR 2):". Another prompt asks whether the X-axis should be automatically or manually scaled, "AUTO OR MANUAL (A/M)? [0=QUIT]". If quit is chosen, plotting is terminated and the menu screen is displayed. If manual scaling is chosen, the operator is prompted to enter the initial and final times (or temperatures), and if these values are not within the data range acquired, the prompts reappear. These prompts include, "ENTER THE INITIAL TIME (in seconds):" or "ENTER THE INITIAL TEMPERATURE:" along with "ENTER THE FINAL TIME (in seconds):" or "ENTER THE FINAL TEMPERATURE:". If automatic scaling is chosen, a flag is set to 1 (AUTOFLAG=1), and the scaling range includes the entire data range acquired.

At this point the generic plotting initialization is complete and the M2 plotting subroutine is called. M2 uses GRAPHICS DEVELOPMENT

TOOLKIT routines to open the workstations and plot the TDS data on the screen, plotter, or printer. All the setup values for these workstations have been established in the generic plotting initialization section. This M2 subroutine arranges the information to be plotted into three regions: a plotting region, a documentation box, and a comment area. The largest of these is the plotting region which is enclosed in a box. Within the plotting region will be the data trace, the X- and Y-axes, as well as some AMU information. The documentation region is located on the upper left side of the plot and includes the following information: filename, date, operator, slope, and an AMU/GAIN table. This information is passed from HTDS, and any integer values must be converted to character strings before they can be displayed on the plots. The final region, the comment area, is enclosed in a box and it is here that the four comment lines, if any, will be displayed. If plotting to the screen, this comment region is not displayed.

The data is now plotted by two-point line segments. That is, two consecutive points are plotted and connected by a line, taking into account any Y-scale multiplication factors or offset values. This sequence is repeated until all the data are plotted. The X-axis is then drawn across the bottom of the plotting region by establishing the range domain and the minor and major intervals, denoted by small or large ticmarks, respectively. The domain is determined from the information provided in the plotting initialization routine regarding automatic or manual scaling. The time or temperature labels are centered under the major interval ticmarks. The Y-axis is now plotted with small ticmarks and labels. Essentially, the Y-axis divides the plotting region vertically into 10 integral units.

Finally, if displaying to the screen, a prompt will appear asking if another mass is to be plotted, "ANOTHER PLOT? (ENTER 0-8 [0=QUIT])". If so, the mass number of the AMU to be plotted is entered. If the value entered is outside the range (0-8), the prompt is repeated. If the operator wishes to quit, 0 is entered, and the program returns to the menu screen.

3.7. Area

The AREA option plots the signal intensity vs. time to the screen and calculates the area under a TDS peak using initial and final cursor points specified by the operator. When the AREA option is selected, TFLAG and AFLAG are set to 1, and the operator is asked which mass to plot, "ENTER MASS# (1-(NMASS)):". The X-axis is automatically scaled and the data plotted. At this point the subroutine AREACALC is called, an OPTIONS list and a data box are added to the screen display, and a cursor (crosshair) is displayed in the plotting region.

The OPTIONS list includes three options: R=REDO START, Q=QUIT, and V=VALUE. These options allow the operator to manuever in the AREACALC routine by setting a flag (VFLAG) value. VFLAG can have 3 values to determine which parameters are set. If VFLAG is 0, the initial and final cursor points have not been chosen, so the program is at its beginning. A value of 1 for VFLAG indicates that the initial cursor point has been selected, and a value of 2 indicates that both the initial and final cursor positions are chosen and the area is being computed. Typing an "R" sets VFLAG to 0 and the operator can move the cursor to a new location. If "V" is chosen, information about the selected data point is displayed in the data box. Finally, selecting "Q" returns the program to M2 and displays the prompt, "ANOTHER PLOT? (ENTER 0-8 [0=QUIT])".

Once an initial cursor position is chosen, selecting "V" displays the data about that point in the data box. The data box includes the DATA#, TIME, TEMP, and SIGNAL values specific to that point. This operation is used to determine peak temperatures or times and signal intensities.

The initial and final cursor points are chosen by the operator using the arrow keys to center the cursor on the first point, typing <RET>, and then repeating the procedure for the final point. After the initial point is chosen, a line is drawn connecting the first point to the final point. The slope of this line is used in background subtraction. The incremental movement of the cursor can be reduced by pressing the <insert> key once, and the original increment restored by pressing the <insert> key once again.

The initial and final cursor points are stored as time (TIMEI, TIMEF) or signal intensity values (FIRST(2), LAST(2)), and the X and Y coordinates of FIRST(2) and LAST(2) are (SX1,SY1) and (SX2,SY2). The slope (MSLOPE) of the line between FIRST(2) and LAST(2) is calculated by the ratio of the difference in Y values to the difference in X values. Further, the y-intercept (B) can be calculated using MSLOPE and the FIRST(2) X and Y coordinates. The peak area is actually calculated between two new points, KNT1 and KNT2, where KNT1 is the first data point following FIRST(2) and KNT2 is the data point preceding LAST(2). The X coordinate of KNT1 is defined by CHKTIME and that of KNT2 by CHKTIME2, whereas the Y coordinates of KNT1 and KNT2 are defined by the corresponding TIME2 values.

The area under a TDS peak is determined by selecting initial and final cursor points at the base of a TDS peak, calculating the area, and subtracting the background intensity. The peak area between KNT1 and KNT2 is determined by summing areas of small rectangles. The width (TIMEINT) of these small rectangles is given by the ratio of the range in X values to the number of data points in that range. Initially, AREA is set to 0, and the area of the first rectangle is calculated as the product of its height (W2 - (MSLOPE*TIME2 -B)) and width (TIMEINT) and added to AREA. This procedure is followed until the area of the final rectangle is summed.

3.8. Print

Selecting the PRINT option allows a hardcopy of the current datafile to be printed to the STAR NX-1000 printer. The information printed on the hardcopy includes the filename, slope, AMUs, time intervals, and signal intensity data.

3.8. Graph

Selecting the GRAPH option calls the STORE subroutine, but stores the data in a format compatible with the GRAPHER graphics software package. In particular, the data is stored in a column format, i.e., 10 columns labeled TIME, TEMPERATURE, and AMUs 1-8. Further, the three letter extension following the filename is changed to .DAT.

3.10. Quit

Selecting the QUIT option terminates the TDS program and the computer returns to its original operating system (DOS).

4. CONCLUSIONS

Although the top-down style of the ELECTRA TDS program seems structurally complex, the menu-driven approach is user friendly and makes the program easy to run. By selecting menu options, the operator can easily change file parameters, acquire data, store or retrieve data to or from floppy disks, and plot data to various devices. This computer-interfaced capability greatly simplifies the acquisition and manipulation of TDS data.

5. ACKNOWLEDGEMENTS

The initial version of this program was written by Dr. J. Lynn Davis. Several subroutines in this program are modified versions of routines from a program written by Dr. John A. Polta, and edited by Dr. Jim Dyer, Jim Anderegg, and this author.

REFERENCES CITED

1. H. Herz, H. Conrad and J. Küppers, J. Phys. E 12 (1979) 369.

APPENDIX B:

SURFACE PROPERTIES OF PbO_2 and Bi-MODIFIED PbO_2 ELECTRODES

SURFACE PROPERTIES OF PbO_2 AND Bi-MODIFIED PbO_2 ELECTRODES

B. S. Nielsen[2], J. L. Davis[1], and P. A. Thiel[2]

[1]Motorola Inc.,
Fort Lauderdale, FL 33322

[2]Department of Chemistry and Ames Laboratory
Iowa State University
Ames, Iowa 50011 USA

This appendix appears in volume 137 of the Journal of the Electrochemical Society on pages 1017-1022, 1990.

ABSTRACT

We have studied the surface composition and vibrational properties of PbO_2 and Bi-doped PbO_2 electrode surfaces using Auger electron spectroscopy (AES) and high resolution electron energy loss spectroscopy (EELS). Deposition from perchlorate solution yields chlorine-rich oxides. For PbO_2, chlorine tends to segregate at the surface. For Bi-PbO_2, chlorine does not segregate at the surface, but the concentration of chlorine throughout the bulk of the oxide is about three times that in PbO_2. This suggests that Bi and Cl may be chemically bound in the doped oxides. Hydroxyl groups and hydrocarbon fragments are also present throughout the bulk of both films. Both oxides exhibit distinct phonon loss spectra, similar to those observed by other authors with EELS for many other oxides. Subtle differences between vibrational frequencies of the two oxides may be related to differences in surface crystallographic orientation or to differences in chemical composition.

1. INTRODUCTION

Surface oxides inevitably form during anodization of metal electrodes. Thus, the role of metal oxide electrodes in various anodic electrode processes, e.g., electrosynthesis [1] and oxygen transfer reactions (OTRs) [2], is an important topic of investigation. Lead dioxide (PbO_2) electrodes are interesting because they are non-stoichiometric, they possess accessible surface oxygen, and they have high oxidizing power at high oxygen overpotential [2, 3]. In addition, PbO_2 electrodes function electrocatalytically in oxygen transfer reactions [4]. In 1986, Yeo and Johnson reported that the incorporation of Bi into the PbO_2 matrix (hereafter referred to as Bi-PbO_2) further enhances these anodic OTRs [2]. However, at present there is little understanding of why or how Bi exerts this important effect.

Oxygen transfer is thought to proceed by mechanisms involving surface oxygen extraction from the metal oxide lattice and subsequent oxygen atom replacement by the anodic discharge of water [4]:

$$MO_x + R \text{ ---> } MO_{(x-1)} + RO$$

$$MO_{(x-1)} + H_2O \text{ ---> } MO_x + 2H^+ + 2e^-$$

In these reactions, MO_x is the metal oxide (PbO_2 or Bi-PbO_2), $MO_{(x-1)}$ represents the oxygen deficient metal oxide, R is the reactant (O-acceptor), and RO is the oxygen-rich product. With Bi present in or on the PbO_2 surface, the OTRs occur at half-wave potentials ($E_{1/2}$s) near that of the Bi^{3+}/Bi^{5+} redox couple, which is less than the potential required for di-oxygen evolution at pure PbO_2 [4]. Yeo and Johnson have amperometrically determined that Bi-doping of the PbO_2 electrodes significantly increases the heterogeneous rate constants for several anodic OTRs relative to the undoped electrodes [2]. This observation of enhanced catalytic activity is consistent with previous studies of the catalytic effect of Bi in various metal oxide matrices [5, 6]. The presence of Bi in the PbO_2 electrode film also increases the stability of the electrode by increasing its useful voltammetric range [2].

Several models have been proposed to explain the effect of Bi on PbO_2 electrodes. Originally, Yeo and Johnson used Bi as a dopant because the stoichiometry of the Bi^{5+} oxide, $BiO_{2.5}$, is such that there must be a higher oxygen content than for PbO_2 [2]. (The electrode potential applied during electrodeposition of Bi-PbO_2 is sufficient to oxidize Bi^{3+} to Bi^{5+} [2].) Thus, they envisioned that the Bi dopant creates oxygen-rich defect sites in the PbO_2 lattice, thereby enhancing the electrode's capacity for oxygen transfer [2]. However, later experiments with other dopants failed to support this simple "rule of stoichiometry" [2, 4, 7, 8]. A subsequent study of the structures of the films, using x-ray diffraction (XRD), indicated that the Bi dopant induces the films to grow with a preferential orientation different from that of the pure PbO_2 films [8, 9]. The Bi-PbO_2 films grow with an oxygen-rich plane preferentially exposed at the surface, which briefly led to speculation that this might be the source of the Bi enhancement [7]. Yet this hypothesis, too, was eventually discarded because there is no systematic correlation between the effect of various ions as dopants in OTRs, and the orientation of the doped PbO_2 film [8]. Most recently, Johnson and coworkers suggested that the dopant enhances oxidation because it has weaker metal-oxygen bonds than are present in the lead matrix, and it thus releases oxygen more readily to the oxidant [8]. At the same time, they suggested that it is important for this dopant to be interstitially incorporated into the PbO_2 lattice [8].

The surface properties of PbO_2 and Bi-PbO_2 electrodes can affect the rates of oxygen-transfer reactions. Thus, characterization of these surfaces using surface sensitive electron spectroscopies is essential to understanding the processes involved in anodic OTRs. In this paper, we present the first study of PbO_2 and Bi-PbO_2 films analyzed with Auger electron spectroscopy (AES) and electron energy loss spectroscopy (EELS). Auger electron spectroscopy provides an elemental analysis of the surface. In addition, the combination of AES and Ar^+ sputtering (hereafter referred to as depth profiling) is used to examine the composition of the electrodeposited films as a function of depth. We employ high resolution EELS to determine the surface vibrational properties of the PbO_2 electrodes and the effect of Bi-doping on these properties. The goal of our work is to compare the composition and vibrational properties of the two oxide surfaces so we can test if there is a relationship between the electrode surface properties and the enhanced electrocatalytic activity of the Bi-PbO_2 electrodes.

2. EXPERIMENTAL

2.1. Electrode Preparation

Gold foil is used as the substrate for the films of PbO_2 and Bi-PbO_2. The Au foil is cleaned with acetone and methanol, rinsed with triply distilled water, and dried in air before deposition. The PbO_2 layers are made by electrodepositing PbO_2 on the Au foil from a solution of 10 mM $Pb(NO_3)_2$ in 1.0 M $HClO_4$ at a potential of + 1.6 V vs SCE for 20 minutes. The Bi-PbO_2 electrodes are electrodeposited from a solution of 10 mM $Pb(NO_3)_2$ and 5 mM $Bi(NO_3)_3$ in 1.0 M $HClO_4$ at + 1.6 V vs SCE for 25 minutes. The Bi/Pb atomic ratio in the resultant film is approximately 0.4 [7]. The oxide film thickness is 100 ± 10 mm ($1.0 \pm 0.1 \times 10^6$ Å). Following electrodeposition, the solutions, rinsed thoroughly with triply distilled water, and allowed to dry in air.

2.2. Surface Analysis

After preparation as described above the sample is mounted directly onto a button heater (Spectra-Mat) via Ta clips spotwelded to the heater. The sample is then transferred into an ultrahigh vacuum (UHV) chamber, where it can be heated conductively and radiatively by passing current through the heater. The sample temperature is measured using W-5% Re and W-26% Re thermocouple wires spotwelded directly to the heater and in contact with the back of the Au foil. The sample is then transferred into the UHV chamber, and the system is baked for 12 to 24 hours at ca. 100°C to achieve UHV conditions.

The stainless steel UHV chamber has a typical base pressure of 1×10^{-10} Torr. The chamber is pumped by a 400 L/s ion pump, a 50 L/s turbomolecular pump, and a titanium sublimator. The surface characterization and preparation devices include a retarding field analyzer for Auger electron spectroscopy, a high resolution electron energy loss spectrometer, and an ion bombardment gun. The arrangement of these devices is shown schematically in Figure 1.

The AES and depth profile experiments are performed using a retarding field energy analyzer and an ion bombardment gun. Typical conditions for the AES experiments are 1.5 kV beam energy, 0.5 mA current at the sample, and 5 eV peak-to-peak modulation amplitude. Typical conditions for Ar^+ sputtering are 1.0 kV beam energy and 1.0 mA current at the sample.

The EELS experiments are performed with a commercial spectrometer from McAllister Technical Services. It consists of 127° sectors for both the monochromator and analyzer. The sectors are mounted in the "double C" configuration, and the entire spectrometer is surrounded by μ-metal magnetic shielding to minimize stray magnetic fields. Typical conditions for the EELS experiments are 2.5 eV beam energy and 2.0×10^{-10} A current at the sample. The spectra are recorded in the specular geometry with a typical resolution of 160 cm^{-1} for the elastically scattered peak.

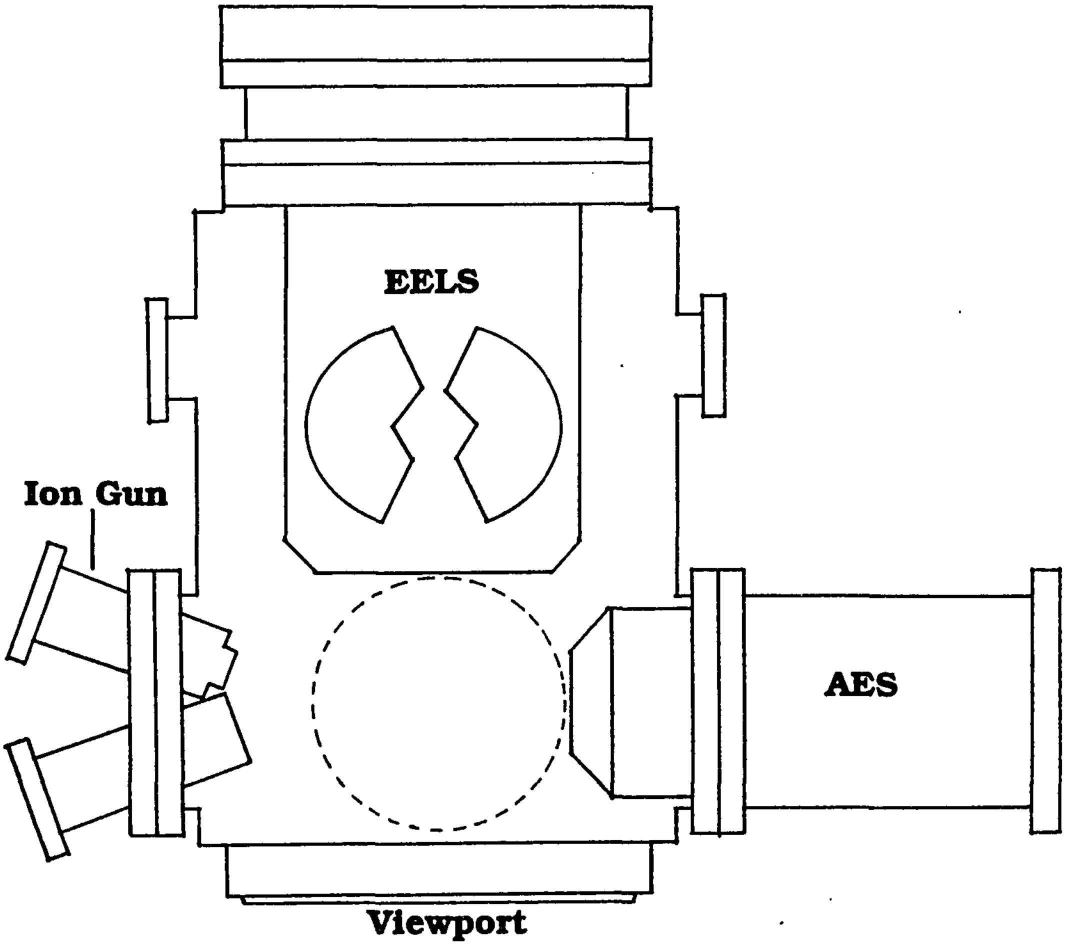

Figure 1. Schematic cross-section of the ultrahigh vacuum (UHV) chamber. The dashed circle indicates the focal point circle, the circle around which the sample can move. The system is pumped by a 50 L/s turbomolecular pump (not shown) and a 400 L/s ion pump with a titanium sublimator (also not shown).

3. RESULTS

3.1. Undoped PbO_2 Electrodes

Auger electron spectroscopy studies of the undoped PbO_2 films suggest that the electrodes consist of a complex mixture of Pb, O, and Cl. Transitions are assigned on the basis of published reference data [10]. In Figure 2, the peaks at 90, 242, and 263 eV are the Auger transitions of Pb, the peak at 179 eV is due to Cl, and the peak at 515 eV represents 0. The presence of Au, presumably from the substrate, is observed as a peak at 55 eV. If the PbO_2 film were pure and contiguous, the Au should not be visible in AES. This is because the mean free path of the Auger electrons (the effective sampling depth of AES) is 10^2 Å <u>at the most</u>, and the PbO_2 films are nominally 10^6 Å deep. The presence of Au in the Auger spectra is probably due instead to cracks or pinholes in the PbO_2 film, since these are sometimes even visually apparent in the films. In addition, a small amount of hydrocarbon exists as a contaminant, based on the EELS data (see below). However the C Auger transition (normally at 272 eV [10]) is not clearly observed, perhaps partly due to overlap with the Pb transition at 265 eV.

The appearance of a Cl transition at 179 eV indicates that Cl is present at the undoped PbO_2 surface. The majority of this surface Cl originates from the 1.0 M $HClO_4$ plating bath used for electrodeposition, rather than from atmospheric contamination when the sample is transferred from solution to UHV. This conclusion rests on the fact that a film deposited from a 1.0 M HNO_3 plating bath instead of $HClO_4$ exhibits

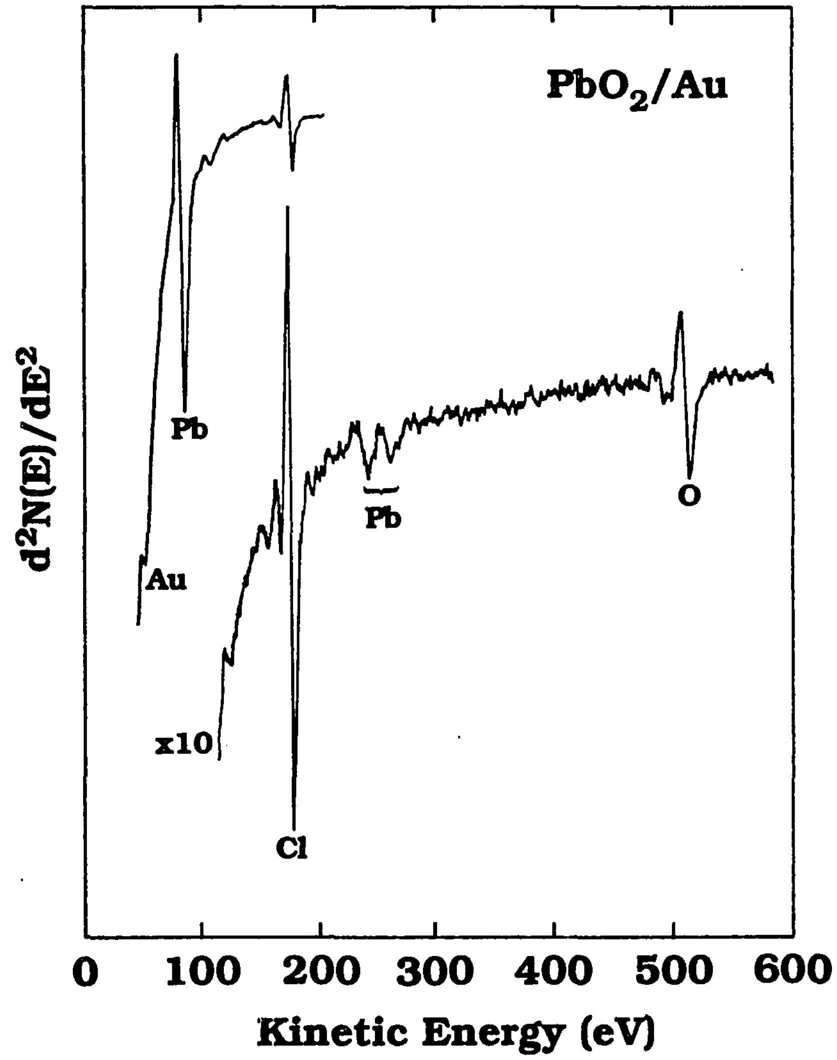

Figure 2. Auger spectrum of the undoped PbO$_2$ electrode. Auger transitions are assigned to Au, Pb, Cl, and O according to reference [10].

the Auger spectrum shown in Figure 3. As shown in Figure 3, Cl is again observed at 179 eV; however, the intensity of this peak is significantly less than the Cl peak observed in Figure 2. The absence of an intense Cl peak in Figure 3 suggests that only trace amounts of Cl exist on the surface which is deposited from the HNO_3 solution; however, a N transition at 381 eV [10], which would be diagnostic for incorporated nitrate or nitrogen, is not observed. In addition, Auger transitions for Pb and O are again identified. The peaks at 89, 242, and 263 eV are assigned to Pb transitions, while the peak at 515 eV is assigned to 0.

Depth profiling probes the spatial homogeneity of the electrode films, in the direction perpendicular to the surface plane. The depth profile of the PbO_2 film is shown in Figure 4. The concentration ratios are calculated as the ratio of the peak-to-peak height of the specified element relative to that of the Pb peak at 90 eV. The concentration profile of the PbO_2 film shows that the O/Pb ratio remains constant as the film is sputtered away. In contrast, the Cl/Pb ratio decreases by a factor of three as the surface layer is sputtered away and then remains constant, but nonzero, upon further sputtering. Thus, our results indicate that Cl concentrates preferentially at the surface but is also present within the PbO_2 matrix.

High resolution EELS studies of the undoped PbO_2 electrodes reflect the nature of the chemical bonds at or near the surface. The EEL spectrum of the PbO_2 film is shown in Figure 5, with the loss frequencies summarized in the first column of Table 1 [11]. The spectrum consists of two main regions, one with low frequency losses ($< 2900\ cm^{-1}$) and one

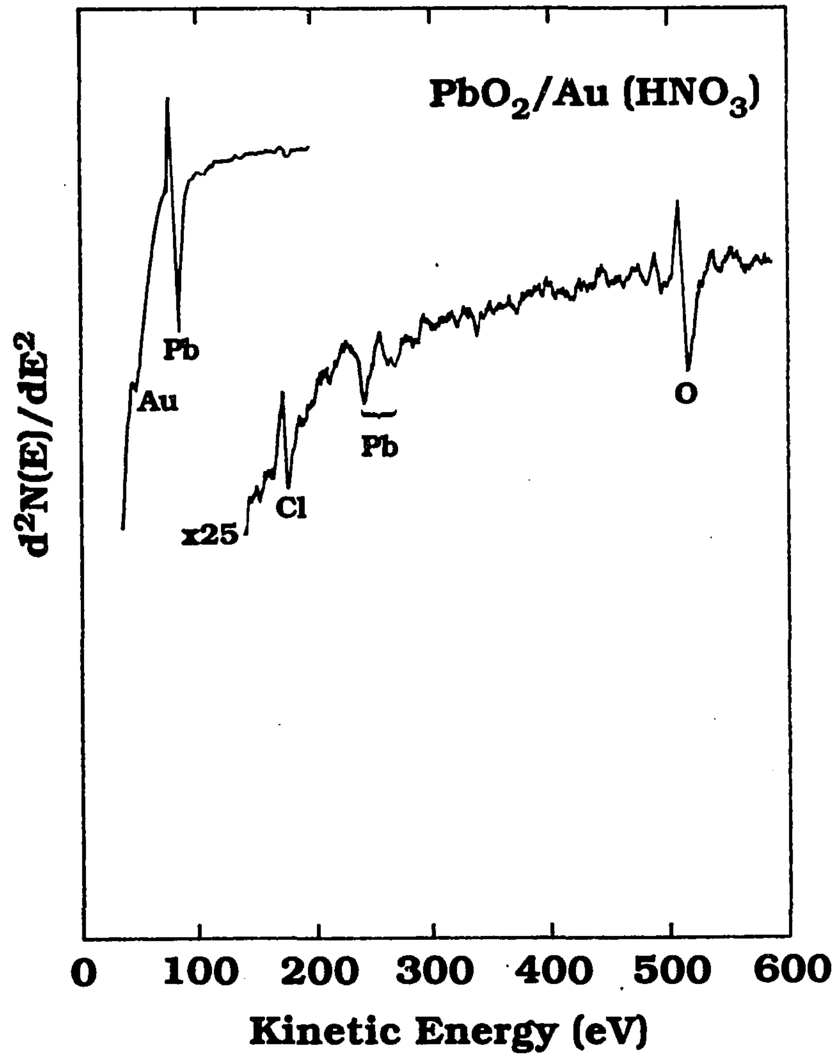

Figure 3. Auger spectrum of an undoped PbO$_2$ electrode deposited from a 1.0 M HNO$_3$ plating bath. Auger transitions are assigned to Au, Pb, Cl, and O according to Ref. [10].

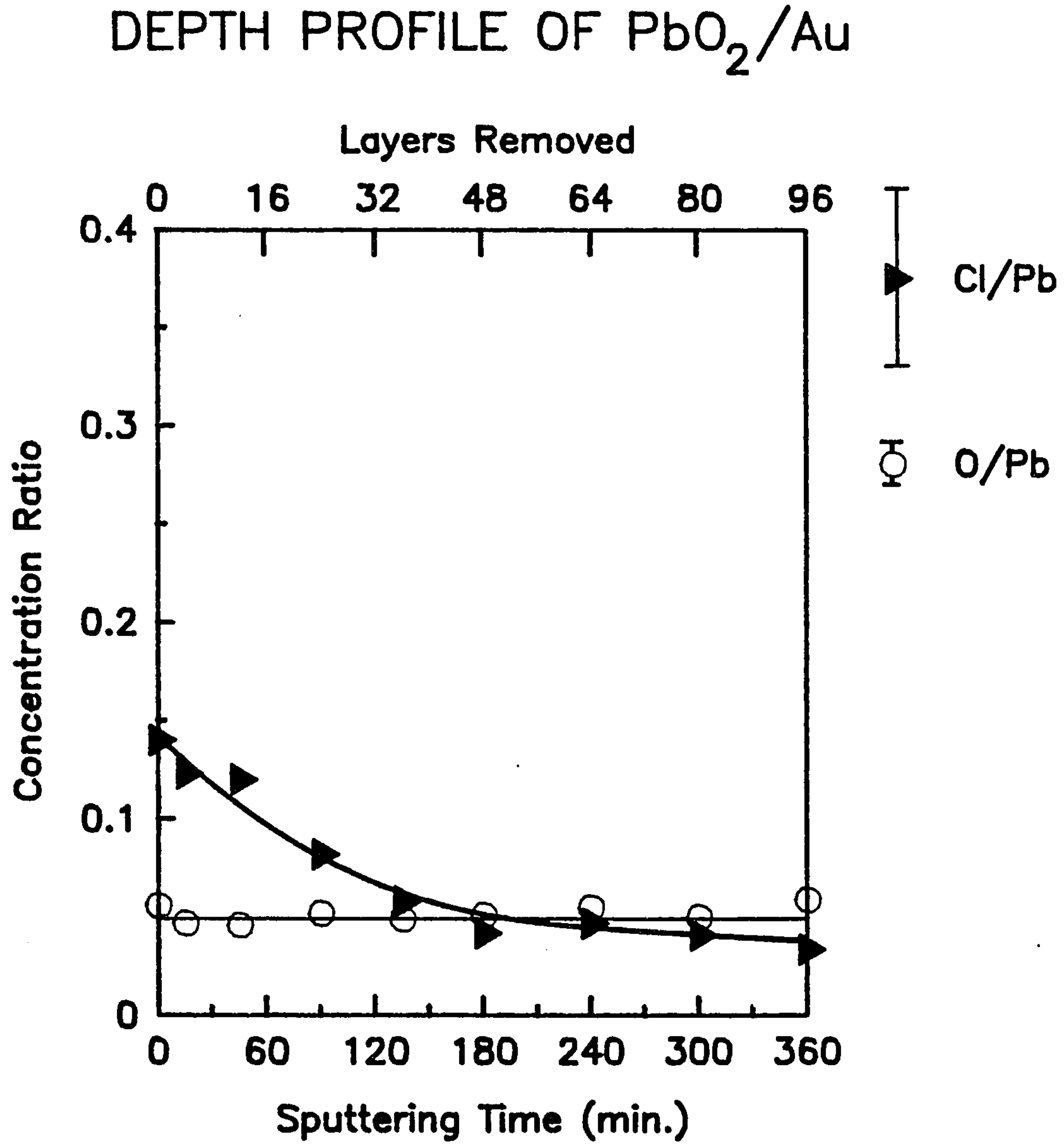

Figure 4. Depth profile of the undoped PbO_2 electrode. The calculation of concentration ratios is described in the text. The solid lines are drawn to guide the eye. The top abscissa is labelled with sputtering depth, calculated by assuming a sputtering yield of unity and removal of one surface layer at a time. The depth profile results from two separate experiments, and the error bars represent the standard deviations in the measurements.

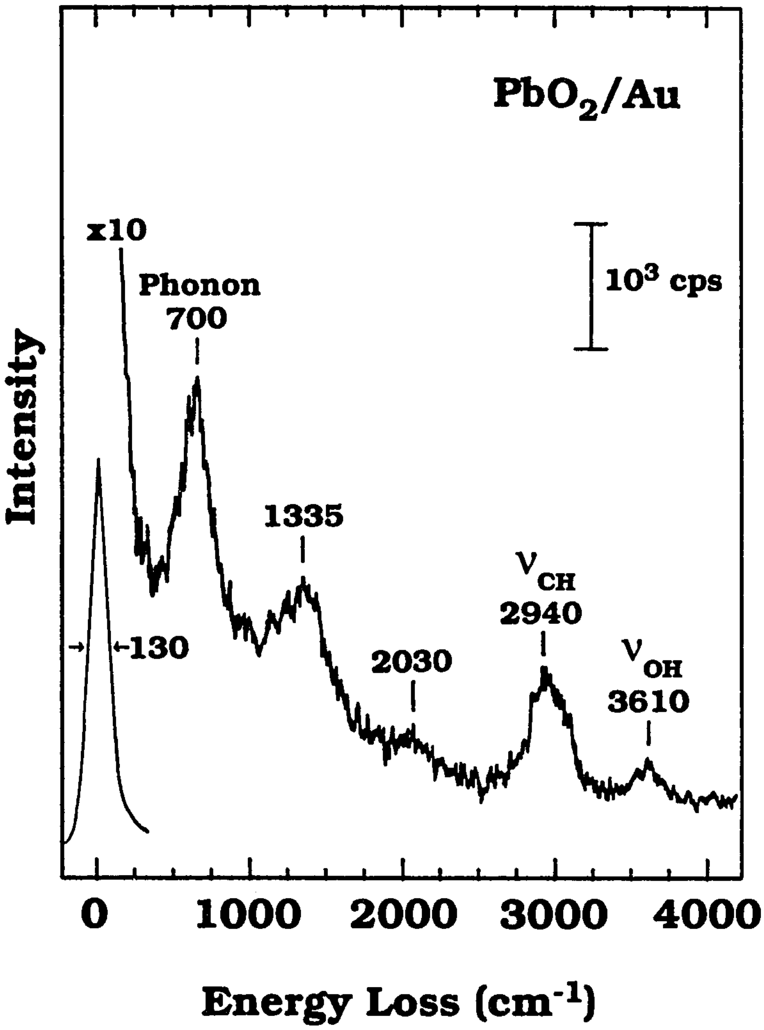

Figure 5. Electron energy loss spectrum of the undoped PbO$_2$ electrode. The vibrational mode assignments are summarized in Table 1.

	PbO_2	Bi-PbO_2	Sputtered Bi-PbO_2
n_1	700 ± 20	785 ± 25	695 ± 5
n_2	1335 ± 20	1350 ± 35	1345 ± 15
n_3	2030 ± 40	2070 ± 160	2010 ± 70
n_4	2940 ± 35	2965 ± 35	2970 ± 45
n_5	3610 ± 45	3770 ± 40	3595 ± 25
n	30	12	3
k	3	4	3

Table 1. Frequencies (in cm^{-1}) of major loss features observed in EELS, rounded to the nearest 5 cm^{-1}. n_1 - n_3 are frequencies of phonons, as described in the text. Values are quoted as the mean, plus/minus on standard deviation, calculated from n (the total number of EELS measurements) and k (the number of different oside samples studied), as described in Ref. [11].

with high frequency losses (> 2900 cm^{-1}). The spectra do not resemble published infrared or Raman spectra of discrete lead oxide molecules or clusters, e.g. PbO, Pb_2O_2, or Pb_4O_4 [12, 13]. Rather the low frequency losses observed at 700 ± 20, 1335 ± 20, and 2030 ± 40 cm^{-1} exhibit several characteristics which identify them as single and multiple phonon excitations, similar to those observed previously for ZnO [14], NiO [15-17], TiO_2 [18], MgO [19, 20], $SrTiO_2$ [21], WO_3 [22], $Na_{0.7}WO_3$ [22], and Al_2O_3 [23-27]. First, the low-frequency losses in Figure 5 appear at regular intervals; that is, the frequency differences between the losses are constant, within experimental error, at 675 cm^{-1}. This observation suggests that the second and third losses represent multiple excitations, and the first loss feature represents a single vibrational excitation. Second, the intensities of the three losses decrease with increasing frequency. For multiple excitations, the intensity is known to vary with number of excitations according to a Poisson distribution [14, 28], and this is consistent with our observation. Finally, in some PbO_2 spectra, a low frequency <u>gain</u> is observed at a frequency near 700 cm^{-1}; however, the intensity of the peak is extremely low and an exact gain frequency is difficult to assign. These characteristics suggest that the low-frequency losses arise from single and multiple excitations of phonons, i.e., lattice vibrations. These three characteristics have <u>all</u> been observed in previous EELS studies of metal oxides, where they are specifically associated with long-wavelength optical (Fuchs-Kliewer) phonons [14-27].

In the EEL spectra, we do not see any features which we can specifically assign to $PbCl_2$ or Pb-Cl vibrations. The characteristic Pb-Cl modes occur at frequencies below 350 cm^{-1} [29]. We do not observe these, perhaps because they are masked by the tail of the elastic peak. There are also no features in the range 950-1270 cm^{-1}, which is the range where characteristic Cl-O stretching frequencies occur in metal perchlorates [30]. Again, if these were present they could be so weak that they would be effectively masked by the phonon loss at 1335-1350 cm^{-1}.

High frequency loss features are also observed in the EEL spectrum of PbO_2. The high frequency region in Figure 5 includes losses at 2940 ± 35 and 3610 ± 45 cm^{-1}. We assign the feature at 2940 cm^{-1} to a ν_{CH} mode, presumably arising from contamination by hydrocarbons. The remaining high frequency loss feature at 3610 cm^{-1} may be a ν_{OH} mode, arising from hydroxyl species, and/or it may be a combination of the 700 cm^{-1} phonon and the ν_{CH} mode at 2940 cm^{-1}. It is highly unlikely that this feature represents molecular water, present as a hydrate or occluded in the film. Molecular water would almost certainly evaporate very soon after the sample is transferred to vacuum, since water is not generally stable on metal or metal oxide surfaces at room temperature in vacuum [31].

The EELS features of the PbO_2 films remain unchanged after heating to 450 K or following exposure to oxygen in the pressure range 10^{-9} to 5×10^{-7} Torr (total exposures up to 50 L), at room temperature.

3.2. Bi-doped PbO_2 Electrodes

The AES studies indicate that the composition of the doped PbO_2 electrode surface is grossly similar to that of the undoped surface. Auger transitions for Pb, Bi, O, and Cl are identified in the Auger spectrum in Figure 6. For the calculation of concentration ratios, the transition at 90 eV is assumed to represent pure Pb, and likewise, the transition at 97 eV to represent pure Bi, even though there is clearly some overlap between the two features which affects their relative intensities. The two peaks at 244 and 267 eV represent overlapping Pb and Bi transitions. Further, the O transition is assigned to the peak at 514 eV. The presence of Au, related to the substrate, is again observed as a peak at 55 eV. As in the undoped films, Cl is present in the Bi-PbO_2 films and is identified as the peak at 181 eV. Finally, hydrocarbons are also present, based on the EEL spectra (see below). However, the C transition (normally at 272 eV [10]) is not observed. A weak C feature could be obscured by the combination (Pb + Bi) transition at 267 eV.

Depth profiling suggests that the Bi-PbO_2 films are more homogeneous than the undoped PbO_2 films. The depth profile of the Bi-PbO_2 film is shown in Figure 7, and the concentration ratios for Cl and O are calculated in the same manner as previously described. The Bi/Pb concentration ratio is calculated as the ratio of the peak height of the Bi transition at 99 eV, measured from a linearly extrapolated baseline, to the peak-to-peak height of the Pb transition at 90 eV. For the doped film, the Bi/Pb, Cl/Pb and O/Pb concentration ratios remain constant throughout the sputtering time. Our data indicate that Bi, Cl and O do

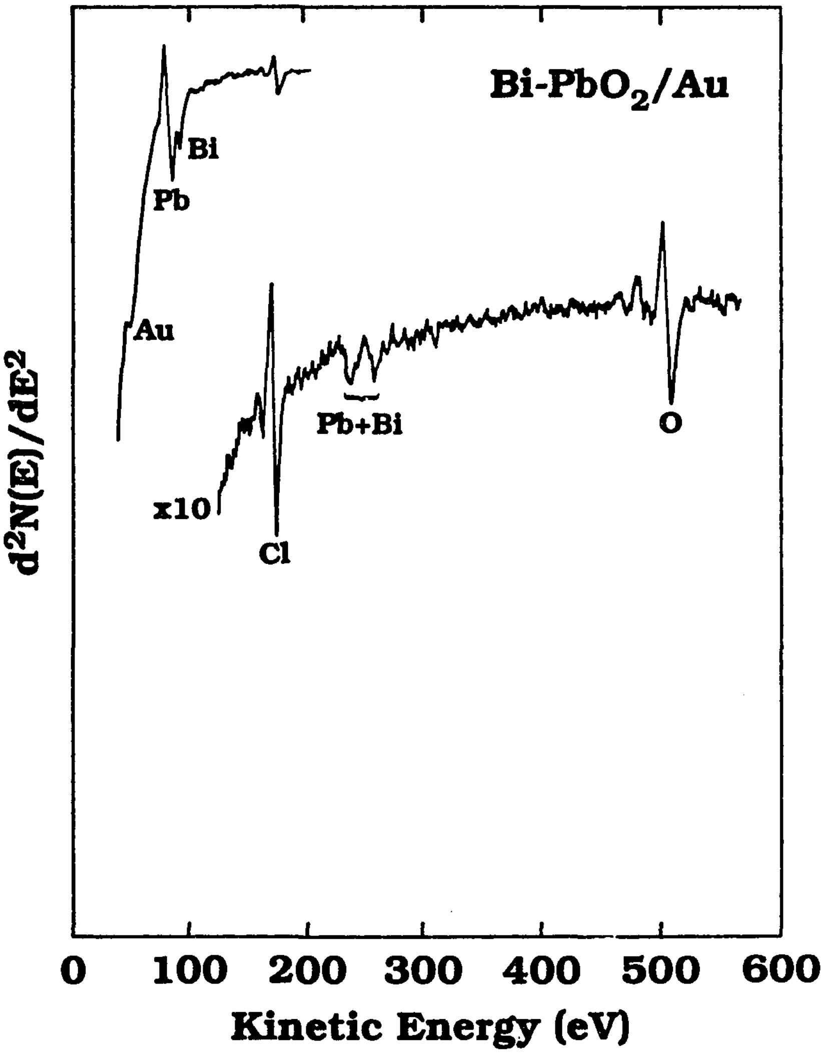

Figure 6. Auger spectrum of the Bi-PbO$_2$ electrode. Auger transitions are assigned to Au, Pb, Bi, Cl, and O according to Ref. [10].

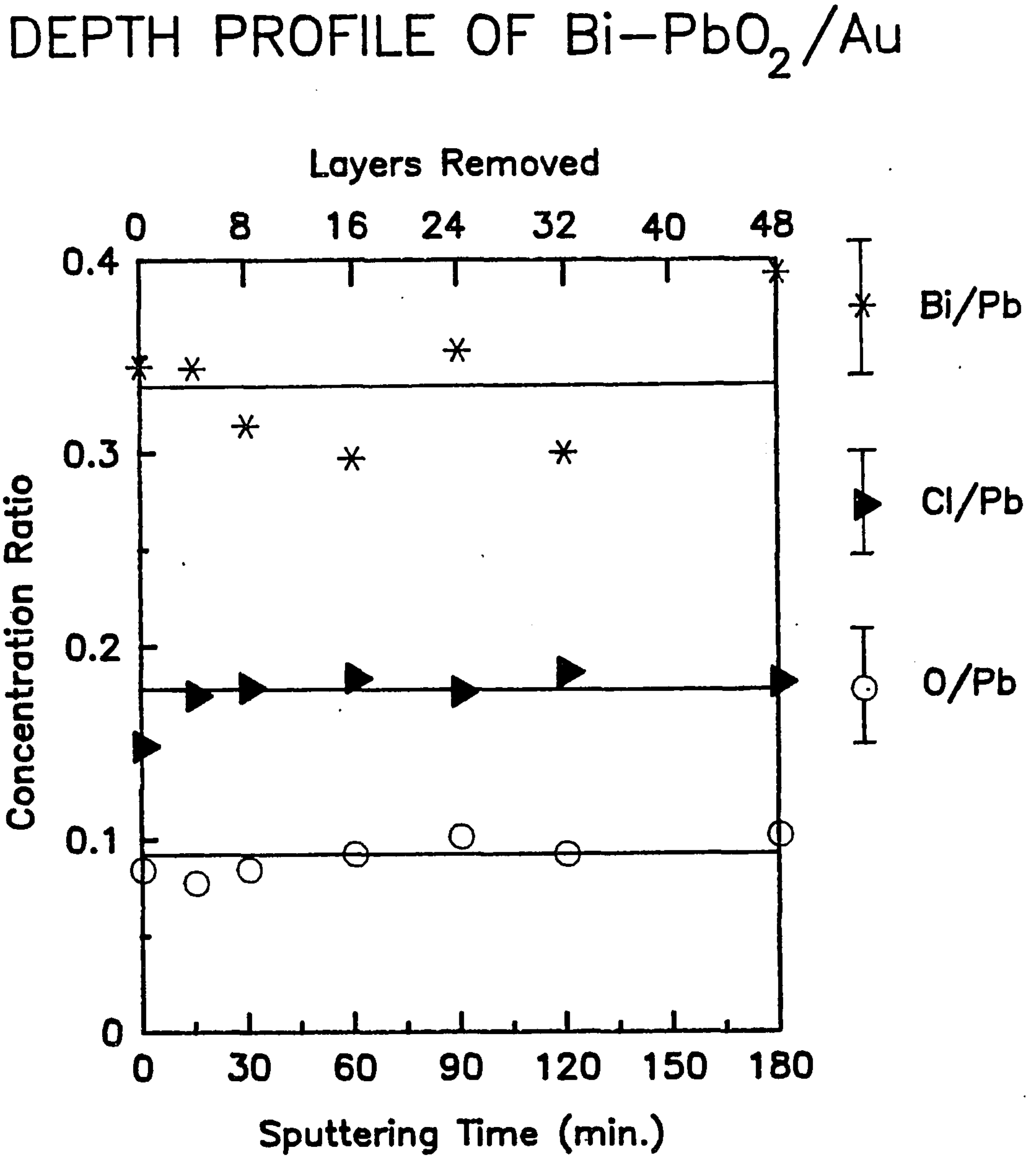

Figure 7. Depth profile of the Bi-PbO$_2$ electrode. The calculation of concentration ratios is described in the text. The solid lines are drawn to guide the eye. The top abscissa is labelled with sputtering depth, calculated by assuming a sputtering yield of unity and removal of one surface layer at a time. The depth profile results from two separate experiments, and the error bars represent the standard deviations in the measurements.

not segregate to the surface of these electrodes, thus suggesting that Bi is uniformly distributed throughout the thickness of the film, and that the Bi-PbO_2 films are more homogeneous in composition than the PbO_2 films.

Surface phonon modes are again observed in the EEL spectra of Bi-PbO_2. The EEL spectrum of the Bi-PbO_2 electrode is shown in Figure 8 with the loss frequencies summarized in the second column of Table 1. Three intense, low-frequency modes and two high frequency losses are observed in this spectrum. As in the undoped film, the intensities of the first three losses at 785 ± 25, 1350 ± 35, and 2070 ± 160 cm^{-1} decrease with increasing frequency. Further, in some EEL spectra, a low intensity <u>gain</u> feature is observed at a frequency near 785 cm^{-1}. In this low-frequency regime, the only significant difference between the Bi-PbO_2 film spectra and the PbO_2 film spectra lies in ν_1, which is about 80 cm^{-1} <u>higher</u> for the Bi-PbO_2 films. Note that the ν_2 and ν_3 values are <u>not</u> shifted upward, and this suggests a contribution to ν_1 which is not related to a lattice phonon, at least in the Bi-doped films.

The EEL spectra for Bi-PbO_2 also exhibit features at higher frequencies. In the EEL spectrum shown in Figure 8, high frequency losses are observed at 2965 ± 35 and 3770 ± 40 cm^{-1}. As for PbO_2, the loss at 2965 cm^{-1} is assigned as ν_{CH}, due to hydrocarbon contamination. The loss feature at 3770 cm^{-1} may be a ν_{OH} mode arising from hydroxyl, and/or a combination of two lower frequency modes, specifically, those occurring at 785 and 2965 cm^{-1}. This 3770 cm^{-1} feature is significantly higher in frequency for the Bi-PbO_2 films than for the PbO_2 films, as shown by Table 1 as well.

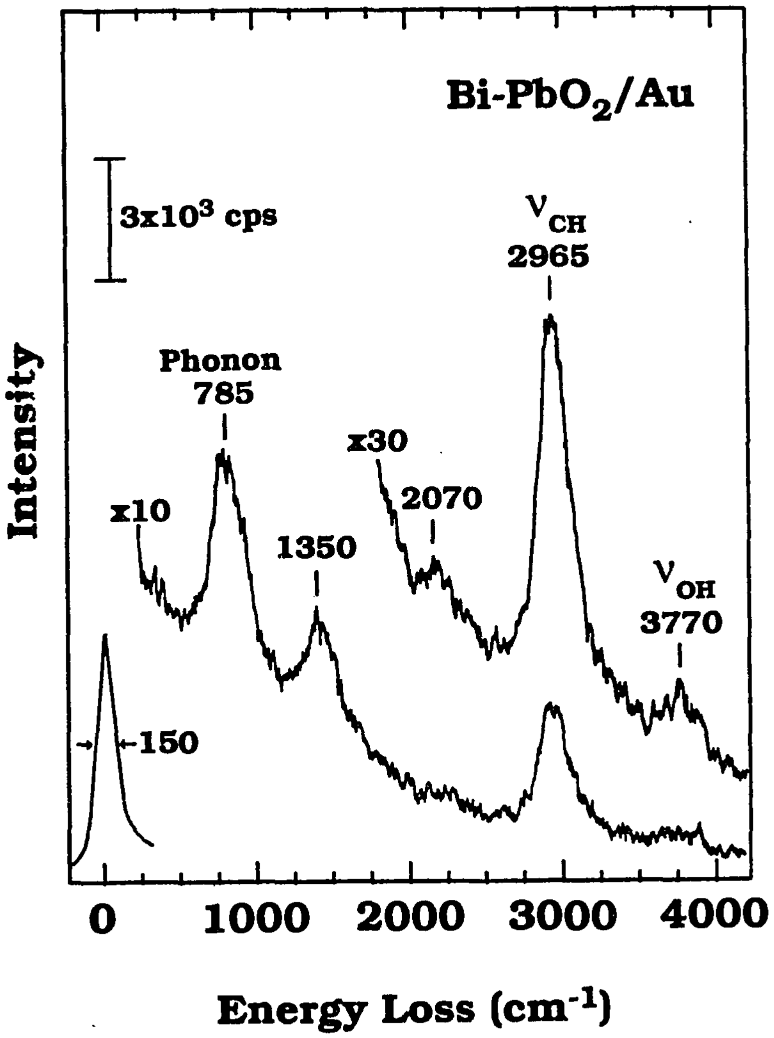

Figure 8. Electron energy loss spectrum of the Bi-PbO_2 electrode. The vibrational mode assignments are summarized in Table 1.

After the Bi-PbO_2 film is sputtered, the EEL spectra resemble those of the original undoped PbO_2 film. The EELS frequencies measured for the sputtered oxide films are summarized in the third column of Table 1. Sputtering the doped film with Ar^+ for ca. 3 hours causes the frequencies of the 785 and 3770 cm^{-1} peaks to decrease to the point where there is no significant difference between the EEL spectra of the PbO_2 film and the sputtered Bi-PbO_2 film.

Finally, we note that all the EELS features of the Bi-PbO_2 films are insensitive to heating, at sample temperatures up to 500 K. This indicates that the crystal structure remains intact to these temperatures, and that any hydrocarbon and hydroxyl species are also stable under these conditions.

4. DISCUSSION

One of the main results of this study lies in the fact that chlorine is unambiguously present, both at the surface and in the bulk, of pure and Bi-doped PbO_2 films. The main source of this chlorine is undoubtedly the $HClO_4$ present in solution as the film grows, as proven by comparison of Figures 2 and 3. Many of the PbO_2 films, and all of the electrochemically-grown Bi-PbO_2 films, described in the literature up to now have been deposited from $HClO_4$-containing solutions [2, 4, 7-9]. Thus, our findings show that chlorine has probably been a contaminant in most other films described in the literature. The chlorine may be incorporated as perchlorate, as atomic chloride, or as some form of metal oxychloride. Perchlorate is a rather large ion whose inclusion in the PbO_2 lattice seems unlikely; furthermore, we do not observe distinct EELS features in the range characteristic of metal perchlorates, 950-1270 cm^{-1} [30]. On the other hand, the ClO_4^{1-} ion may be incorporated preferentially at domain boundaries and defect sites; and the loss feature due to the Cl-O stretch may be obscured by the intense lattice phonon. The possibility of ClO_4^{1-} is supported (and the possibility of chloride is discounted) by the fact that the films are deposited at oxidizing potentials. Our data are not adequate at this point, however, to determine the chemical form of the chlorine in these films. It must be noted that no crystalline materials beside PbO_2 were detected in the previous XRD study [8, 9], but the detection limit in the XRD work was probably on the order of 5% [32].

The role of this chlorine in affecting the catalytic properties of the electrode is unknown. However, it is striking that one pronounced difference between PbO_2 and Bi-PbO_2 films lies in the spatial distribution of chlorine within the sample. For the PbO_2 electrodes, chlorine is located preferentially at the surface, whereas for the Bi-PbO_2 electrodes it is not. In addition, below the surface region, the chlorine concentration in the PbO_2 film drops (on average) to about one third of that in the Bi-PbO_2 film. At the surface, the concentration of chlorine is the same in the two samples, within ca. 20%. This is shown by comparison of Figures 4 and 7.

These data suggest that Bi enhances the tendency to incorporate Cl into the oxide lattice as it grows. The presence of Bi may enhance the incorporation of Cl as BiCl- or BiOCl-containing units into the oxide lattice, for instance, relative to PbCl- or PbOCl-containing units. Alternatively, Bi may create relatively more defect sites in the PbO_2 lattice where ClO_4^{1-} can be trapped. The fact that there is preferential surface concentration of Cl in the PbO_2 films but not in the Bi-PbO_2 films is more difficult to explain. This may be related to the effect of doping on the surface roughness of the films, or to the role which Bi plays in the kinetics of film deposition.

More subtle differences between the PbO_2 and Bi-PbO_2 films are revealed by EELS, as summarized by the first and second columns in Table 1. For both oxide surfaces, the vibrational spectra show a series of phonon losses, labelled ν_1, ν_2 and ν_3. Based upon comparison with characteristics of oxide phonons published in many other EELS studies

[14-27], we identify these three features as lattice phonons. The similarity between these losses for the two oxides is consistent with previous XRD work, which showed only a very slight lattice expansion (less than 1%) in the Bi-PbO_2 films, with the rutile structure preserved [8, 9]. The value of ν_1 is slightly but significantly higher for the Bi-PbO_2 film than for the PbO_2 film, as is the value of ν_5. One possible explanation for this effect is that ν_5 is primarily a combination of the ν_1 and ν_4 modes. Within the limits of error associated with the measurement, then, the upward shift in ν_1 would account for the simultaneous shift in ν_5. The upward shift in ν_1 could be due to overlap between a single phonon excitation (presumably at ~675 cm^{-1}, judging by the positions of ν_2 and ν_3) and a higher frequency mode associated with the Bi-O stretch of surface oxygen. Alternatively, there could be a surface hydroxyl species associated with the Bi atoms which accounts for these same changes in ν_1 and ν_5. The value of ν_1 measured on the PbO_2 surface is also slightly higher than expected (700 cm^{-1}), relative to the spacing between ν_1, ν_2 and ν_3, suggesting that there is some extra high frequency contribution to ν_1 there as well, perhaps by an analogous species.

Interpretation of the EEL data after sputtering must be accompanied by knowledge that sputtering is known to reduce the amount of hydroxide present at a metal oxide surface relative to the amount of oxide surface, and even in some cases to convert the oxide to the metal [33]. Therefore, the changes in frequency observed after depth profiling may be due to changes in chemical composition which are present <u>before</u> ion etching, or to changes which are <u>induced by</u> ion etching. However, sputtering produces no major changes in the intensity or shape of any vibrational features, only changes in frequency. This suggests that ν_5 is more probably a combination band than an O-H stretch, since hydroxyl species would almost certainly be depleted by ion bombardment, resulting in a decrease in relative intensity of ν_5.

In summary, we have used AES and EELS to identify components of PbO_2 and Bi-PbO_2 films. Electrodeposition onto gold foil in $HClO_4$ produces chlorine-containing oxides. Depth profiles of the undoped PbO_2 film suggest that Cl segregates to the surface, whereas there is no evidence of surface Cl segregation in the doped film. Further, the EEL spectra of PbO_2 consist of equally spaced phonon losses at 700, 1335, and 2030 cm^{-1}, a weak ν_{CH} mode at 2940 cm^{-1}, and a mode at 3610 cm^{-1}. Phonon losses are also observed at 785, 1350, and 2070 cm^{-1} in EEL spectra of Bi-PbO_2, a weak ν_{CH} mode is again present at 2965 cm^{-1}, and a mode at 3770 cm^{-1} is also present. The differences in vibrational frequencies of Bi-doped PbO_2, relative to those of PbO_2, are quite subtle.

5. ACKNOWLEDGEMENTS

We gratefully acknowledge valuable conversations with D. C. Johnson and H. Chang. Also, we thank H. Chang for preparing all the electrode samples. This work is supported by the Director for Energy Research, Office of Basic Energy Sciences. Ames Laboratory is operated for the U. S. Department of Energy by Iowa State University under Contract No. W-7405-ENG-82.

REFERENCES CITED

1. R. Varma, J. Eckert, V. A. Maroni, J. A. Goldstone, C. Giodano, T. Cehelnik, R. Kumar, S. Siegel and B. Tani, in: Proc. Symposium on Advances in Lead-Acid Batteries, Pennington, 1984, V. 84-14, p. 44.
2. I.-H. Yeo and D. C. Johnson, J. Electrochem. Soc. 134 (1987) 1973.
3. F. Beck and W. Gabriel, J. Electroanal. Chem. 182 (1985) 355.
4. D. C. Johnson, private communication.
5. R. G. Egdell, J. B. Goodenough, A. Hamnett and C. C. Naish, J. Chem. Soc., Faraday Trans. 1 79 (1983) 893.
6. D. J. Buttrey, D. A. Jefferson and J. M. Thomas, Mat. Res. Bull. 21 (1986) 739.
7. I.-H. Yeo, Ph.D. Dissertation, Iowa State University (1987).
8. I.-H. Yeo, S. Kim, R. Jacobson and D. C. Johnson, J. Electrochem. Soc., in press
9. S. Kim, Ph.D. Dissertation, Iowa State University (1986).
10. P. W. Palmberg, G. E. Riach, R. E. Weber and N. C. MacDonald, Handbook of Auger Electron Spectroscopy, (Physical Electronic Industries, Inc., Edina, 1972).
11. D. A. Skoog, Principles of Instrumental Analysis, Third Edition (Saunders, Philadelphia, 1985).
12. J. S. Ogden and M. J. Ricks Jr., J. Chem. Phys. 56 (1972) 1658.
13. R. K. Khanna and Y. J. Park, Spectrochim. Acta 42A (1986) 603.
14. H. Ibach, Phys. Rev. Lett. 24 (1970) 1416.
15. P. A. Cox and A. A. Williams, Surf. Sci. 152/153 (1985) 791.
16. G. Dalmai-Imelik, J. C. Bertolini and J. Rousseau, Surf. Sci. 63 (1977) 67.
17. F. T. Wagner and T. E. Moylan, J. Electrochem. Soc., in press (1989)

18. L. L. Kesmodel, J. A. Gates and Y. W. Chung, Phys. Rev. B 23 (1981) 489.

19. P. A. Thiry, M. Liehr, J. J. Pireaux and R. Caudano, Phys. Rev. B 29 (1984) 4824.

20. M. Liehr, P. A. Thiry, J. J. Pireaux and R. Caudano, Phys. Rev. B 33 (1986) 5682.

21. A. D. Baden, P. A. Cox, R. G. Egdell, A. F. Orchard and R. J. D. Willmer, J. Phys. C 14 (1981) L1081.

22. D. G. Aitken, P. A. Cox and R. G. Egdell, Vacuum 33 (1983) 753.

23. J. E. Crowell, J. G. Chen and J. T. Yates Jr., Surf. Sci. 165 (1986) 37.

24. J. L. Erskine and R. L. Strong, Phys. Rev. B 25 (1982) 5547.

25. J. G. Chen, J. E. Crowell and J. T. Yates Jr., Phys. Rev. B 33 (1986) 1436.

26. J. G. Chen, J. E. Crowell and J. T. Yates Jr., J. Chem. Phys. 84 (1986) 5906.

27. J. G. Chen, J. E. Crowell and J. T. Yates Jr., Phys. Rev. B 35 (1987) 5299.

28. H. Ibach and D. L. Mills, Electron Energy Loss Spectroscopy and Surface Vibrations, First Edition (Academic Press, New York, 1982).

29. G. A. Ozin and A. V. Voet, J. Chem. Phys. 56 (1972) 4768.

30. K. Nakamoto, Infrared and Raman Spectra of Inorganic and Coordination Compounds, (John Wiley and Sons, New York, 1978).

31. P. A. Thiel and T. E. Madey, Surf. Sci. Reports 7 (1987) 211.

32. R. A. Jacobson, private communication.

33. T. J. Chuang, C. R. Brundle and K. Wandelt, Thin Solid Films 53 (1978) 19.